The Pennsylvania State University

The Graduate School

College of Engineering

AIRBORNE INSECT RADAR SCATTERING CHARACTERIZATION USING ELECTROMAGNETIC MODELING

A Dissertation in

Electrical Engineering

by

Omar Alzaabi

Submitted in Partial Fulfillment
of the Requirements
for the Degree of

Doctor of Philosophy

May 2019

The dissertation of Omar Alzaabi was reviewed and approved* by the following:

Julio V. Urbina
Associate Professor of Electrical Engineering
Dissertation Advisor
Chair of Committee

James K. Breakall
Professor of Electrical Engineering

Kenneth Jenkins
Professor of Electrical Engineering

Michael T. Lanagan
Professor of Engineering Science and Mechanics

Kultegin Aydin
Professor of Electrical Engineering
Head of the Department of Electrical Engineering

*Signatures are on file in the Graduate School

ABSTRACT

Bees are the most important pollinator; therefore, plans for their conservation require an understanding of the dynamics and the spatial scale of scavenging, to better determine their needs in terms of nesting sites and food plants. To investigate airborne insect behavior beyond the visible range, radar now plays a valuable role in entomology, particularly in enabling direct observation of insects without disturbing their natural behavior. However, target identification and classification to discriminate among species of airborne insects has always been a challenge in entomological radar applications, particularly in characterizing their scattering signatures through their Radar Cross Section (RCS). Another limitation hindering entomological radar applications generally is the distinctly differing behavior across varied wave frequencies and polarizations as well as varying viewing angles.

This thesis addresses these issues by demonstrating computational electromagnetic tools able to predict the radar scattering characteristics of aerial insects – in this case Honeybee workers (i.e. Apis Mellifera) – and to investigate RCS dependencies on multiple frequencies, polarizations and viewing angles. Knowledge of the Honeybee's dielectric properties, necessary for RCS analysis, was formed using an X-band system with a frequency range from 8.2 GHz to 12.4 GHz, at room temperature, using rectangular waveguides. By measuring both transmission and reflection parameters, dielectric properties were quantified. The dielectric constant of the Honeybee was found to average between 10.59 to 10.69 across the above frequency range, exhibiting inverse proportionality to frequency. Furthermore, the loss tangent was found to increase from 0.26 to 0.41 for the same frequency range. Based on these findings, the RCS was then simulated and predicted using commercial modeling software FEKO. To produce accurate RCS simulation, an organismal Honeybee model was developed. RCS signatures for both vertical and horizontal polarizations were

calculated at multiple frequencies and viewing angles, where the incident angle of the plane wave is $\theta = 90^{\circ}$ and $0^{\circ} \leq \varphi \leq 180^{\circ}$. The azimuth angle was incremented by 5 degrees.

To validate the calculation of backscattering RCS results of the Honeybee model obtained through the FEKO method of moments, the simulated results were compared with laboratory measurements. These measurements of backscattering cross section of Honeybee were performed in the antenna anechoic chamber at the ElectroScience Laboratory (ESL) at The Ohio State University (OSU). The backscattering RCS measurements of the Honeybee were carried out for both horizontal and vertical polarizations over a wide frequency range between 2 and 18 GHz with a frequency step of 6 MHz. These measurements were performed at the incident angle of the plane wave $\theta = 90^{\circ}$ and $0^{\circ} \leq \varphi \leq 360^{\circ}$. The azimuth angle was incremented by 5 degrees. In general, the simulated backscattering cross section of the Honeybee shows very good agreement with the obtained backscattering RCS measurements. As a result, such modeling techniques can be applied for many insect species and birds and will help to discriminate targets of different shapes and sizes, and therefore differentiate among different insect targets.

TABLE OF CONTENTS

LIST OF FIGURES

LIST OF TABLES

ACKNOWLEDGEMENTS

The studies undertaken herein appear in their current form thanks to the support, guidance, wisdom and mentorship of several people to whom I extend my deep sense of appreciation and gratitude.

To my advisor Dr. Julio Urbina, of the Electrical Engineering Department at Penn State University (PSU), I extend my deep sense of appreciation for his mentorship, guidance and patience throughout the process of selecting a research topic and at the various stages of its development. To Professor James Breakall, also of the Electrical Engineering Department at PSU, I extend my deep sense of indebtedness and appreciation for his wisdom, guidance and support throughout the process of undertaking this research and documenting its findings. To Professor Michael Lanagan and Mr. Steven Perini, of the Department of Engineering Science and Mechanics at PSU, I extend my gratitude and appreciation for making available crucial experimental apparatus used in this work and providing guidance throughout the process of the relevant empirical analysis. My appreciation for their patience and know-how cannot be overstated. I also extend thanks to Professor Kenneth Jenkins for serving on this dissertation committee and constructive feedback throughout the process of assembling this work into a finished document. To Dr. Harland Patch and Professor Christina Grozinger, both of PSU's Department of Entomology, I extend a deep sense of appreciation and gratitude for guidance, support and facilitation of materials necessary for conducting experimental studies within this scholarly work. Their personal interest in this work and constructive discussions allowed for an improved scholarly undertaking. The support, patience and wisdom of all of the above has made me a better researcher and engineer.

I also acknowledge the contributions of Dr. Reed Johnson, of The Ohio State University's (OSU) Department of Entomology, who facilitated for and provided specimens used in some of the experimental analysis undertaken at OSU. I also extend my appreciation to Dr. Chia-Hua Lin, who took the time to provide personal advice and support during experimental studies undertaken at OSU. To Mr. Kenneth Ayotte of OSU's ElectroScience Laboratory, I extend my sincere sense of indebtedness for investing significant time and effort facilitating and supporting experimental analysis undertaken at the Lab's anechoic chamber. The feedback, guidance, and personal investment of time and energy has allowed for rigorous experimental studies and subsequent analysis for which I am sincerely grateful.

My eternal indebtedness goes to my family for their unceasing support, love and encouragement. I also extend my gratitude to friends including Ibrahim Khawaji and Mohamed Alkhatib of PSU and Mohammad Al-Khaldi of OSU, to name a few, for their support throughout the grueling process of undertaking this research and assembling its findings into a finished document. Without my family and friends this work would not have been possible.

Finally, none of this work would have been possible without the opportunity and sponsorship afforded to me by the Abu-Dhabi National Oil Company (ADNOC), and Sheikh Saud bin Saqr Al-Qasimi Foundation, United Arab Emirates to which I extend my sincere gratitude and unyielding indebtedness. For the assistance they offered throughout this journey, I offer my appreciation.

Chapter 1

Introduction and Background

The Bumblebee, as well as the Honeybee (shown in Figure 1.1), is highly valued as a pollinator of flowers and important crops. The Honeybee pollinates about 70% of the hundred most common agricultural crops, which account for approximately 90% of the global food supply [1]. While the Bumblebee also significantly contributes to the pollination of crop plants, other small animal species are pests that destroy critical strands of cropped vegetation within agricultural ecosystems. In recent years, the general public has become aware that Honeybees are in serious trouble. Honeybee colonies have been mysteriously dwindling, in what has been called "Colony Collapse Disorder", and several Bumblebee species on the east and west coasts of the United States have been declining precipitously [2]. In order to develop plans and strategies to conserve the population and diversity of bees, an understanding of the spatial and temporal configuration is needed as well as their requirements in terms of nesting sites and food plants [3-6].

Figure 1.1: Honeybee [7].

1.1 Tracking Low-Flying Insects

There are traditional techniques to track low-flying insects; for example, in the mark–recapture technique, bees are marked at the nest and located while foraging to observe the distance of actual foraging trips [8, 9]. Other techniques include: genetic analysis, pollen mapping, nest–forager association, nest–plant association, and nest site addition [8]. Most of the data that has been found using these techniques was not obtained with equal sample effort per unit area, which makes it impossible to determine maximum foraging distance. This is because, as the search area expands as the square of the distance from the nest, so the number of marked bees in the landscape is quickly diluted.

Collecting ecologically-relevant movement information from flying insects is a challenge in the case of insects beyond visual range. Therefore, remote sensing is used to provide a solution for this problem. The term "remote sensing" was coined by Evelyn Pruitt, at the office of Naval Research in 1960's, as "[a] technique to record electromagnetic radiation beyond human vision" [10]. It is also defined as "[a] multi-disciplinary technique of electronic and analog image acquisition and exploitation" [10]. A complete definition, however, comes from [11] as "[t]he measurement or acquisition of information about some property of an object or phenomenon by a recording device which is not in physical or intimate contact with the object or phenomenon under study".

During the mid-20th century, remote sensing was used for entomological applications [12]. Photography, videography, thermal and spectral imaging are all techniques that are non-invasive – but proved unable to identify insects. These techniques rely generally on detection of plant stress or damage which can suggest insect activity, but which is mostly not the case [13]. Moreover, they are not suitable for real-time monitoring and surveying of large or inaccessible insect-affected areas [14].

Nowadays, radar (Radio Detection And Ranging) plays an important role in the tracking of moving entities beyond the visible range. It uses electromagnetic signals to sense and observe motion. In this case, insects' motion can be detected and studied without disturbing their natural behavior. The electromagnetic energy is radiated to and reflected (echoed) back from the intercepting target, which provides an accurate measurement for locating the target [15]. However, there has not been much effort put into RCS detection of bees.

One of the most widely used techniques today for tracking small low-flying insects is harmonic tracking, using low-cost harmonic transponders with their associated harmonic radar [16]. The harmonic transponder is simply a frequency doubler connected to an antenna. The frequency doubler is a nonlinear element, usually a passive Schottky diode, which has a small built-in potential (a few hundreds of mV) such that the low-power received by the transponder is enough to drive the diode into operation. The nonlinear component efficiently converts the power f_0 from the transponder to the $2f_0$ frequency, while the harmonic radar and the transponder communicate using an antenna. The efficiency of the harmonic transponder depends directly on the selected combination of antenna and frequency doubler. This technique, however, is limited as follows: the aerial insect needs to be aligned either horizontally [17] or vertically [18], with a harmonic radar polarization which results in aerodynamic drag that affects the flight behavior of the bees [19, 20]. This can result in overloading [21] or entangling [22] of the bee. For instance, vertical transponders for monitoring bees are too tall to allow the insects to move around within their nests or hives, so this could affect their flight behavior [16]. As an additional problem, these transponders have introduced some challenges for monitoring, as they are fitted when bees leave, and removed on their return. Electromagnetic field distortion introduced by the body of the insect causes a loss of efficiency by the transponders [16]. This problem is tackled to a certain degree by using a glass tube and discs to attach the transponder onto the insect's body, as illustrated in Figure 1.2. However,

such a feature increases the transponder's length and weight, which causes a disturbance to the insect's behavior.

Figure 1.2: A Honeybee wearing a vertical wire transponder placed inside a detachable glass tube [23].

The main idea behind detecting insects on radar is the reflection of radio waves back towards a transmitter. Each insect has different effectiveness with regards to how well it reflects the radio waves. Therefore, the first technical task in radar entomology is to measure this property (the radar back scattering cross-section, or RCS) for insect species of interest, and to determine how it varies with the aspect they present to the radar [24, 25].

In this thesis, a different approach is explored by using backscattering RCS. In this way, we can overcome limitations of previous methods, and it can also pave the way for radar entomology to follow in a similar path, where three-dimensional models of aerial insects are made on commercial software such as FEKO, simulating real-life situations.

1.2 Radar Cross Section

1.2.1 RCS Definition

Radar Cross Section (RCS) is the amount of scattered power that a target reflects back at the radar. According to the IEEE Standard Dictionary of Electrical and Electronics Terms, RCS is "a measure of the reflective strength of a radar target defined as 4π times the ratio of the power per unit solid angle scattered in a specified direction to the power per unit area in a plane wave incident on the scatterer from a specified direction" [26]. A more explicit definition is that the RCS is the ratio of the incident power density to the power density scattered by an object. The formal mathematical definition of radar cross section is [15]:

$$\sigma = \lim_{R \to \infty} 4\pi R^2 \frac{|E_s|^2}{|E_0|^2} \tag{1.1}$$

where σ is the RCS of the target, R the range between radar and target, E_0 the electric-field strength of the incident wave impinging on the target, and E_s the electric-field strength of the scattered wave at the radar. The RCS defined by equation (1.1) is often referred to as either monostatic or backscattered RCS.

More simply, a target's RCS (σ) is visualized as the product of three factors, as determined by equation (1.2):

$$\sigma = (\text{Projected Cross Section}) \times (\text{Reflectivity}) \times (\text{Directivity}) \tag{1.2}$$

where the reflectivity is the percent of the intercepted power radiated by the target, and the directivity is the ratio of the power reflected in the radar's receiver direction to the power that would have been reflected to the receiver if the scattering had been uniform in all directions [27].

The unit of RCS is usually given in square meters. Due to large variations in the RCS pattern from one aspect angle to another, it is convenient to display the RCS in logarithmic form. The unit commonly used is decibel over square meter or dBsm [28].

$$\text{RCS (dBsm)} = 10 \log_{10} \sigma \tag{1.3}$$

The RCS value depends basically on several parameters, including: target shape, target material composition (electric and/or magnetic properties), and size of target; wavelength of the illuminating radar; incident and reflected angle of the radar beam; and the polarization of the transmitted radiation with respect to the orientation of the target.

1.2.2 Scattering Regions

The manner in which an impinging electromagnetic wave is scattered by a target depends on the target size relative to the wavelength of the incident wave. The dependence of the RCS on the characteristic target size, L, is sorted into three different regions [29-31]:

- The Rayleigh region (low-frequency region), where target dimensions (L) are much less than the probing wavelength ($L \ll \lambda$). In this region, the RCS is approximately

proportional to the fourth power of the frequency ($\sigma \propto f^4$) and to the square of the volume of the target ($\sigma \propto (\text{target volume})^2$).

- The Mie region (Resonant region), where target dimensions are comparable to the probing wavelength ($L \approx \lambda$), the RCS oscillates in a complex way due to interference between signals reflected from different parts of the target.

- The Optical region (high-frequency region), where target dimensions are very large compared to the probing wavelength ($L \gg \lambda$), the RCS behaves more simply and is approximately proportional to the geometric cross section, but is also strongly dependent on target geometry.

To illustrate these regions, it is useful to study the RCS of a Perfectly Electric Conductive (PEC) sphere as a function of the electrical size of the radius (ratio of radius to wavelength), since its RCS is independent of aspect angle. Figure 1.3 shows the change in RCS value of a sphere as its radius increases with respect to wavelength. From this graph we see that the RCS for a PEC sphere is constant in the optical region. For this reason, radar designers typically use spheres of known cross sections to calibrate radar systems experimentally.

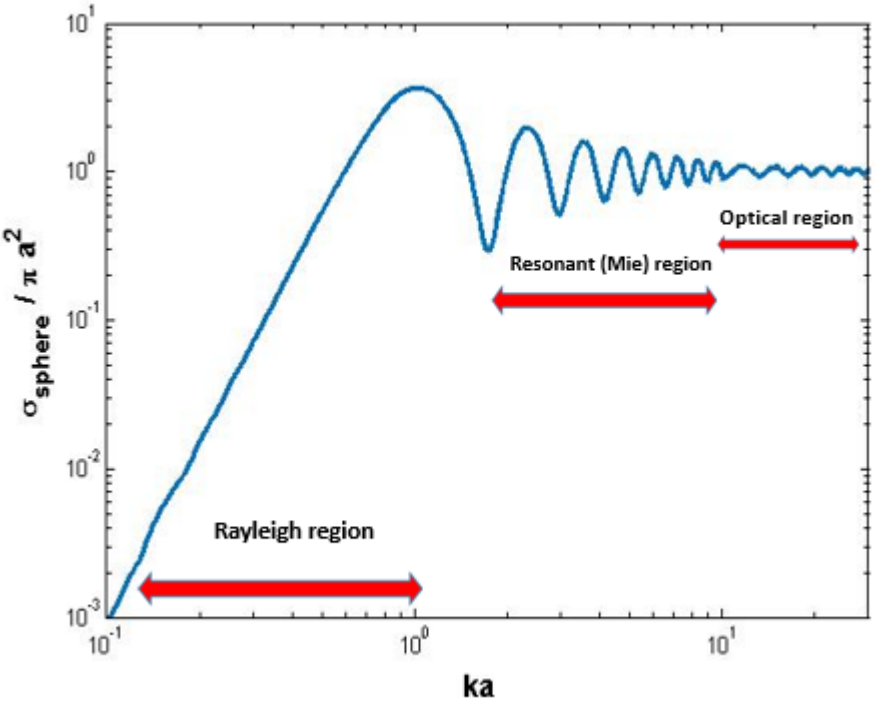

Figure 1.3: Radar cross section of a perfectly conducting sphere, created using electromagnetic software FEKO, where a is the radius of the sphere. The parameter $ka = {}^{2\pi a}/_{\lambda}$ is the circumference of the sphere expressed in wavelengths.

1.2.3 RCS Measurements

The scattering of an electromagnetic wave by a target can be measured and separated into three different categories: backscattering, bistatic scattering, and forward scattering. Backscattering is when the signal reflection is directed back to the source antenna. In contrast, bistatic scattering is when the signal is scattered in all directions other than the direction of the incident wave. A

forward scattered wave is when the scattering is in the direction of the incident wave. Since most radar systems have a transmitter and receiver in one physical position (monostatic), backscattered signals are most useful. However, if the transmitter and receiver are not in the same position, bistatic and forward scattered signals are used to detect the target.

The RCS of an object can be related to the other system parameters via the radar range equation, given by equation (1.4) [30]:

$$P_r = P_t \frac{G_t G_r \lambda^2 \sigma}{(4\pi)^3 R_t^2 R_r^2} \tag{1.4}$$

where P_r is the power received at the receiving antenna, P_t is the power transmitted from the source antenna, G_t is the gain of the source antenna, G_r is the gain of the receiving antenna, σ is the RCS, R_t is the distance from the source antenna to the target, and R_r is the distance from the receiving antenna to the target. For monostatic RCS systems, $R_t = R_r$.

The most important requirement for RCS measurement is to operate the measurement in the far-field. In this region, the incident field can most accessibly be defined by a plane wave with components that are purely real, with a radial decay dependency of 1/r, where r is the radial distance from the source. For the illuminated target to be in the far-field, it must lie at a minimal distance, R_{min}, away from the source and/or reciever. The conditions outlined in (1.5.1 – 1.5.3) ensure that sufficient radial separation is met between transmitter, target and receiver for far-field conditions to be met.

$$R_{min} > {}^{2D^2}/_{\lambda} \tag{1.5.1}$$

$$R_{min} > 5D \tag{1.5.2}$$

$$R_{min} > 1.6\lambda \tag{1.5.3}$$

where D is the largest dimension of the transmitting antenna and λ represents electromagnetic wavelength; in turn this will ensure acceptable phase and amplitude with sufficient uniformity when the target is illuminated by a radar wave [32].

Depending on the size of the test target, the frequencies to be used, and other test requirements, measurements may be made in indoor test facilities or on outdoor ranges. In general, outdoor facilities are required when test targets are too large to be measured indoors. A disadvantage of such facilities is that they are easily influenced by weather and wind conditions, and consequently it is difficult to get high resolution and accurate results. In contrast, indoor facilities such as anechoic chambers, whose interior walls are covered with high-quality radar-absorbing material, offer the attractive advantage of being independent of weather conditions, and therefore provide more productive testing [33].

1.3 The RSC Characteristics of Insects

Several researchers have used RCS measurements to study electromagnetic wave interactions with airborne insects. Hajovsky et al. has measured the backscattering cross sections for different species of insects, to determine their general magnitude, and the polarization dependence that their cross sections exhibit [34]. The measurements were performed at 9.41 GHz and made on the roof of the laboratory. The insects were alive but drugged to immobilize them for the measurements. It was found that larger cross sections are generally associated with larger insects. Additionally, the results indicated that the polarization of the incident wave had an effect in the magnitude of the backscattering cross section of an insect. Larger differences in cross sections were experienced when insect body lengths are much greater than their body diameters, as in the case of the Alfalfa Caterpillar butterfly. The backscattering cross section measured varied by about 15 dB between horizontal and vertical polarizations.

To continue investigating the RCS of insects, Riley published polar diagram plots of the RCS against aspects of three types of insect pests, namely the desert locust (Schistocerca gregaria), the African migratory locust (Locusta migratoria migratorioides), and the armyworm moth (Spodoptera littoralis) [24]. The radar wavelength used was 3.18 cm (9.41 GHz). The measurements were carried out with anaesthetized insects viewed horizontally and using horizontal polarization. Generally, the largest cross section was found when the insect was viewed from the side, but it was found to be slightly larger from head-on for some insects. The RCS varied significantly, with deep nulls when viewed from some angles.

A few years later, Riley also performed X-band measurements of RCS as a function of the angle between insect body axis and the orientation of the polarization plane for different species and sizes of insects [34]. Small insects had a maximum at parallel polarization and a minimum at perpendicular polarization. However, larger insects had a maximum occurring at perpendicular polarization and a minimum at parallel polarization.

Due to the complexity of insect shape for RCS prediction, Riley also showed the relationship between the RCS of spherical water droplets and the mass of an insect [35]. The insects were killed and dried out to estimate their free water content. After that, the RCS of a spherical water drop of mass equal to the free water content of each insect was calculated. It is shown in [15] for various insects at a wavelength of 3.18 cm (9.41 GHz) overlaid on the classical scattering from water droplets of equivalent mass. It would appear that the RCSs of large insects (such as locusts) are at the lower end of the interference region, and those of the smaller insects (such as aphids) are at the higher end of the Rayleigh region. The RCS of a water sphere gives a remarkably good estimate of the mean RCS of an insect of equivalent mass. However, it gives no hint of the variation in aspect and plane of polarization, since the RCS of a sphere is independent of these parameters.

1.4 Thesis Goals

Target identification is a challenging topic within entomological radar studies. So far, there's been too little knowledge of insect RCS to establish a radar scheme for them. Until now, only a few types of insects of certain species have been measured in the laboratory; therefore, a valid comparison between species cannot be established. Even though these measurements have provided a plethora of RCS information, they still don't give information at multiple frequencies or polarizations and observing angles. Also, existing measurements are reported through a limited set of azimuth or elevation angles, which limits their generality in entomological radar applications.

Further experimental measurements of insect RCSs are needed to gain additional understanding of insect RCSs and a more reliable index. Although RCS measurements are always possible, it is impractical to conduct measurements on extremely large objects, such as aircrafts or motor vehicles, or tiny objects, such as airborne insects. For airborne insects, these issues arise due to the delicacy and fragility of the body (e.g., a Honeybee). Electromagnetic modeling can provide a substitute solution to performing this analysis, however, its limits are not boundless. By accounting for the limitations of electromagnetic modeling, sacrifices are bound to happen in accuracy, convenience and practicality, when selecting the most appropriate RCS method of analysis to use. Furthermore, in order to produce realistic scattered fields from biological scatterers such as insects, prior knowledge of their dielectric properties are vital.

This thesis demonstrates computational electromagnetic tools which can predict radar scattering characteristics of aerial insects – specifically Honeybee workers (i.e. Apis Mellifera) – and investigates their dependence on the RCS at multiple frequencies or polarizations and observable angles.

1.5 Contributions to Knowledge

The contributions of this work can be summarized by numerical investigations into the means by which Honeybee radar cross section can be modelled across a wide range of frequency, view angle and polarization under varying dry/wet conditions. This is coupled with extensive complementary experimental investigation aimed at validating and extending conclusions from this knowledge. This work furthers insect tracking ability, which in turn improves our understanding of the entomological and ecological implications. This work has resulted thus far in two scholarly contributions at the National Radio Science Meeting.

In this work the following lines of analysis are carried out:

1. Characterizing and experimentally quantifying Honeybee dielectric properties across a wide range of frequencies.
2. Correlating dielectric properties of Honeybees with other organic tissue.
3. Extending biological insect models with the computational electromagnetic tool, FEKO, typically used for antenna and component level studies.
4. Subsequently analyzing available numerical solvers and establishing relations between ideal solver and object of simulation.
5. Characterizing Honeybee RCS across a wide range of frequencies and view angles through simulation.
6. Establishing experimental set up for measurements of Honeybee RCS across a wide range of frequencies and view angles.
7. Empirically analyzing how Honeybee frequency response under various dry/wet conditions affects dielectric properties of test subjects.
8. Correlating and validating results from numerical (simulation) analysis and subsequent empirical investigation.

9. Illustrating dependencies of Honeybee RCS on incidence wave polarization.
10. Illustrating dependencies of Honeybee RCS on frequency and resonance.

1.6 Thesis Organization

The thesis is presented in five Chapters and two Appendices. Chapter 2 presents the experimental technique that measures dielectric properties of the Honeybee worker (i.e. Apis Mellifera) at a frequency range from 8.2 GHz to 12.4 GHz (X-band) at room temperature. To validate the results obtained on dielectric properties of Honeybee tissue, they are compared with previous studies on dielectric properties of different types of human tissues. Chapter 3 introduces the computational electromagnetic method (CEM) techniques used in numerical evaluations of RCS of complex objects. It demonstrates the capability of the numerical electromagnetic model, such as the method of moments (MoM) implemented in the FEKO software package, in producing realistic scattered electric fields of an organismal model, in this case a Honeybee worker (i.e. Apis Mellifera). Chapter 4 assesses the validity of the backscattering cross section results of the Honeybee model obtained through the FEKO method of moments. A laboratory measurement of the backscattering cross section of the Honeybee is performed and compared with the numerical electromagnetic model results. Chapter 5 summarizes the thesis and discusses future work that could benefit the field of radar entomology for tracking low altitude flying insects. For each of the aforementioned Chapters, a bibliography is attached in which the relevant scholarly work is identified, acknowledged and incorporated as part of the discussion material.

1.7 References

[1] PAN. 2012. Pesticides and Honeybees: State of the Science. Pesticide Action Network North America. Retrieved from https://www.panna.org/sites/default/files Bees&Pesticides_SOS_FINAL_May2012.pdf

[2] Moissett, Beatriz, and Steve Buchanan. *Bee basics: an introduction to our native bees*. USDA, Forest Service, 2010.

[3] Osborne, J. L., et al. "A landscape-scale study of Bumblebee foraging range and constancy, using harmonic radar." *Journal of Applied Ecology* 36.4 (1999): 519-533.

[4] Fussell, M., and Sarah A. Corbet. "Forage for Bumblebees and Honeybees in farmland: a case study." *Journal of apicultural Research* 30.2 (1991): 87-97.

[5] Fussell, M., and Sarah A. Corbet. "Flower usage by bumble-bees: a basis for forage plant management." *Journal of Applied Ecology* (1992): 451-465.

[6] Fussell, M., and Sarah A. Corbet. "The nesting places of some British Bumblebees." *Journal of Apicultural Research* 31.1 (1992): 32-41.

[7] Sass, Jennifer. "Why We need bees: Nature's tiny workers put food on our tables." *Natural Resources Defense Council March* (2011).

[8] Greenleaf, Sarah S., et al. "Bee foraging ranges and their relationship to body size." *Oecologia* 153.3 (2007): 589-596.

[9] Kapyla, Markku. "Foraging distance of a small solitary bee, Chelostoma maxillosum (Hymenoptera, Megachilidae)." *Annales Entomologici Fennici*. 1978.

[10] Lusch, D. P., ed. *Introduction to environmental remote sensing*. 1999, Centre for remote sensing and GIS, Michigan State University.

[11] Colwell, R. N., ed. *Manual of remote sensing*. ed. R. N. Colwell and A.S.o. Photogrammetry. 1983, American Society of Photogrammetry.

[12] Riley, J., *Remote sensing in entomology.* Ann. Rev. Entomol., 1989. 34: p. 247-271.

[13] Murtha, P. A., *Detection and analysis of vegetation stress*, in *In remote sensing for resource management*. 1982: Ankeny, Iowa. p. 141- 57.

[14] Tahir, N. and G. Brooker. *Recent developments and recommendations for improving harmonic radar tracking systems*, in *5th European Conference on Antennas and Propagation, EuCap 2011*. 2011: Rome, Italy. p. 1531 - 1535.

[15] Skolnik, M. I. "Radar Handbook, Vol. 1, 8." (2008).

[16] Riley, J. R., and A. D. Smith. "Design considerations for an harmonic radar to investigate the flight of insects at low altitude." *Computers and Electronics in Agriculture* 35.2 (2002): 151-169.

[17] Mascanzoni, Daniel, and Henrik Wallin. "The harmonic radar: a new method of tracing insects in the field." *Ecological entomology* 11.4 (1986): 387-390.

[18] Riley, J. R., et al. "Recent applications of radar to entomology." *Outlooks on pest management* 18.2 (2007): 62-68.

[19] Riley, J. R., et al. "Tracking bees with harmonic radar." *Nature* 379.6560 (1996):

[20] Colpitts, Bruce G., and Gilles Boiteau. "Harmonic radar transceiver design: Miniature tags for insect tracking." *IEEE Transactions on Antennas and Propagation* 52.11 (2004): 2825-2832.

[21] Boiteau, Gilles, and Bruce Colpitts. "Electronic tags for the tracking of insects in flight: effect of weight on flight performance of adult Colorado potato beetles." *Entomologia experimentalis et applicata* 100.2 (2001): 187-193.

[22] Roland, Jens, et al. "Even smaller radar tags on insects." *Nature* 381.6578 (1996): 120-120.

[23] Chapman, Jason W., V. Alistair Drake, and Don R. Reynolds. "Recent insights from radar studies of insect flight." *Annual review of entomology* 56 (2011): 337-356.

[24] Riley, J. R. "Angular and temporal variations in the radar cross-sections of insects." *Proceedings of the Institution of Electrical Engineers*. Vol. 120. No. 10. IET, 1973.

[25] Schaefer, G. W. "Radar observations of insect flight." *Symposia of the Royal entomological Society of London*. 1976.

[26] IEEE Standard Dictionary of Electrical and Electronics Terms. New York: Institute of Electrical and Electronics Engineers, Inc., 1988.

[27] Constantine, A. Balanis. "Antenna theory: analysis and design." *third edition, John Wiley & sons* (2005).

[28] Chibuisi, Iroegbu. "Simulation of Radar Cross Section (RCS) of Spherical Objects."

[29] Uluisik, Cagatay, et al. "Radar cross section (RCS) modeling and simulation, part 1: a tutorial review of definitions, strategies, and canonical examples." *IEEE Antennas and Propagation Magazine* 50.1 (2008).

[30] Knott, Eugene F. *Radar cross section measurements*. Springer Science & Business Media, 2012.

[31] Jenn, David C. "Radar and Laser Cross Section Engineering AIAA Education Series." *Washington, DC 1995* (1995).

[32] Stutzman, Warren L., and Gary A. Thiele. *Antenna theory and design*. John Wiley & Sons, 2013.

[33] Dybdal, Robert B. *Radar cross section measurements*. No. TR-0086 (6925-05)-5. AEROSPACE CORP EL SEGUNDO CA ELECTRONICS RESEARCH LAB, 1986.

[34] Hajovsky, R., A. Deam, and A. LaGrone. "Radar reflections from insects in the lower atmosphere." *IEEE Transactions on Antennas and Propagation* 14.2 (1966): 224-227.

[35] Riley, Joseph R. "Radar cross section of insects." *Proceedings of the IEEE* 73.2 (1985): 228-232.

Chapter 2

Dielectric Properties of Honeybee Body Tissue for Insect Tracking Applications

2.1 Introduction

Developing a classification system to discriminate among species of aerial objects has always been a challenge in entomological radar applications. In these applications, the interaction of radio waves with these objects introduces radar scatterings, characterized by their radar cross section (RCS). RCS is defined as: "[a] quantitative measure of the ratio of power density in the vector signal scattered in the direction of the receiver to the power density of the radar wave incident upon the target" [1]. RCS values are dependent on a number of characteristics: size, shape, material, and aspect of the target, as well as the wavelength and polarization of transmitted radiation with respect to the orientation of the target. What's more, the RCS of objects such as insects can be much more complex to predict because of the complexity of their surface profiles and dielectric constants.

Dielectric properties of biological tissues have been of interest for many years, however, available dielectric properties of insects are limited, as discussed in several studies [2-16]. In these studies, the main goal was to study the dielectric properties of insects for treating infested products, for control purposes, using radio-frequency and microwave heating.

With the need to develop insect tracking systems comes a need to develop standardized techniques for quantifying radio wave scattering at different radar wavelengths and polarizations. In order to obtain an accurate prediction of the RCS of Honeybee body tissue, measuring its dielectric properties is vital. Therefore, in this chapter, we investigate the dielectric properties of Honeybee tissue, to study its interaction with electromagnetic fields.

2.2 Samples collection procedure

In early summer of the 2017 season, Honeybee workers (i.e., Apis Mellifera) were carefully collected. The typical generation age of Honeybees in summer is 10 to 30 days. The Honeybees were collected in accordance with relevant guidelines of the Penn State College of Agricultural sciences. Protective gear such as veil, gloves and smoker were used and made the collection of Honeybees safer and easier. A smoker is quite an essential component, as it makes aggressive bees more docile and minimizes defensive reactions during the collection process. The Honeybees lived in standard bee hives and were collected in jars. All Honeybee samples were collected to obtain the dielectric properties of these bees using the waveguide technique. Care was taken to eliminate any suspicious effect on the measurement of Honeybee dielectric properties. For instance, collected Honeybee samples could contain no loose debris or beeswax on their body structures. In addition, the dielectric properties of all collected samples were measured mostly within two hours of collection, to insure perfect wettability conditions of each collected Honeybee body tissue.

2.3 Honeybee dielectric properties measurements

Measurement of dielectric properties were made to determine the complex relative permittivity of the collected Honeybees,

$$\varepsilon = \varepsilon' - j\varepsilon'' \tag{2.1}$$

where ε' is the dielectric constant and ε'' is the dielectric loss factor. Permittivity measurements were made using an Anritsu 37369D vector network analyzer (VNA). This 40 MHz to 40 GHz analyzer is a single-instrument system that contains a built-in signal source, a test set, and an analyzer subsystem. The measurement set up is shown in Figure 2.1. Each sample was packed into

a rectangular waveguide as shown in Figure 2.2. The waveguide was fabricated by machining waveguide flange stock (Micro-Coax Inc., Collegeville PA) to a thickness of 3 mm. The frequency range of interest is dependent upon the waveguide geometry. The band used for the dielectric constant and loss measurements was the X-band rectangular waveguide (h = 1.27 cm, w = 2.29 cm) with a frequency range from 8.2 to 12.4 GHz. The waveguide was attached to the VNA ports by flange adapters using 3.5mm coaxial cables (GORE® VNA Microwave/RF Test Assemblies). This VNA is interfaced with a computer running LabVIEW software for data computation and acquisition. The software program is designed to acquire the S-parameter data from the VNA, and then precisely calculate the dielectric properties.

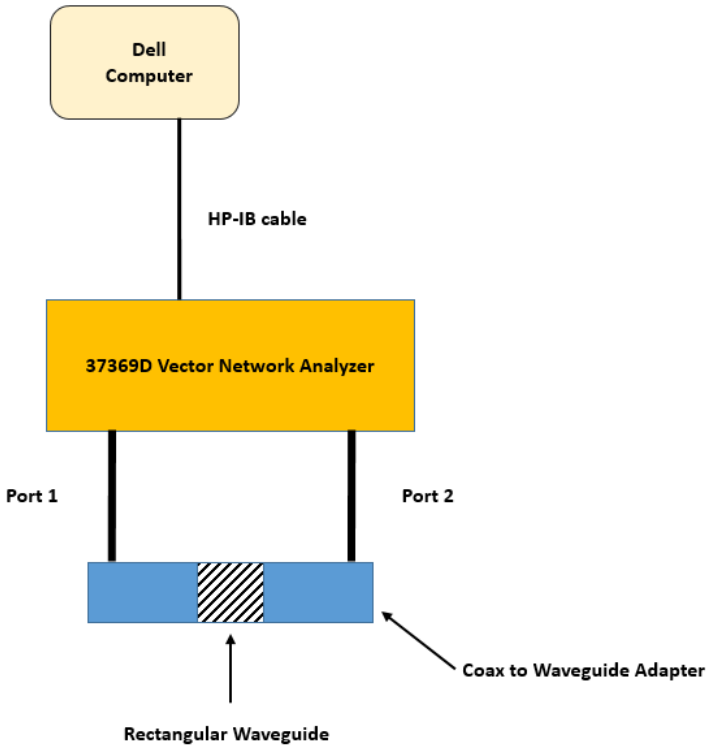

Figure 2.1: Schematic of the Anritsu 37369D network analyzer system with rectangular waveguide.

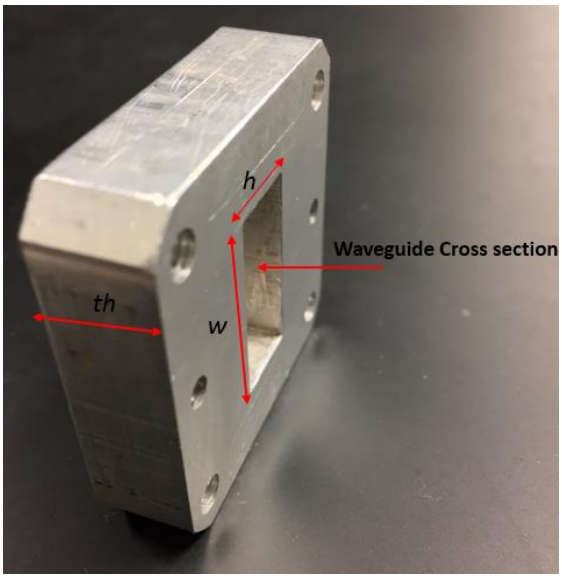

Figure 2.2: Rectangular Waveguide Used in the Experiment.

Prior to any measurement, the Anritsu 37369D system had to be calibrated. To calculate dielectric properties accurately, a Maury Microwave X7005E calibration kit was used to obtain accurate measurements of the complex reflection and transmission coefficients (S_{11} and S_{21}). The calibration process generates reference planes of known impedance, from which the real and imaginary parts of both S-parameters were determined. The reference planes' placement is shown in Figure 2.3. Full two-port calibration standards (Maury Microwave, Cucamonga CA) for the full two-port waveguide calibration consisted of shorts, a matched load, a sliding load and a through connection.

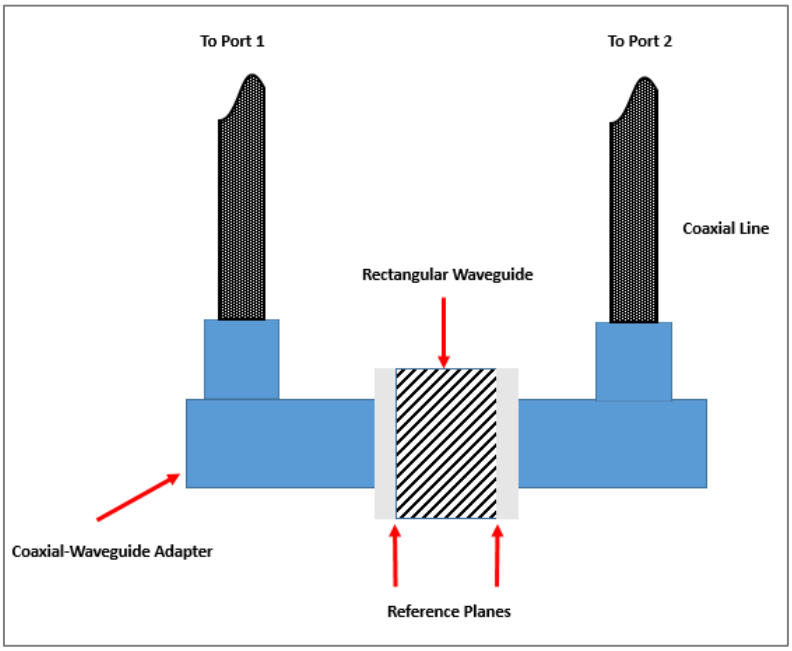

Figure 2.3: Schematic of rectangular waveguide, flange adapter, and reference plane position.

The transmission and reflection parameters were measured for a rectangular waveguide packed with Honeybee samples. A relationship is derived between the complex scattering parameters S_{11} and S_{21}, and the dielectric properties of a material [17],

$$S_{11} = \rho \frac{1 - e^{-2\gamma l}}{1 - \rho^2 e^{-2\gamma l}} \tag{2.2}$$

$$S_{21} = \rho \frac{(1 - \rho^2) e^{-\gamma l}}{1 - \rho^2 e^{-2\gamma l}} \tag{2.3}$$

where ρ is the complex reflection coefficient, and γ is the propagation coefficient. Dielectric property information is contained in the ρ and γ coefficients as shown in equations (2.2) and (2.3). The thickness of the dielectric slab is l.

$$\rho = \frac{1 - (\varepsilon^*)^{1/2}}{1 + (\varepsilon^*)^{1/2}} \tag{2.4}$$

Here ε^* is the relative complex permittivity. The propagation coefficient, γ, can be expressed in terms of the real and imaginary parts of the permittivity [18]:

$$\gamma = \alpha + j\beta = j\omega(\mu^*\varepsilon^*)^{1/2} \tag{2.5}$$

where

$$\alpha = \left[\pi(\varepsilon')^{\frac{1}{2}} \tan\delta\right]/\lambda_o \tag{2.6}$$

$$\beta = \left[2\pi(\varepsilon')^{\frac{1}{2}}\right]/\lambda_o \tag{2.7}$$

In equations (2.5) to (2.7), ε' is the real part of the permittivity, λ_o is the free-space wavelength, and μ^* is the complex permeability. The complex permittivity was solved in terms of the scattering parameters S_{11} and S_{21} by combining equations (2.2) and (2.3) [19].

$$\varepsilon_r = \frac{(1 - S_{11})^2 - {S_{21}}^2}{(1 + S_{11})^2 - {S_{21}}^2} \tag{2.8}$$

Equations (2.2), (2.3) and (2.8) were derived for free space conditions and need to be modified to account for the dispersive nature of the waveguide. The extension of equation (2.8) for waveguide configuration can be expressed as follows [20]:

$$\left(\frac{\gamma}{\gamma_o}\right) = \frac{(1 - S_{11})^2 - {S_{21}}^2}{(1 + S_{11})^2 - {S_{21}}^2} \tag{2.9}$$

where $\gamma_o = (k_c^2 - k_O^2)^{1/2}$ and $\gamma = (k_c^2 - \varepsilon(k_o)^2)^{1/2}$.

In equation (2.9), γ_o and γ are the propagation constants of an air-filled and dielectric-filled waveguide respectively, k_c is the cutoff wavenumber, and k_o is the free space wavenumber.

2.4 Measurements Procedure

To accurately measure scattering parameters, the Honeybee samples completely filled the waveguide cross section, as shown in Figure 2.4 (a). Since electromagnetic energy radiated through the air gap causes an error in S-parameter measurements, air gaps between the Honeybees and waveguide cross section will have a great influence on measured dielectric properties. To eliminate this effect on dielectric measurements, a dielectric mixture equation can be used to provide effective complex relative permittivity of the solid Honeybee tissue.

Various dielectric mixture equations have been proposed to represent the effective permittivity of mixtures of dielectric materials. These equations have unique performance and characteristics in various applications and are discussed in the literature [20-26]. For a two-component mixture, such as insects and air, the Landau & Lifshitz and Looyenga dielectric mixture equation is used to convert the measurement data on bulk samples of Honeybee (Honeybee-air

mixtures), to calculate the complex relative permittivity of the solid Honeybee body tissue from the complex relative permittivity of an air-Honeybees mixture. The Landau & Lifshitz and Looyenga dielectric mixture equation can be expressed as follows [27, 28]:

$$(\varepsilon)^{1/3} = v_1(\varepsilon_1)^{1/3} + v_2(\varepsilon_2)^{1/3} \tag{2.10}$$

where $\varepsilon = \varepsilon' - j\varepsilon''$ represents the complex relative permittivity of the mixture, ε' is the dielectric constant, ε'' is the dielectric loss factor, subscripts 1 and 2 refer to the air and samples of Honeybee, respectively, and v_1, and v_2 are the volume fractions of the respective components, where $v_1 + v_2 = 1$. Thus, the complex relative permittivity of Honeybee tissue can be determined by substituting $1 - j(0)$ for ε_1, the complex relative permittivity of air, and solving for ε_2. The corresponding equation is:

$$\varepsilon_2 = \left(\frac{\varepsilon^{1/3} + v_2 - 1}{v_2} \right)^3 \tag{2.11}$$

To use the mixture equation, one needs to know the complex relative permittivity of the mixture, ε, and the fractional part of the total volume of the mixture occupied by the Honeybee samples in waveguide cross section.

Generally, insects require a more sophisticated technique to measure their volume. Luckily, there is a straightforward way to measure the volume of an irregularly-shaped object using the liquid displacement method in a graduated cylinder. The objects need to have higher density than that of the liquid to estimate the volume correctly. Since the density of a Honeybee ranges from 0.8 g/cm^3 to 0.9 g/cm^3, acetone, which has a density of 0.78 g/cm^3 is used as a liquid to perform the displacement method. A 25 ml graduated cylinder, with each division at 0.1 ml, filled with acetone

solvent, is used to calculate the volume of the Honeybee samples. The acetone solvent is added to a graduated cylinder until it reaches a certain height level sufficient to submerge the Honeybee samples. Later, as shown in Figure 2.4 (b), the Honeybee samples are submerged in the graduated cylinder, until the acetone solvent reaches the final height level. The difference between the initial and final acetone height levels is the volume of the Honeybee samples. The estimated measured volume of the Honeybee was found to be in the range of $100 - 150\ mm^3$.

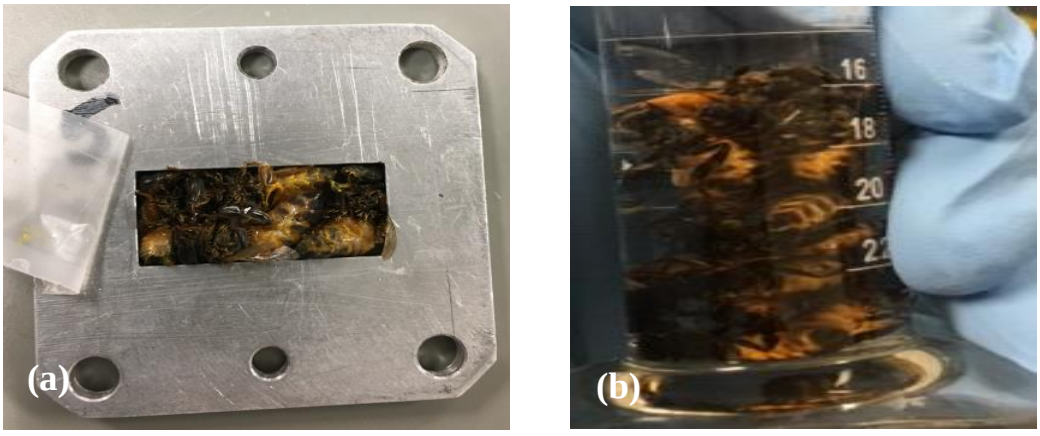

Figure 2.4: (a) Honeybee samples fill the waveguide cross section. (b) Honeybee samples submerged in the graduated cylinder.

Three sets of Honeybee samples were prepared to determine complex relative permittivity of the Honeybee body tissue at a frequency range from 8.2 GHz to 12.4 GHz at room temperature, using a rectangular waveguide packed with Honeybee samples. Then, both transmission and reflection parameters were measured by VNA to determine the dielectric properties using LabVIEW software.

2.5 Results and Discussion

The dielectric properties measurements were performed using an X-band system, to determine complex relative permittivity of the Honeybee body tissue at a frequency range from 8.2 GHz to 12.4 GHz at room temperature, for a rectangular waveguide packed with bulk samples of Honeybees. The measurements were performed on three different sets of Honeybee workers. Results of the complex relative permittivity measurements are summarized graphically in Figures 2.5-2.8. As frequency increases from 8.2 to 12.4 GHz, Figure 2.5 and Figure 2.6 show the calculated dielectric constant and calculated dielectric loss factor obtained from equation (2.11) of the Honeybee body tissue, respectively. In Figure 2.5, the dielectric constant decreases as the frequency increases. Meanwhile, the dielectric loss factor increases as the frequency increases, as shown in Figure 2.6. Figure 2.7 shows that the average dielectric constant of the three sets of Honeybee samples increases as frequency increases from 8.2 to 10 GHz, reaches a maximum at 10 GHz, and then starts to decrease, as frequency continues increasing from the 10 to 12.4 GHz range. On the other hand, Figure 2.8 illustrates that the average dielectric loss factor of the three set samples decreases slowly between 8.2 and 9 GHz and increases gradually as frequency increases from 9 to 12.4 GHz. The loss tangent which is related to energy loss is described as the ratio of the dielectric loss factor divided by the dielectric constant. The average loss tangent is found to increase from 0.25 to 0.4 as the frequency increases from 8.2 to 12.4 GHz, respectively.

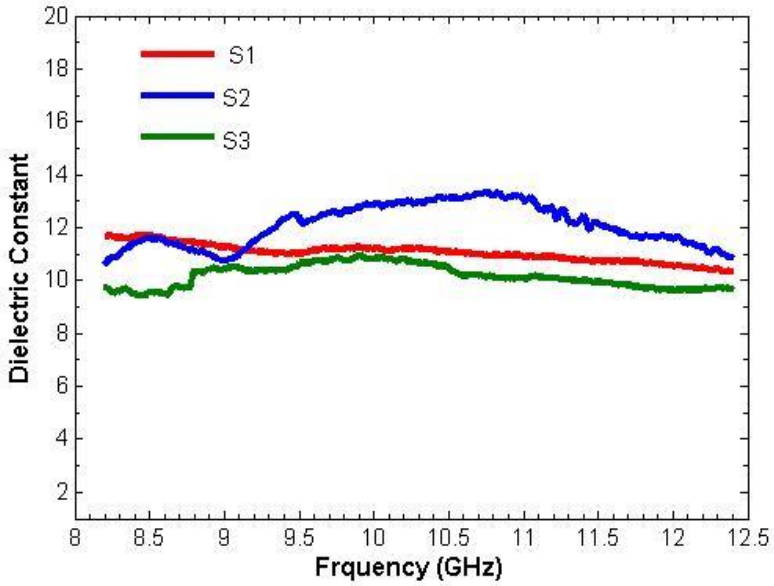

Figure 2.5: Dielectric constant of three different sets of Honeybee samples calculated by equation (2.11) from measured dielectric properties of bulk samples of Honeybees.

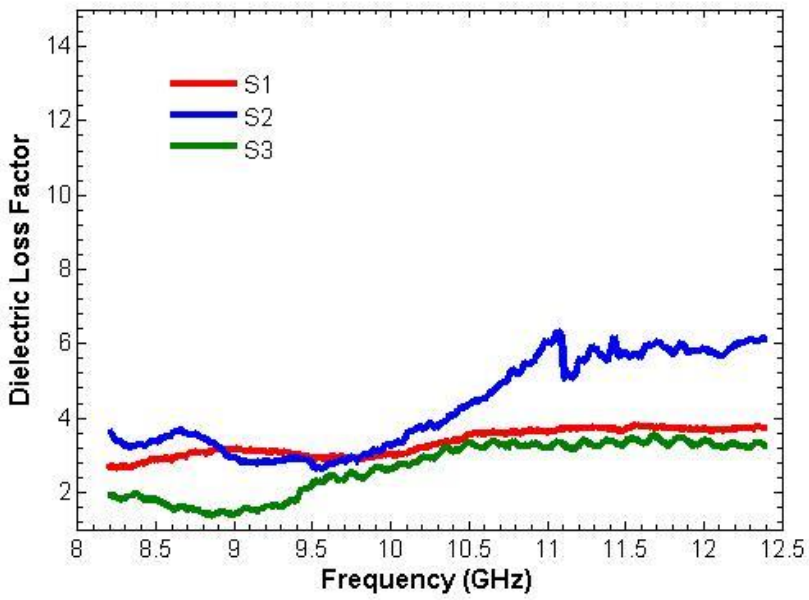

Figure 2.6: Dielectric loss factor of three different sets of Honeybee samples calculated by equation (2.11) from measured dielectric properties of bulk samples of Honeybees.

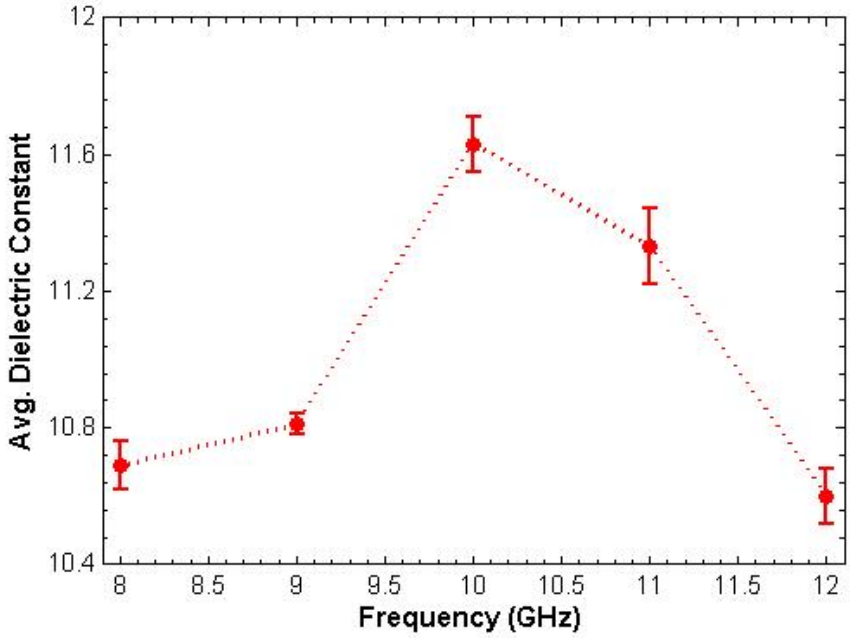

Figure 2.7: Average dielectric constant of three different sets of Honeybee samples.

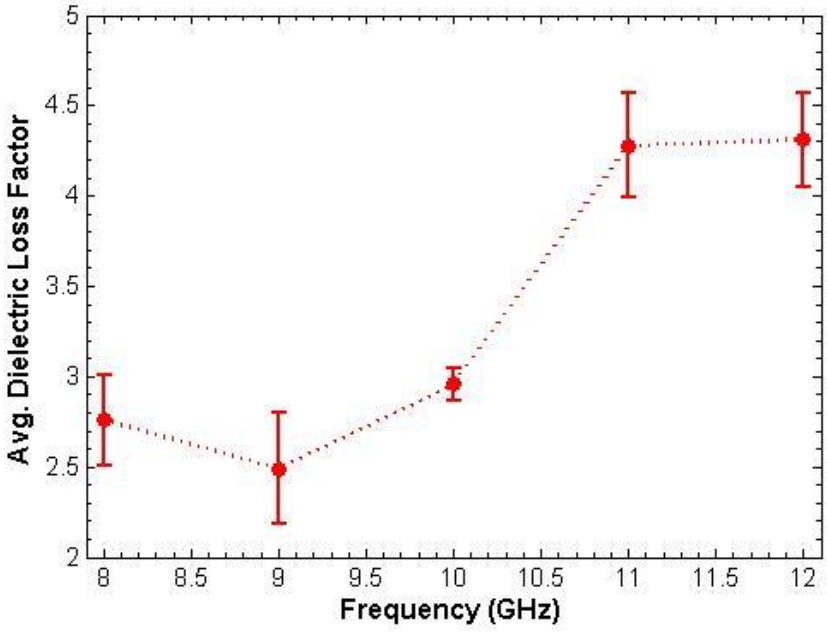

Figure 2.8: Average dielectric loss factor of three different sets of Honeybee samples.

The average and error measurement results of dielectric constant and dielectric loss factor for the three different sets of Honeybee samples are given in Table 2.1. The measurement error of the average dielectric constant is in the range of 3% to 11%, and 9% to 30% of the average dielectric loss factor. Such variations in error are natural and can be attributed to the inhomogeneous nature of biological tissue composition, because the complexity of the tissue structure and composition of Honeybees may alter the experimental results. In addition, a possible interpretation of measurement error can be the influence of air gaps between the bulk samples of Honeybee and the waveguide cross section. Although the dielectric mixture equation can help to eliminate the effects of air gaps, still some uncertainty is expected to occur.

Table 2.1: A summary of dielectric properties measurement of the Honeybee.

Frequency (GHz)	Avg. Dielectric Constant	Error	Avg. Dielectric Loss Factor	Error	Loss Tangent
8.2	10.69	0.069	2.76	0.25	0.26
9	10.81	0.032	2.49	0.31	0.23
10	11.63	0.077	2.96	0.09	0.26
11	11.31	0.11	4.28	0.29	0.38
12.4	10.59	0.075	4.31	0.26	0.41

There are disorganized differences in the dielectric properties of humans and animal species. The wildly differing tissue properties are even more apparent than differences between the species themselves. The biological tissue such as in insects and the human body is a complicated mixture of organs and materials with widely varying dielectric properties. However, the major component of human tissues is water, and this is the most important factor affecting the dielectric properties value. Most of the organs and tissues in the human body contain more than 70% water. On the other hand, insect tissues have lower water density in comparison to human tissues' water density. Normally, high water content species have high conductivity and fast dielectric relaxation

at high frequencies, whereas those with low water content have low conductivity and slow dielectric relaxation.

Much research has been performed on the dielectric properties of human tissues [29-33]. For example, Gabriel has compiled extensive data on various human tissues such as brain, muscle, kidney, and bone, in the frequency range 10 Hz to 20 GHz [33]. For tissues with higher water content, such as brain, muscle and kidney, the dielectric constant decreases almost linearly at higher frequencies from 80 to 20 for the range of frequency from 100 MHz to 20 GHz. Bone tissue has the lowest water content, and the dielectric constant decreases slowly from 20 to 10, as frequency increases from 1 MHz to 20 GHz, respectively.

A living Honeybee tissue is assumed to be almost dry, and it can be expected that most of the water content will be kept inside cells or the interstitial space of the tissues. To validate this assumption, a comparison of the dielectric constant between pure water, human tissues (wet), human tissues (dry), and Honeybee tissue is presented in Table 2.2. As shown in Table 2.2, the average value of the dielectric constant of the Honeybee tissue at 10 GHz is comparable with dry human tissues such as bones, which is consistent with the previous statement. Another observation, shown in Figures 2.7 and 2.8, is that slow dielectric relaxation is found in the case of the Honeybee for the frequency range from 10 to 12.4 GHz as the average dielectric constant decreases, with a consistent corresponding increase in the average dielectric loss factor at 10 GHz.

Table 2.2: Dielectric Property Comparison between Pure Water, Human Tissues (wet), Human Tissues (Dry), and Honeybee Tissue at 10 GHz

Materials	Dielectric Constant	Dielectric Loss Factor	Loss Tangent	Ref.
Pure water	10.69	2.76	0.26	34
Human tissues (wet)	10.81	2.49	0.23	33
Human tissues (dry)	11.63	2.96	0.26	33
Honeybee tissue	11.31	4.28	0.38	

2.6 References

[1] Skolnik, Merrill Ivan. "Radar handbook." (1970).

[2] Headlee, Thomas J., and Robert C. Burdette. "Some facts relative to the effect of high frequency radio waves on insect activity." *Journal of the New York Entomological Society* 37.1 (1929): 59-64.

[3] Kilgore, Wendell W., and Richard L. Doutt. *Pest control: biological, physical, and selected chemical methods*. Academic Press; New York; San Frncisco; London, 1967.

[4] Nelson, Stuart O., and W. K. Whitney. "Radio-frequency electric fields for stored grain insect control." *Transactions of the American Society of Agricultural Engineers* 3.2 (1960): 133-144.

[5] Nelson, S. O., L. H. Soderholm, and F. D. Yung. "Determining the dielectric properties of grain." *Agricultural Engineering*34.9 (1953): 608-610.

[6] Nelson, S. O., L. E. Stetson, and J. J. Rhine. "Factors influencing effectiveness of radio-frequency electric fields for stored-grain insect control." *Transactions of the ASAE* 9.6 (1966): 809-0815.

[7] Nelson, S. O., and L. F. Charity. "Frequency dependence of energy absorption by insects and grain in electric fields." *Transactions of the ASAE* 15.6 (1972): 1099-1102.

[8] Nelson, Stuart O. "Insect-control studies with microwaves and other radiofrequency energy." *Bulletin of the ESA* 19.3 (1973): 157-163.

[9] Nelson, S. O., and L. E. Stetson. "Comparative effectiveness of 39-and 2450-MHz electric fields for control of rice weevils in wheat." *Journal of Economic Entomology* 67.5 (1974): 592-595.

[10] Ondracek, J., and V. Brunnhofer. "Dielectric properties of insect tissues." *General physiology and biophysics* 3.3 (1984): 251-257.

[11] Nelson, S. O. "Radio-Frequency: and Microwave Dielectric Properties of Insects." *Journal of Microwave Power and Electromagnetic Energy* 36.1 (2001): 47-56.

[12] Colpitts, B., Y. Pelletier, and S. Cogswell. "Complex permittivity measurements of the Colorado potato beetle using coaxial probe techniques." *Journal of Microwave Power and Electromagnetic Energy* 27.3 (1992): 175-182.

[13] Andreueeetti, D., et al. "Microwave destruction of woodworms." *Journal of Microwave Power and Electromagnetic Energy* 29.3 (1994): 153-160.

[14] Nelson, Stuart O., P. G. Bartley, and Kurt C. Lawrence. "Measuring RF and microwave permittivities of adult rice weevils." *IEEE Transactions on Instrumentation and Measurement* 46.4 (1997): 941-946.

[15] Nelson, S. O., P. G. Bartley, and K. C. Lawrence. "RF and microwave dielectric properties of stored-grain insects and their implications for potential insect control." *Transactions of the ASAE* 41.3 (1998): 685.

[16] Ikediala, J. N., et al. "Dielectric properties of apple cultivars and codling moth larvae." *Transactions of the ASAE* 43.5 (2000): 1175.

[17] Vangemert, M. J. "High-frequency time-domain methods in dielectric spectroscopy." *Philips Research Reports* 28.6 (1973): 530-572.

[18] Von Hippel, Arthur R. *Dielectric Materials and Applications* (1966).

[19] Stuchly, Stanislaw S., and Miroslaw Matuszewski. "A combined total reflection-transmission method in application to dielectric spectroscopy." *IEEE Transactions on Instrumentation and Measurement* 27.3 (1978): 285-288.

[20] Ligthart, Leo P. "A fast computational technique for accurate permittivity determination using transmission line methods." *IEEE Transactions on Microwave Theory and Techniques* 31.3 (1983): 249-254.

[20] Van Beek, L. K. H. "Dielectric behaviour of heterogeneous systems." *Progress in dielectrics* 7.71 (1967): 113.

[21] Tinga, W. R. "Mixture laws and microwave-material interactions." *Dielectric Properties of Heterogeneous Materials*, 6 (1992): 40.

[22] Banhegyi, G. "Comparison of electrical mixture rules for composites." *Colloid and polymer science* 264.12 (1986): 1030-1050

[23] Sihvola, Ari H. *Electromagnetic mixing formulas and applications*. No. 47. IET, 1999.

[24] Grosse, Constantino, and Jean-Louis Greffe. "Permittivite statique des emulsions." *Journal de Chimie Physique* 76 (1979): 305-327.

[25] Greffe, J. L., and C. Grosse. "Static permittivity of emulsions." *Progress In Electromagnetics Research* 6 (1992): 41-100.

[26] Nelson, Stuart O. "Useful relationships between dielectric properties and bulk densities of granular and powdered materials." *Am. Inst. Chem. Eng. Ann.* (2004): 136-140.

[27] Dube, D. C. "Study of Landau-Lifshitz-Looyenga's formula for dielectric correlation between powder and bulk." *Journal of physics D: Applied physics* 3.11 (1970): 1648.

[28] Nelson, S. O. "RF and microwave permittivities of insects and some applications." *URSI EMTS International Symposium on Electromagnetic Theory, 1224e1226*. 2004.

[29] Baker-Jarvis, James R., et al. *Characterization of tissue-equivalent materials for high-frequency applications (200 MHz to 20 GHz)*. No. Technical Note (NIST TN)-1554. 2010.

[30] Schwan, H. P. "Linear and nonlinear electrode polarization and biological materials." *Annals of biomedical engineering* 20.3 (1992): 269-288.

[31] Epstein, B. R., and K. R. Foster. "Anisotropy in the dielectric properties of skeletal muscle." *Medical and Biological Engineering and Computing* 21.1 (1983): 51.

[32] Stuchly, M. A., and S. S. Stuchly. "Electrical properties of biological substances Biological Effects and Medical Applications of Electromagnetic Energy ed OP Gandhi." (1990).

[33] Gabriel, Sami, R. W. Lau, and Camelia Gabriel. "The dielectric properties of biological tissues: II. Measurements in the frequency range 10 Hz to 20 GHz." *Physics in Medicine & Biology* 41.11 (1996): 2251.

[34] Von Hippel, A. R. "The dielectric relaxation spectra of water, ice, and aqueous solutions, and their interpretation. I. Critical survey of the status-quo for water." *IEEE Transactions on Electrical Insulation* 23.5 (1988): 801-816.

Chapter 3

Prediction of Radar Scattering Characteristics of Airborne Insects by Utilizing Electromagnetic Modeling

3.1 Introduction

For decades, radar has been used to observe and monitor aerial animals [1-4]. Nowadays, radar has started to play a valuable role in entomology for investigating the behavior of flying insects beyond the visible range and contributing to much developmental research into biological and ecological advances [5-11]. Although radar has proven to be a powerful tool in these applications, its utility for detecting and distinguishing between different biological targets is limited. Biological target identification has always been a challenge in entomological radar applications. In these applications, the electromagnetic energy is radiated to and reflected (echoed) back from the intercepting target, which provides an accurate measurement for locating the target [12-13]. The intensity of the echo is described explicitly by the radar cross section (RCS) of the object. Values of the RCS are dependent on a number of factors, such as the size, shape, material, and aspect of the target, as well as the wavelength and polarization of the transmitted radiation with respect to the orientation of the target.

The lack of understanding of how airborne insects interact with radio waves limits our ability to develop a classification system for biological observations from radar data. There have been several efforts at experimental measurement to understand interactions of aerial animals, i.e. insects, using radio waves [14-19]. Although these interactions have produced a plethora of radio wave scattering information, they often only report the measurements at select frequencies, observable angles, and polarizations. In addition, these measurements are also complex and expensive to build and operate, and they typically lack full azimuthal radio scattering data or

elevation angles radio scattering data, or both. To overcome radar entomology limitations in qualitative analysis and interpretation, we need a standardized technique for quantifying radio wave scattering at multiple frequencies or polarizations and diverse viewing angles. Indeed, this technique should get validation from both an analytical model and associated experimental studies.

In the early 20th century, extensive analytic studies describing electromagnetic radiation interactions with simple physical objects were proposed [20]. However, adequate solutions for objects with more complex shapes have not been proposed. Recently, several numerical approaches have estimated the RCS values for different objects, but with little research on airborne species [21-23].

To determine the RCS of complex objects, such as insects, solving Maxwell's equations in their general form is required. However, solving Maxwell's equations is almost impossible for an inhomogeneous geometrical shape. To overcome this, a numerical solution of some variation of Maxwell's equations is needed in either integral or differential form. Generally, computational electromagnetics method (CEM) techniques have been developed and implemented to solve various similar problems [26]. A block diagram of these methods is illustrated in Figure 3.1.

The exact methods are based on either the integral or differential form of Maxwell's equations. In general, there are three well-known methods: method of moments (MoM), finite difference time domain (FDTD), and the finite element method (FEM) for physically rigorous solution or full-wave methods [24-30]. The MoM obtains the solution of integral equations in the frequency domain, while the FDTD finds solutions of the differential equations in the time domain. The finite element method (FEM) is also used in both the time and frequency domains. The Fourier transform provides a relationship between time and frequency domain solutions. Due to the requirement of high computer resources at high frequencies, these methods are sometimes

identified as low frequency. These methods are often used for relatively simple or relatively small objects in the Rayleigh and Resonant regions.

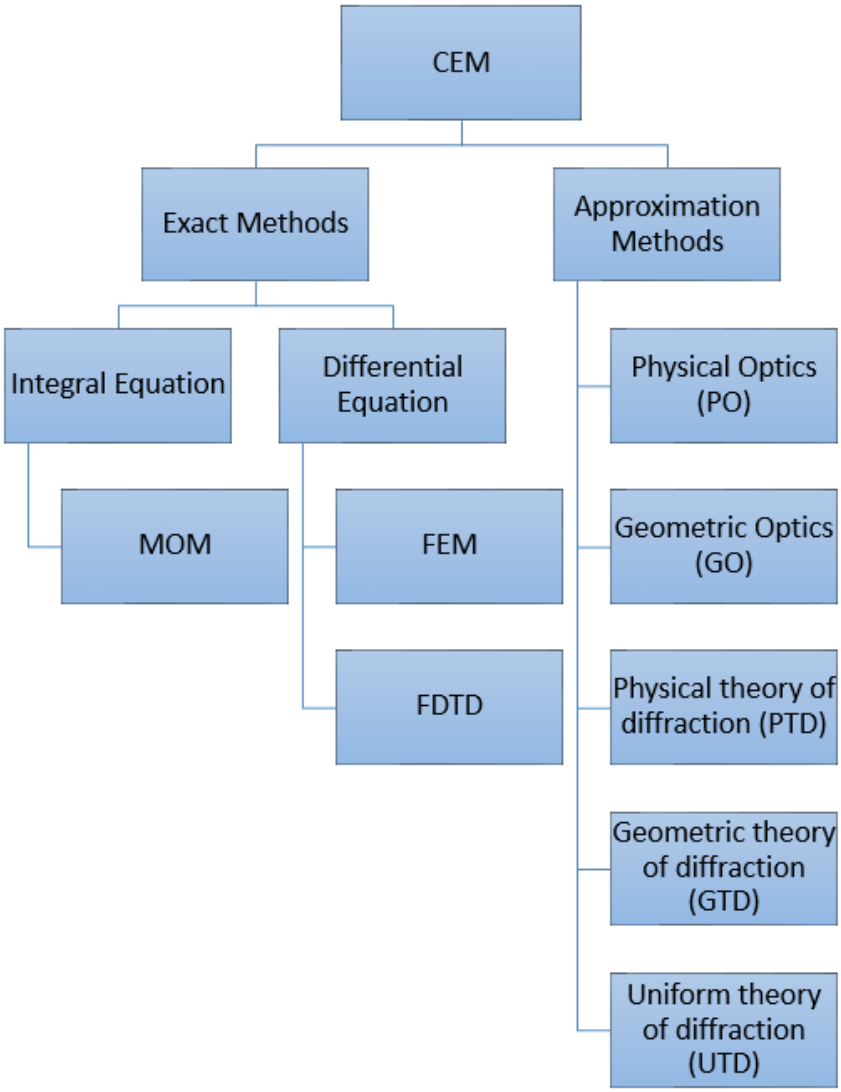

Figure 3.1: Computational hierarchy.

In contrast to the exact methods, approximation methods have been developed for the optics region to handle electrically large problems. These methods are also called high-frequency solution methods, since they are effective at high frequencies. The approximate high frequency

methods are mainly based on geometrical optics (GO) or physical optics (PO), physical theory of diffraction (PTD), geometric theory of diffraction (GTD) and uniform theory of diffraction (UTD).

Commonly, radar targets can be defined on the three RCS frequency regions based on their body size in wavelengths. These regions are identifiable for most structures: the Rayleigh region (low-frequency region), the Mie region (Resonant region or medium-frequency), and the optical region (high-frequency region). The RCSs of insects are little understood; anyway, available results suggest that the general scattering characteristics of insects at a wavelength of 3.2 cm (X-band) occurs at the high end of the Rayleigh region or at the Resonant region, depending on insect size [17, 31]. In such cases, choosing an accurate numerical simulation technique becomes critical for applications in which dielectric scattering objects such as insects have a size comparable to the probing wavelength. Therefore, the only accurate way to resolve the RCS calculations of these applications is to use the exact methods [23].

In the present study, we have developed a reliable Honeybee model and predict its radar scattering characteristics using the method of moments (MoM) implemented in the FEKO software package. The backscattering cross sections of the Honeybee worker (i.e., Apis Mellifera) model are calculated for both horizontal and vertical polarization cases. Both types of cross sections were calculated to determine the general magnitude of Honeybee backscattering cross sections and to study polarization dependence of the cross sections at multiple frequencies and viewing angles.

3.2 The Method of Moments (MoM) and FEKO Modeling Software

Many commercial software packages are available to handle RCS calculations. The FEKO is a comprehensive electromagnetic simulation software tool based on state-of-the-art CEM

techniques, developed by Altair engineering [32]. Solutions to various numerical problems are facilitated in FEKO by numerous techniques. For problems with large electrical size and low level of material/structure complexity, approximate methods suffice such as the Uniform Theory of Diffraction (UTD), Physical Optics and Geometrical Optics (GO). For studies involving objects with a smaller electrical size but more complex and intricate details, exact techniques like the Finite Element Method (FEM), Finite Difference Time Domain (FDTD) and Method of Moments (MoM) become more favorable. Note that with these latter techniques, computational effectiveness faces practical limitations. In particular, in cases where the size of the object(s) become large relative to a wavelength, as with high frequency sweeps, the size of the simulation mesh increases as a consequence of domain discretization. Consequently, computational time may increase significantly.

The main algorithmic technique of FEKO is the method of moments (MoM). It is also combined with other techniques, such as Physical Optics (PO), Geometric Optics (GO), the Finite Element Method (FEM), Multilevel Fast Multipole Method (MLFMM), and so on. This variety of numerical methods in FEKO makes it possible to utilize FEKO software for a wide range of electromagnetic problems. Applications include cable modeling, antenna design, dielectric media, RCS analysis and many more.

Accurate prediction of target RCS is critical in order to describe the amount of scattered power from a target towards the radar. Radar designers consider the perfectly electric conducting (PEC) sphere to be the simplest target to examine the plane wave scattering as the reference because of its symmetry. This is used to measure scattering properties such as RCS of the other targets. Following several developments from various authors [20, 33-35], the normalized exact backscattered RCS for a perfectly conducting sphere is a Mie series given by:

$$\frac{\sigma}{\pi r^2} = \left(\frac{j}{kr}\right)\sum_{n=1}^{\infty}(-1)^n\,(2n+1)\left[\left(\frac{krJ_{n-1}(kr) - nJ_n(kr)}{krH_{n-1}^{(1)}(kr) - nH_n^{(1)}(kr)}\right) - \left(\frac{J_n(kr)}{H_n^{(1)}(kr)}\right)\right] \qquad (3.1)$$

where r is the radius of the sphere, $k = \frac{2\pi}{\lambda}$, λ is the wavelength, J_n is the spherical Bassel of the first kind of order n, and $H_n^{(1)}$ is the Hankel function of order n, and is given by

$$H_n^{(1)}(kr) = J_n(kr) + jY_n(kr) \qquad (3.2)$$

where Y_n is the spherical Bessel function of the second kind of order n.

These Hankel and Bessel functions are not easily calculated analytically and must be done numerically on a computer. The electromagnetic software FEKO was implemented to simulate and predict the RCS of a PEC sphere as a function of its electrical size, as illustrated in Figure 3.2.

The method applied in FEKO is an exact solving technique known as the Method of Moments (MoM), used to simulate the RCS of PEC sphere. The Method of Moments divides the PEC sphere surface into a collection of discrete patches. For each patch on the surface, the electric and magnetic field boundary conditions are applied to create an equivalent matrix of induced surface electric and magnetic currents. Each current is defined as a product of a higher-order known functional basis with an unknown coefficient, for which the matrix system is solved. Across the surface of the sphere, the total solution of these currents is formed from a combination of these coefficients with their corresponding basis functions. Then, they are inserted into Maxwell's equations to produce the resulting scattered electromagnetic field.

The scattering results in Figure 3.3 are computed for the sphere of fixed radius $a = 3\,mm$ as shown in Figure 3.2 over the frequency range from 1.6 GHz to 500 GHz, to span the entirety of the Rayleigh, Mie and Optical regions. This radius was picked because it emulates the volume of a Honeybee closely. The regions are split according to the parameter ka, where ka given as $2\pi a/\lambda$, which is the circumference of the sphere expressed in wavelengths. The RCS is considered to be in the Rayleigh region when $ka < 1$. It is considered to be in the Optics region when $ka > 10$. If ka falls between 1 and 10 then it is considered to be in the Resonance region [12].

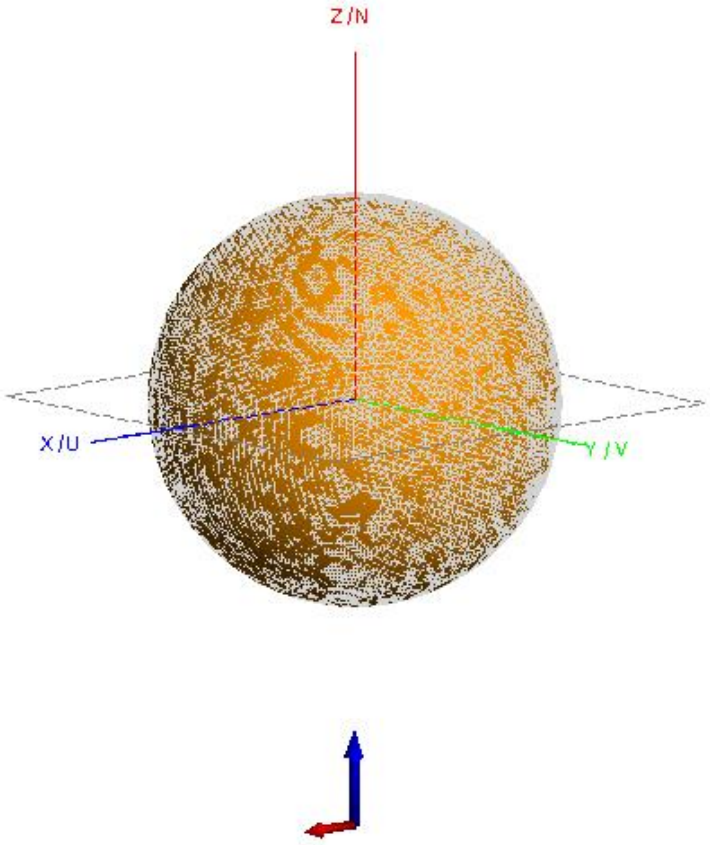

Figure 3.2: 3D-PEC sphere modeled on FEKO.

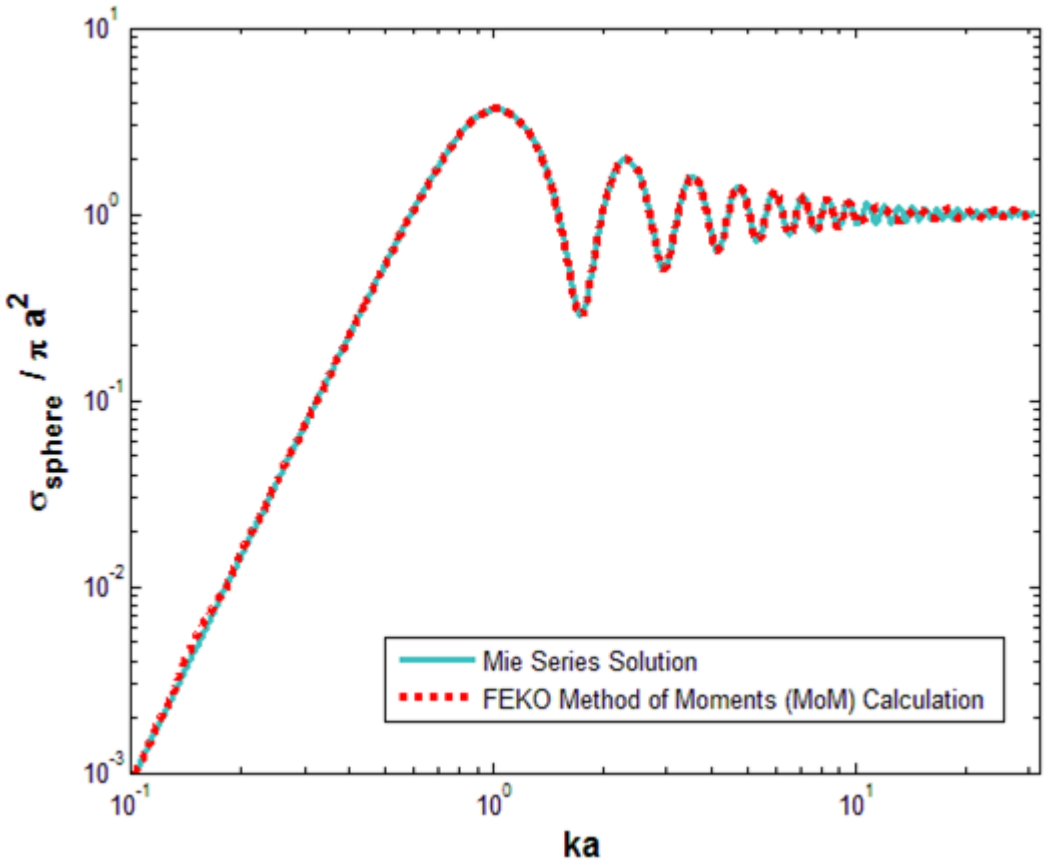

Figure 3.3: The computed RCS Results of a perfectly conducting sphere, acquired from method of moments (MoM) solver implemented in the FEKO software package and Mie series solution, where a is the radius of the sphere. The parameter $ka = {}^{2\pi a}/_{\lambda}$ is the circumference of the sphere expressed in wavelengths.

Note that there exists a high degree of correlation between the analytical Mie series solution and that obtained using the FEKO MoM computation. This agreement places confidence in FEKO's ability to capture related effects in subsequent studies of Honeybee RCS under varying states and conditions.

3.3 Organismal Honeybee model in FEKO software

To produce realistic scattered fields of a Honeybee, one must develop an organismal Honeybee model that includes as much detail as possible. The three main parts of a Honeybee are the head, thorax, and abdomen, with fine details such as six legs, a pair of antenna, compound eyes, and wings obtained from SolidWorks 3D Computer Aided Design (CAD) software [36] and imported into electromagnetic software FEKO, as shown in Figure 3.4, for RCS calculation and analysis. The backscattering cross sections are calculated for both horizontal and vertical polarizations. The horizontal cross section refers to the electric field of the calculating scattering radiation oriented parallel to the model of the Honeybee body, whereas the vertical cross section refers to the electric field orientated perpendicular to the model of the Honeybee body, as illustrated in Figure 3.5.

For comparison, another simplified model was defined as a sphere with size comparable with that of the Honeybee volume. In general, the volume of the Honeybee is in the range of $100 - 150\ mm^3$ and was measured using the liquid displacement method in a graduated cylinder, as described in Chapter 2. The sphere of fixed radius $a = 3\ mm$, representing the volume of the Honeybee, was modeled in FEKO software for backscattering cross sections calculation.

Our goal is to develop a model that matches RCS signatures of the living Honeybee. After defining the geometric structure of the Honeybee, the complex relative permittivity obtained by dielectric properties measurements in Chapter 2 was used, and are discussed in more detail there. The complex relative permittivity of $\varepsilon = 10.81 - j2.49$ with a loss tangent of $tan\delta = 0.23$ were assigned to the entire body parts of the modeled Honeybee. To avoid creating internal boundaries and complexity in the model, the wings are modelled as 1-nm thin dielectric sheets (TDS) with the same permittivity as the rest of the body parts.

The Honeybee model time requirement and computational complexity for the backscattering cross section calculations depend directly on the calculated number of coefficients of the MoM solution. The total number of these coefficients can be obtained through the structural elements of the model and its electric properties. To reduce the number of unknowns by almost half, the option of symmetry was employed, which results in a reduction in computational complexity. Therefore, the result of solving for these unknowns will be considered as the solution of the induced currents across the surface of the Honeybee. Consequently, this solution can also be used to solve for the complex scattering matrix, and therefore RCS, using Maxwell's equations.

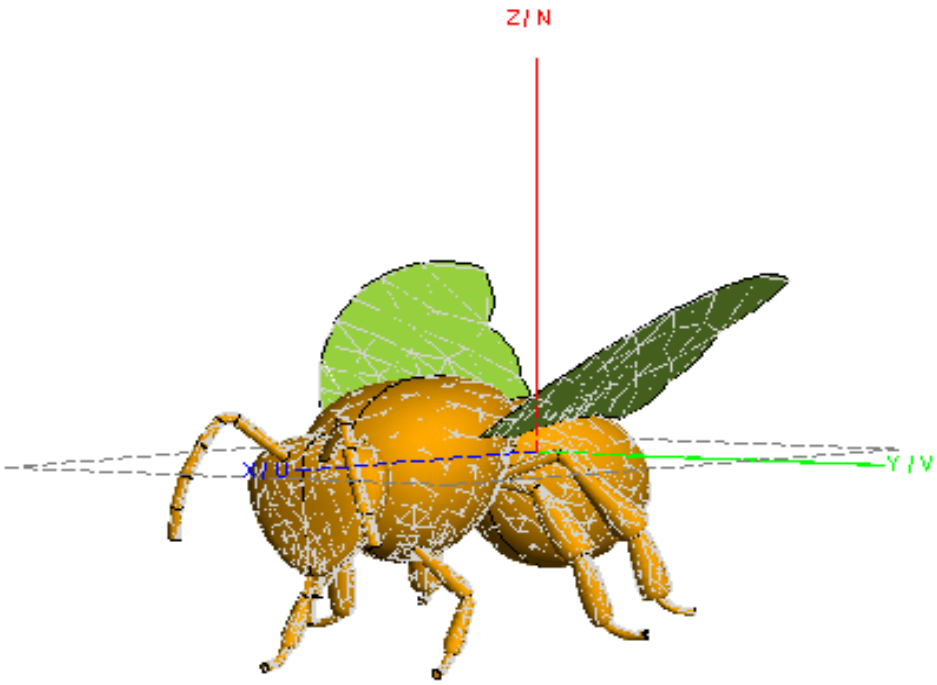

Figure 3.4: 3-D view of the Honeybee model in FEKO software using the Method of Moments (MoM) calculations to find the backscattering cross sections assuming a probing wavelength of 3.2 cm (9.41 GHz).

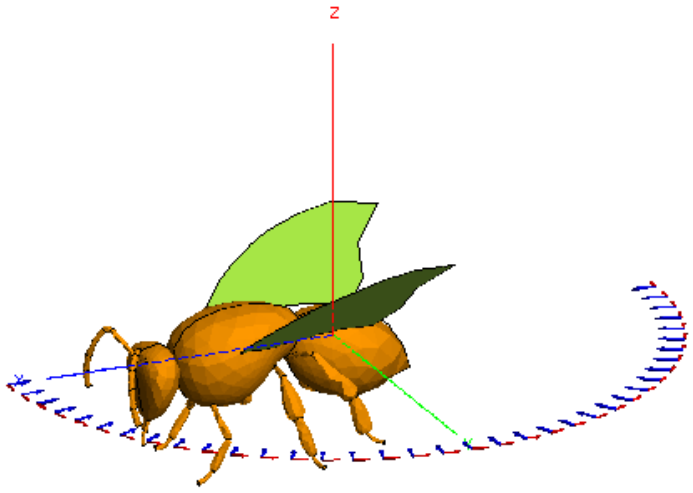

(a)

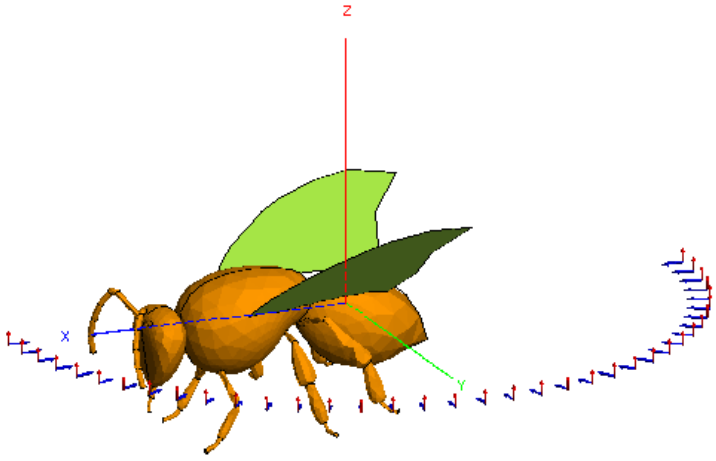

(b)

Figure 3.5: Illustration of the polarization backscattering cross sections of the Honeybee as function of incident angle (a) Horizontal polarization (b) Vertical polarization.

3.4 Results and Discussion

To simply examine and predict the backscattering cross sections of the Honeybee, the PEC sphere that has an equivalent volume to the Honeybee volume was modeled in FEKO software and excited by an incident plane wave for RCS calculation. To further investigate the effect of Honeybee dielectric composition on the backscattering cross section value, the measured dielectric constant of $\varepsilon' = 10.81$ with a loss tangent of $tan\delta = 0.23$ of Honeybee body tissue was assigned for another sphere. Figure 3.6 compares the computed results for the RCS of PEC and dielectric spheres of fixed radius $a = 3\,mm$ over the frequency range from 1 to 100 GHz. The backscattering cross sections of the PEC sphere are generally larger than the backscattering cross sections of the dielectric sphere. However, in this case the difference between the PEC and the dielectric sphere models is minimal. The small backscattering cross section of the dielectric sphere can be attributed to its lower reflection coefficient, and to losses in the material that converts part of the incident wave energy into heat.

At the Rayleigh region, the RCS of both spheres increases as frequency increases, reaching a maximum of -40 dBsm at 16 GHz. In the Mie or Resonance region above 16 GHz, where both spheres' dimension and wavelength are in the same order, the RCS of both spheres varies in a complex way for relativity small frequency shifts, due to the interference between the main reflection and the creeping wave of the sphere at a particular wavelength. Because the dielectric sphere is lossy, the RCS of the dielectric sphere exhibits larger variation, with deep nulls at a particular frequency, than the PEC sphere. Surprisingly, the RCS in the high end of the Rayleigh region of both modeled spheres is

approximately around the measured backscattering cross sections of Honeybee at X-band, as reported in previous studies [15, 18]; however, no indication of the variation with aspect and the plane of polarization is observed. This is due to the RCS of a sphere being independent of these parameters.

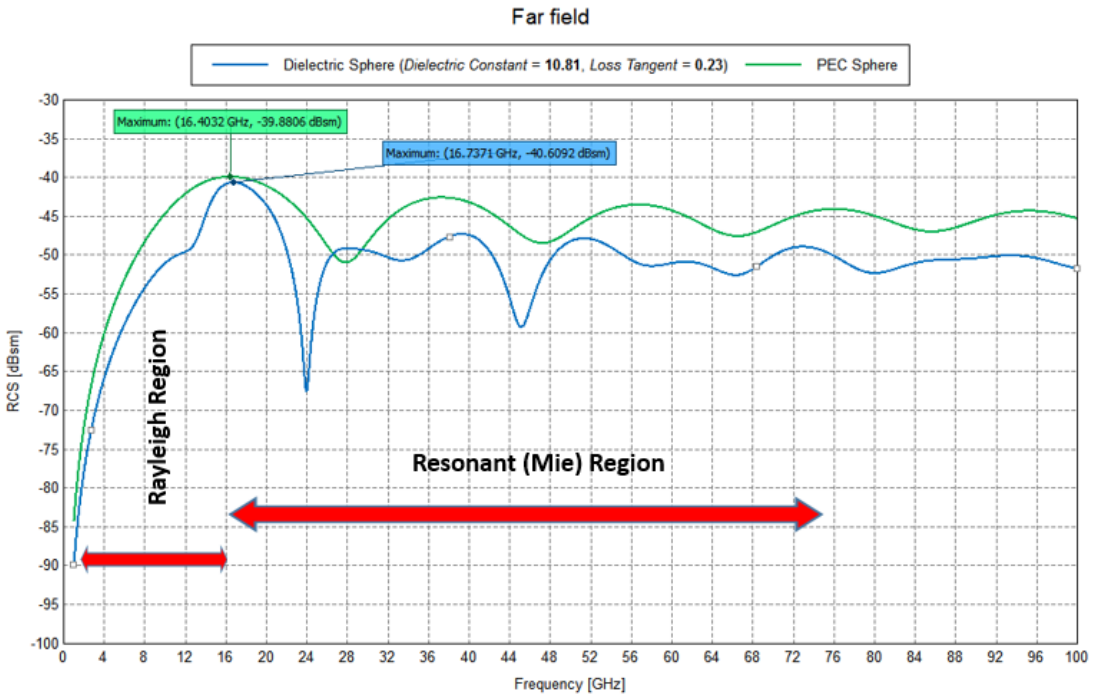

Figure 3.6: The computed RCS results of the PEC and dielectric spheres, created using the method of moments (MoM) solver implemented in the FEKO software package.

To further predict the general shape and magnitude of Honeybee backscattering cross sections, and to study the polarization dependence of the cross sections at different frequencies and viewing angles, the complex scattering matrix of the organismal model of Honeybee in FEKO software is calculated for horizontal and vertical polarizations over all solid angles of incident. The incident angle of the plane wave is $\theta = 90^{\circ}$ and $0^{\circ} \leq \varphi \leq 180^{\circ}$. The azimuth angle was

incremented by 5 degrees. The results of the RCS calculations are summarized in Figures 3.7-3.20 and given in rectangular diagrams, expressed in dBsm. The Honeybee's head (Head-on) and abdomen (End-on) correspond to azimuth angles of 0° and 180°, respectively.

At S, C, and X bands (2-12 GHz), Figures 3.7-3.9 show that the RCS curves are relatively smooth, and maximum backscattering occurs at 90° in azimuth, that is, when the Honeybee is broadside-on to the incident wave for horizontal and vertical polarizations. The minimum backscattering coincides with head-on and end-on positions of the Honeybee, with respect to the incident wave. It can be observed from Figure 3.9 (a), at 90° in azimuth, that the maximum magnitude of the backscattering cross sections of the Honeybee modeled is about -43 dBsm when the incident wave is polarized horizontally at 9.41 GHz, which incidentally is close to the first reported laboratory measurements in 1966 [8]. The RSC results at S, C, and X bands indicated this in the Rayleigh scattering region, since their RCS exhibit relatively smooth variations with aspect. Similarly, the overall backscattering magnitudes at these bands are quite similar to backscattering magnitudes corresponding to the dielectric sphere in the Rayleigh region with similar dielectric composition and volume size of Honeybee. Moreover, the results also indicate that the magnitude of the backscattering cross sections of the Honeybee is greatly dependent on the polarization of the incident wave. In these bands, the RCS curves are generally larger and smaller when the incident electric field vector is polarized horizontally and vertically along the Honeybee's body, respectively. However, the difference in the magnitude backscattering cross section between the horizontal and vertical is not quite as large. This is because Honeybee body length is not much greater than its body diameter. For example, at 9.41 GHz specifically at 90° in azimuth, the horizontal and vertical cross sections differ by about 8 dBsm; at 0° and 180° in same frequency, the difference is almost negligible.

At higher frequencies, such as Ku, K, Ka bands (12-40 GHz), Figures 3.10-3.12 show the backscattering cross section magnitudes of the Honeybee modeled does not increase significantly,

but varies considerably. When compared to lower frequencies (S, C, and X bands), deep nulls are observed from some angles at the higher frequencies. These results indicate that the RCS at these bands are in the interference scattering region, since the RCS becomes very sensitive and exhibits rapid and complex variations in aspect.

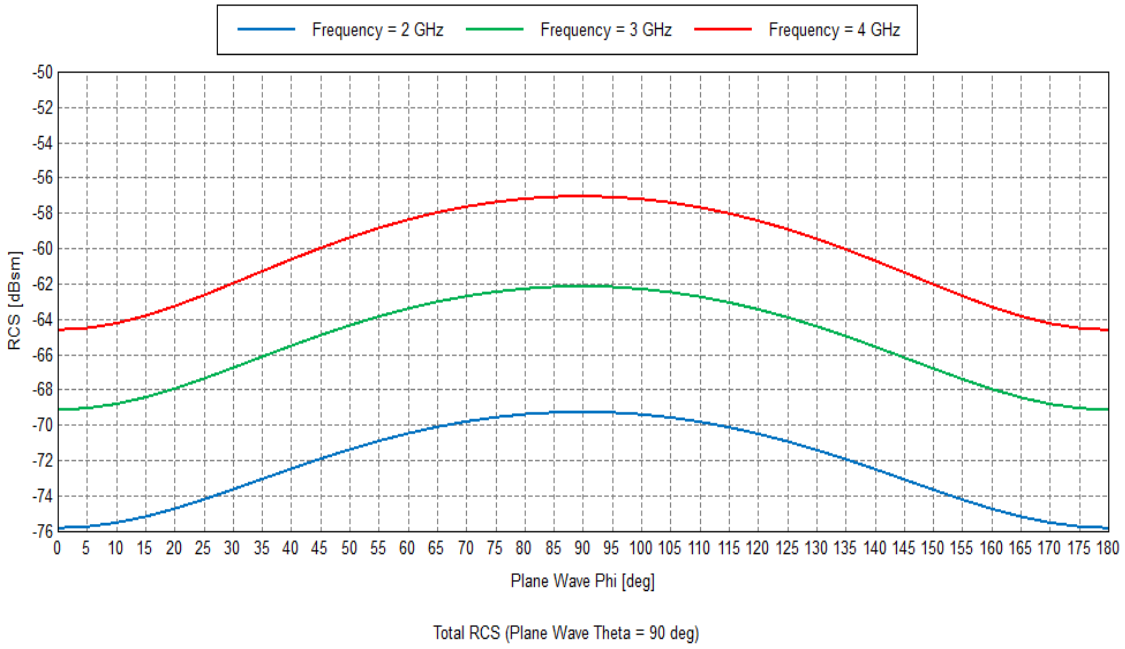

(a)

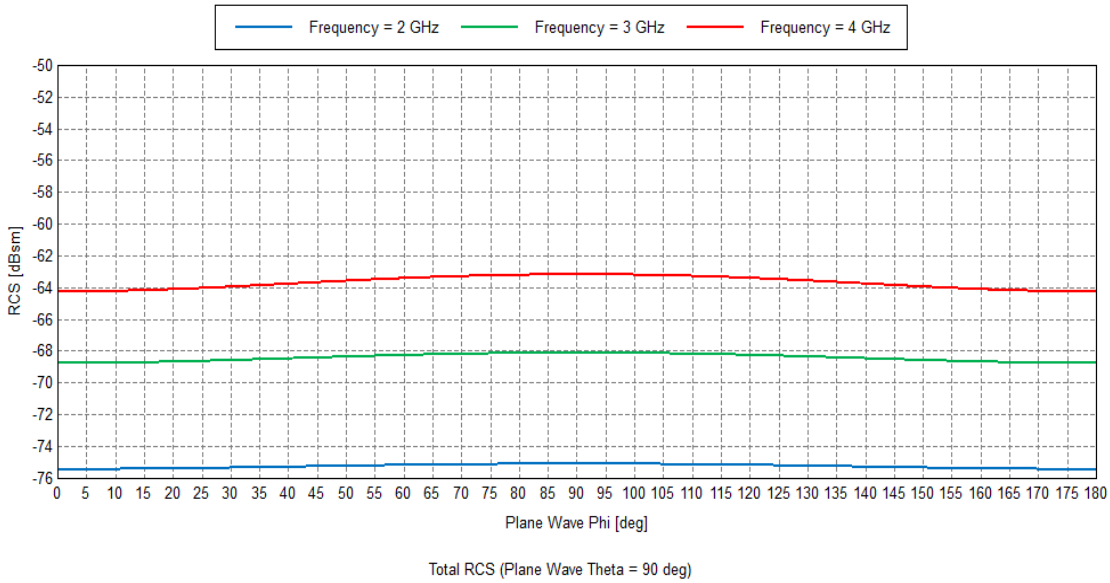

(b)

Figure 3.7: The backscattering cross sections of the Honeybee as function of incident angle at S-band (a) Horizontal Polarization (b) Vertical Polarization.

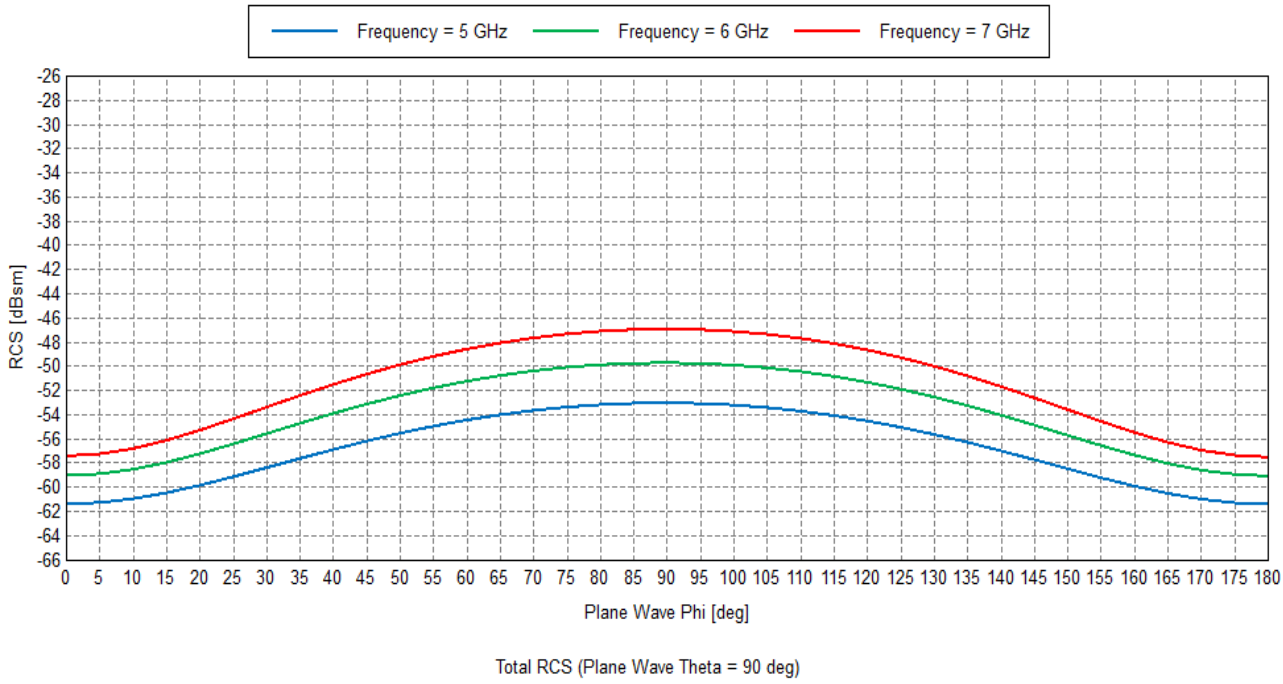

(a)

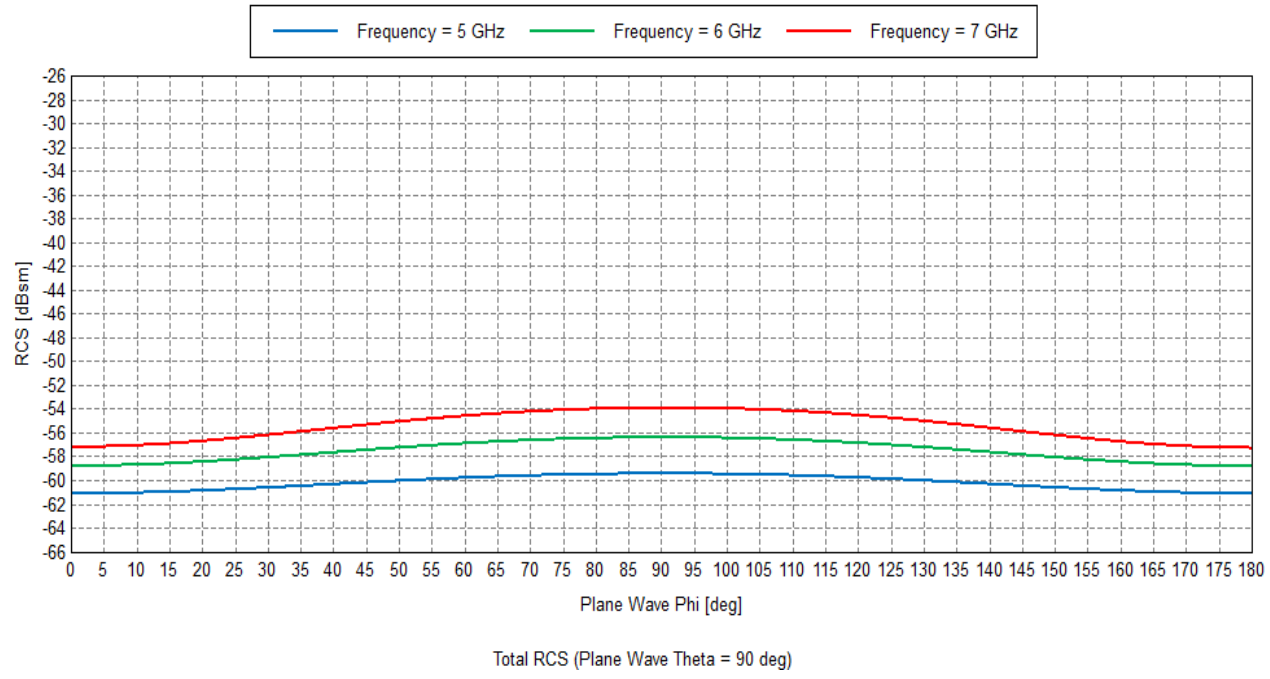

(b)

Figure 3.8: The backscattering cross sections of the Honeybee as function of incident angle at C-band (a) Horizontal Polarization (b) Vertical Polarization.

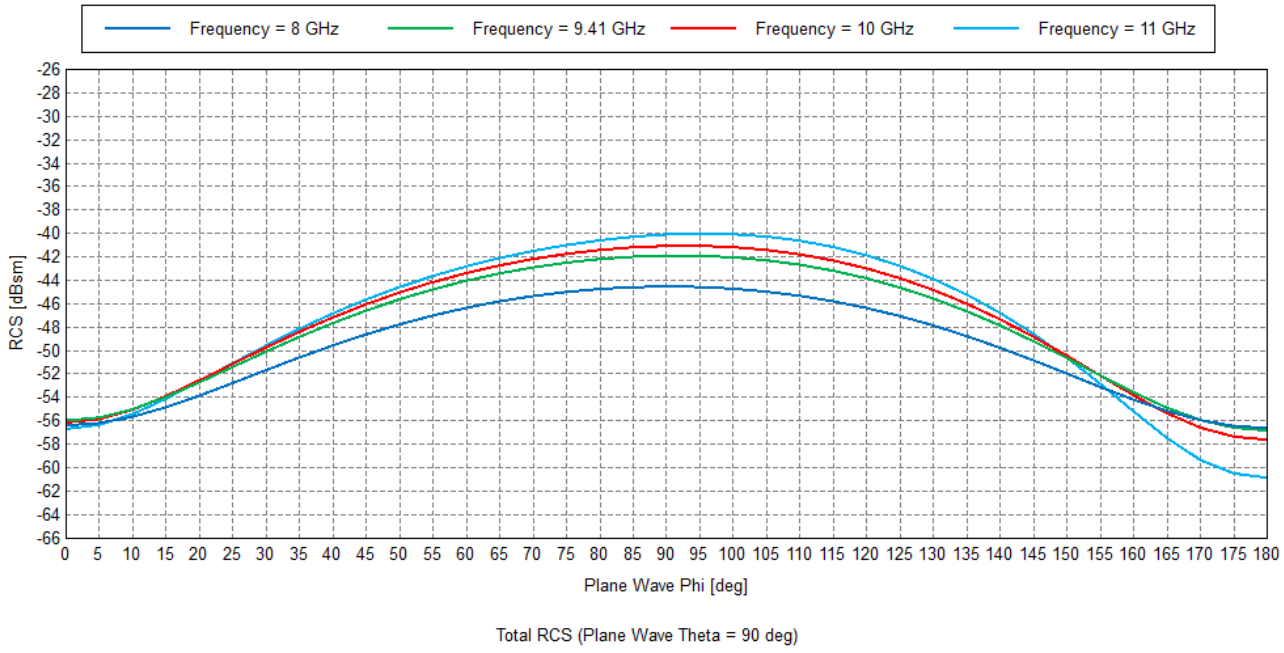

(a)

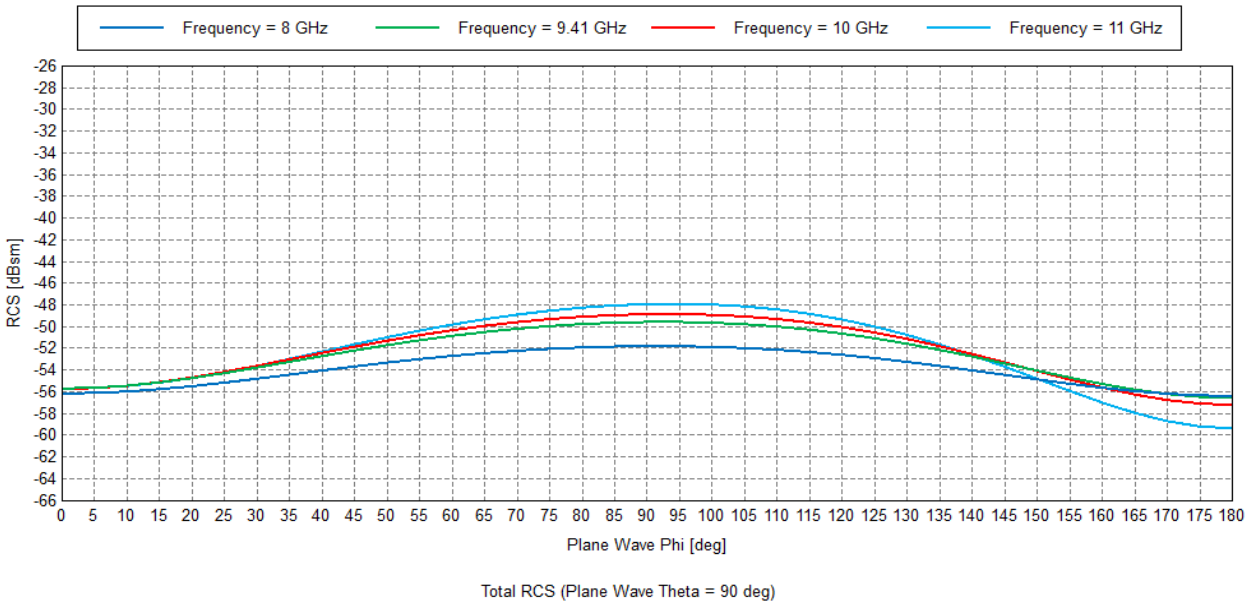

(b)

Figure 3.9: The backscattering cross sections of the Honeybee as function of incident angle at X-band (a) Horizontal Polarization (b) Vertical Polarization.

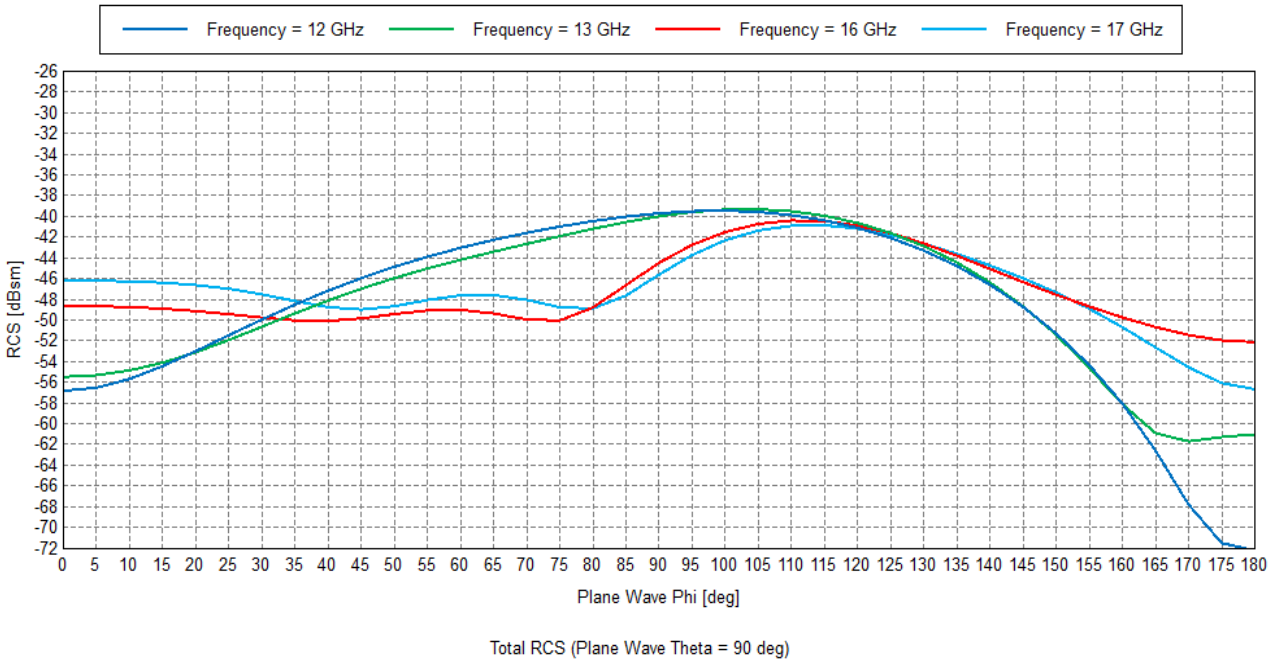

(a)

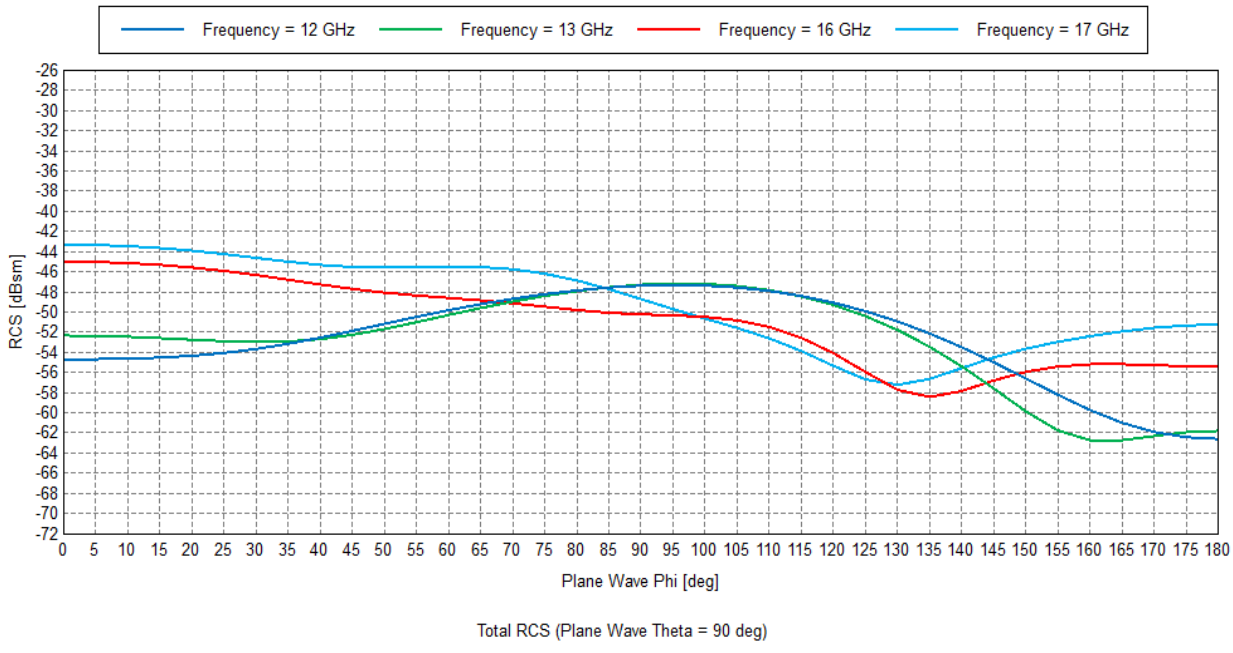

(b)

Figure 3.10: The backscattering cross sections of the Honeybee as function of incident angle at Ku-band (a) Horizontal Polarization (b) Vertical Polarization.

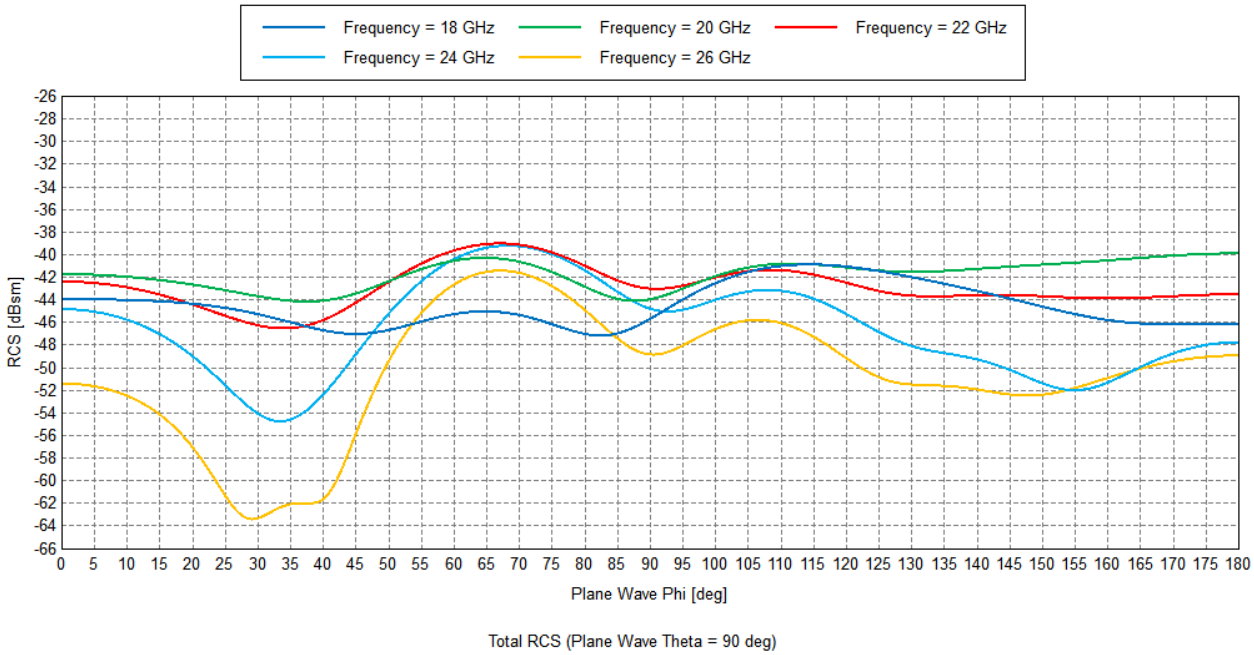

(a)

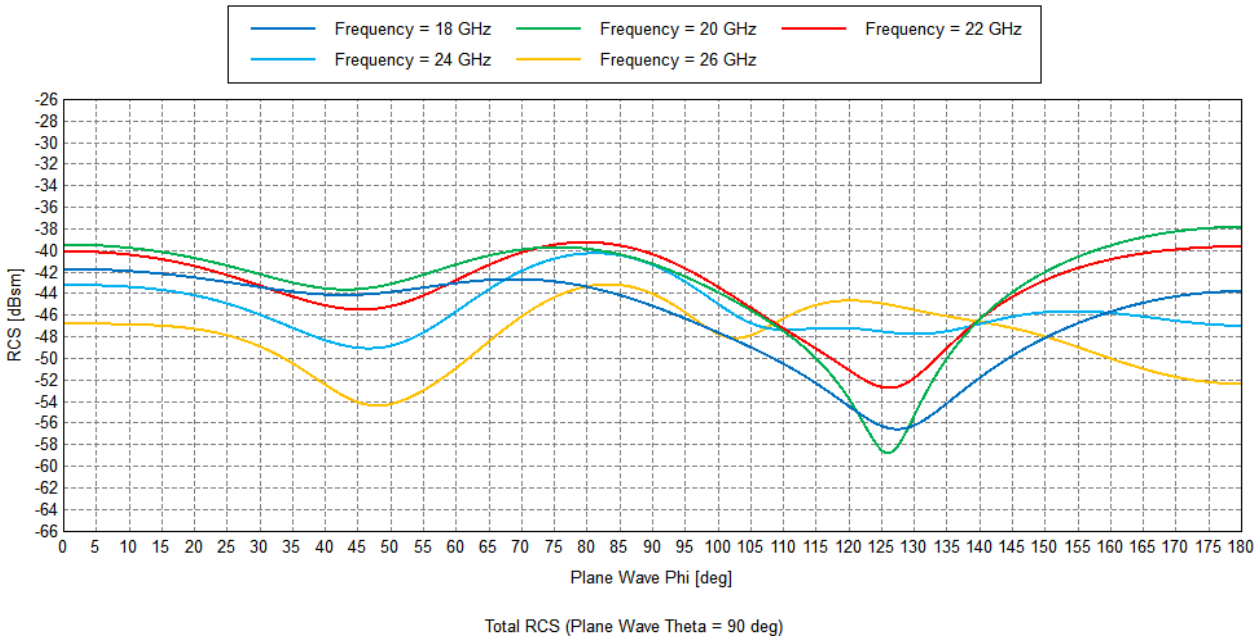

(b)

Figure 3.11: The backscattering cross sections of the Honeybee as function of incident angle at K-band (a) Horizontal Polarization (b) Vertical Polarization.

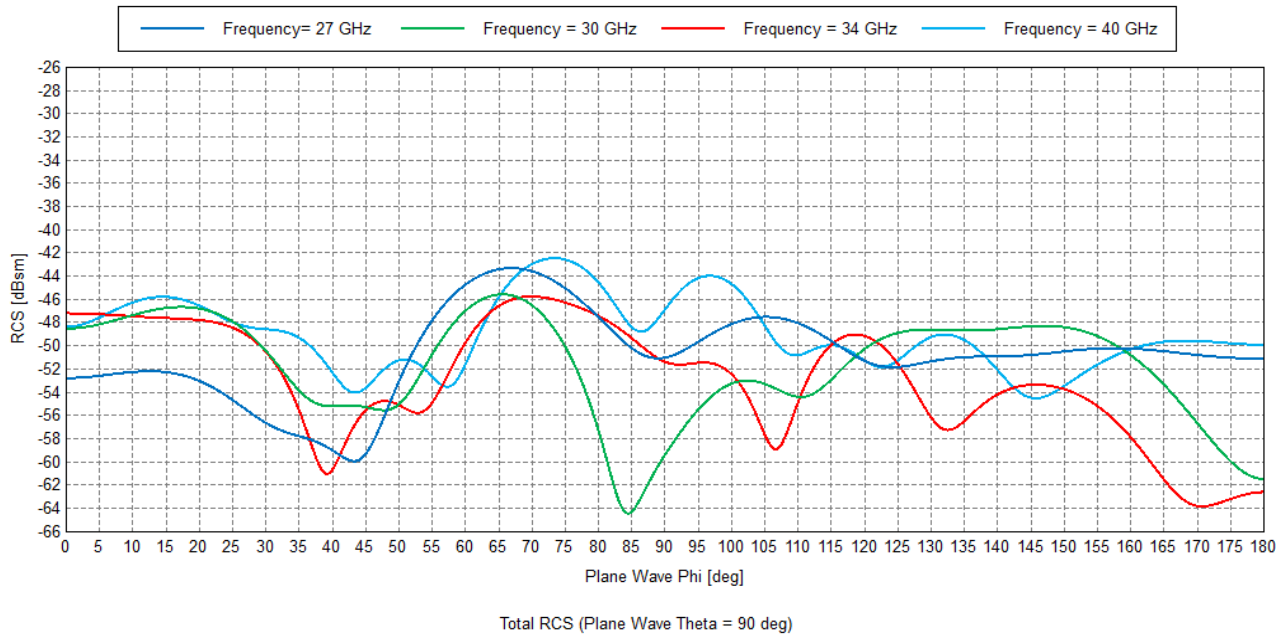

(a)

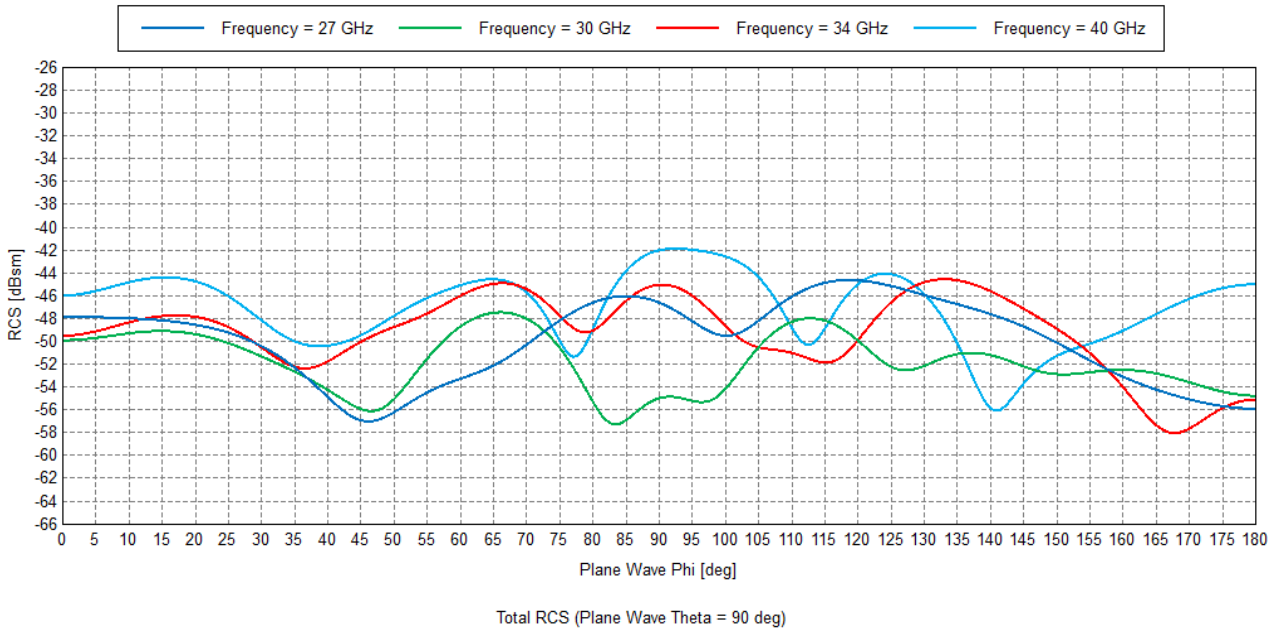

(b)

Figure 3.12: The backscattering cross sections of the Honeybee as function of incident angle at Ka-band (a) Horizontal Polarization (b) Vertical Polarization.

A study was done by Riley in 1985 where different sizes of insects were exposed to both horizontally- and vertically-polarized waves at the X-band frequency [17]. This resulted in two observations. Firstly, the smaller insects, where the diameter of the insect is much smaller than the probing wavelength, had its horizontally polarized cross section higher than its vertically polarized cross section. Secondly, for larger insects, where the body diameter of the insect is much closer to the probing wavelength, the vertically polarized cross section was higher. This observation made by Riley also shows here, where as the wavelength gets closer to that of the Honeybee body diameter (at W-band), the vertically-polarized cross section is higher than the horizontally-polarized cross section. This is shown in Figures 3.13-3.14. However, the backscattering cross section magnitude does not increase significantly, but the deep nulls are more apparent than the previously observed results at the lower end of the frequency spectrum (Ku, K, Ka bands).

Also, it should be noted that in our study, dielectric properties were measured at X-band (8.2-12.4 GHz) and then were assigned for the Honeybee model. The dielectric response of biological materials is always frequency dependent [37-38]. Small errors in backscattering cross sections magnitude of the Honeybee modeled at other bands are possible. In addition, the variability of the dielectric properties across Honeybee body parts could affect the shape and magnitude of the backscattering cross section. This is because the head, thorax, and wings are typically dry, while the abdomen and the rest of the internal body parts have varying amounts of water content in them. The varying water content in the internal body parts would slightly alter the dielectric properties of the Honeybee, and as a result, alter the observable backscattered cross section.

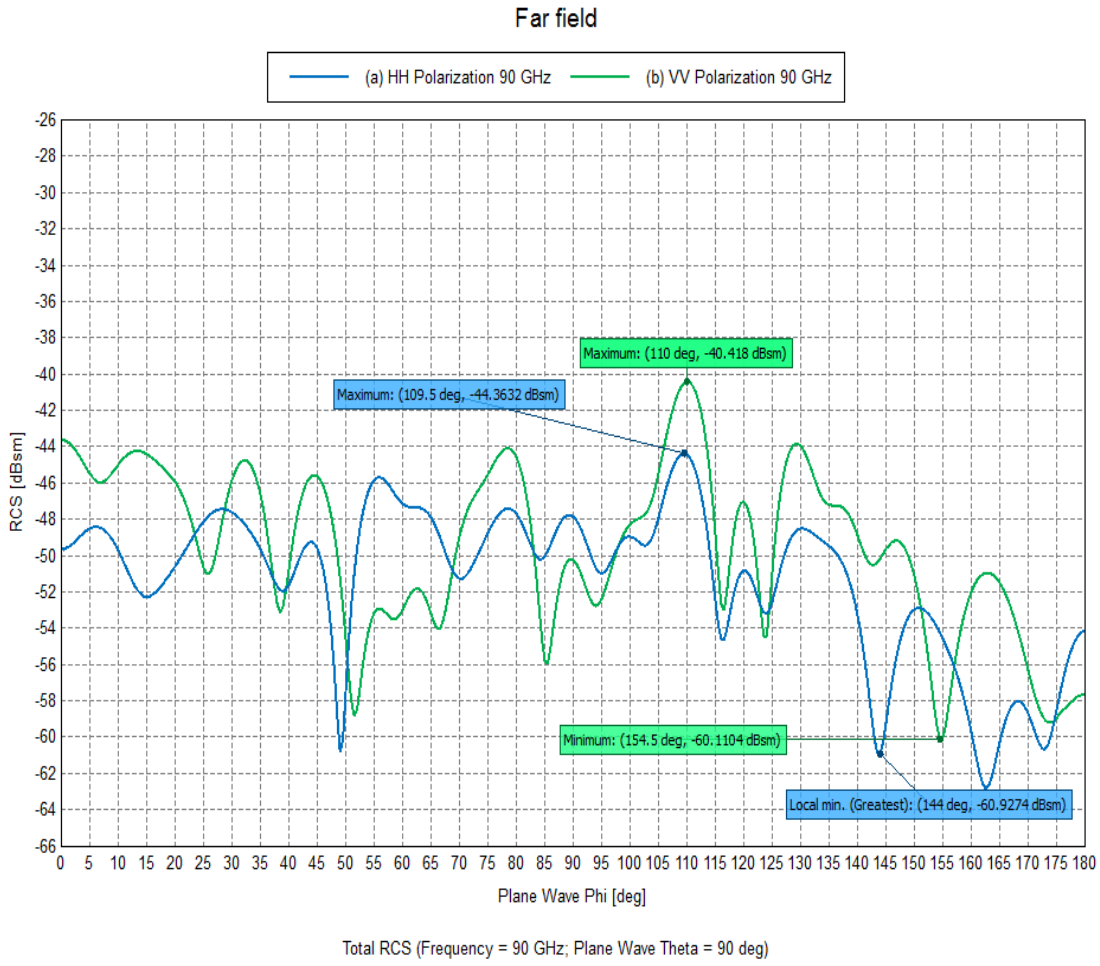

Figure 3.13: The backscattering cross sections of the Honeybee as function of incident angle at 90 GHz (W-band) (a) Horizontal Polarization (blue) (b) Vertical Polarization (green).

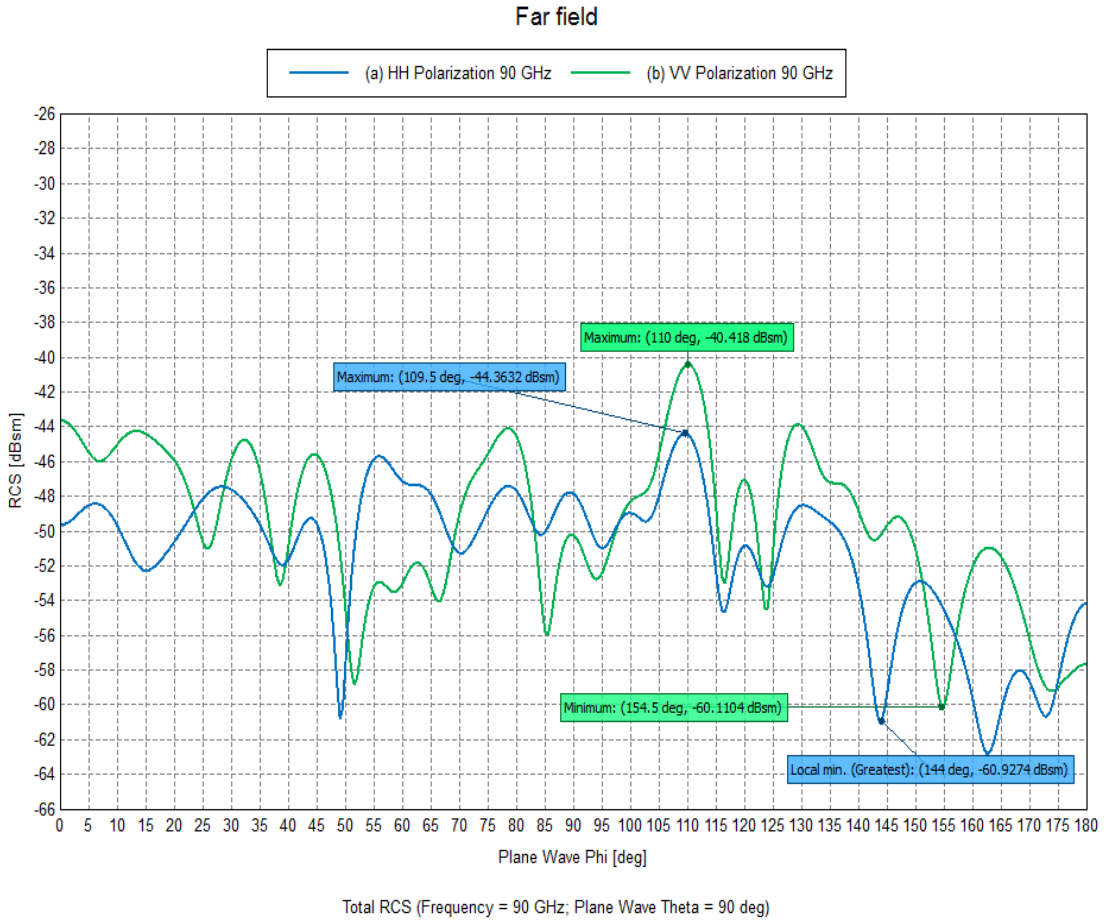

Figure 3.13: The backscattering cross sections of the Honeybee as function of incident angle at 90 GHz (W-band) (a) Horizontal Polarization (blue) (b) Vertical Polarization (green).

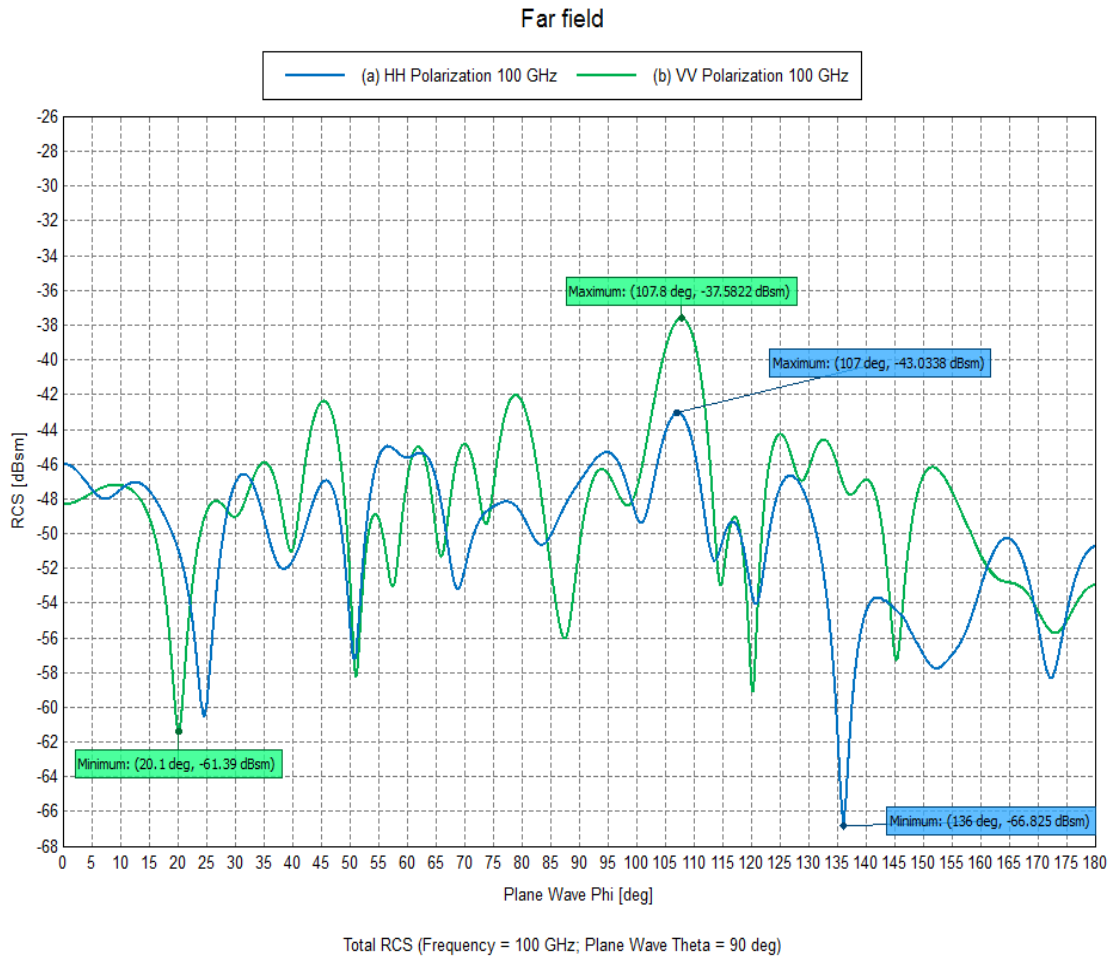

Figure 3.14: The backscattering cross sections of the Honeybee as function of incident angle at 100 GHz (W-band) (a) Horizontal Polarization (blue) (b) Vertical Polarization (green).

To investigate further the effect of the dielectric composition of Honeybee tissue on backscattering cross section magnitude and shape, Figures 3.15-3.20 compare the backscattering cross section between the dielectric and the PEC Honeybee models for horizontal polarization at multiple frequencies. Generally, the backscattering cross section magnitude of the PEC model is larger than the dielectric model; however, in this case, the difference between the PEC and the dielectric is minimal. It is observed that the difference between the backscattering cross sectional magnitudes decreases as the frequency increases. This is illustrated in Figures 3.15-3.19 respectively. The difference in shape of the backscattered cross section also remains constant in the Rayleigh region, as shown in Figures 3.15-3.16.

As the frequency increases, the difference between the latter becomes much smaller, as shown in Figures 3.17-3.19, but the shape changes as it approaches the interference scattering region. However this is only true as long as the wavelength does not approach the Honeybee's body diameter. As observed in Figure 3.20, when the wavelength approached the body diameter of the Honeybee, the difference between the latter became larger once more. One can deduce from this that the Honeybee size and operating frequency, specifically at higher frequencies, contribute significantly to the results of the backscattering cross section magnitude. The dielectric composition has almost minimal effects at higher frequencies, while effects at the lower end of the frequency of operation are more evident.

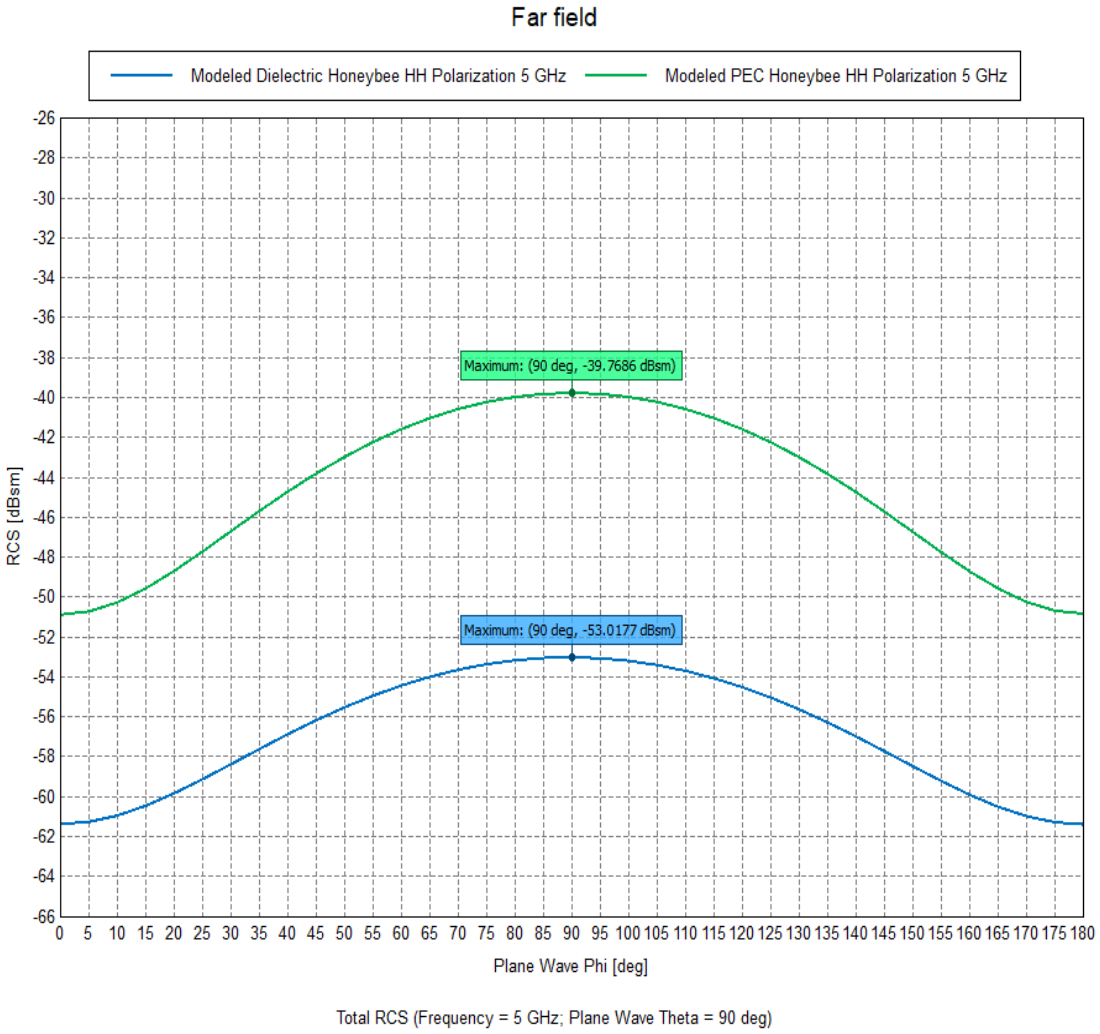

Figure 3.15: Comparison of Dielectric and PEC Honeybee modeled backscattering cross section for horizontal polarization at 5 GHz.

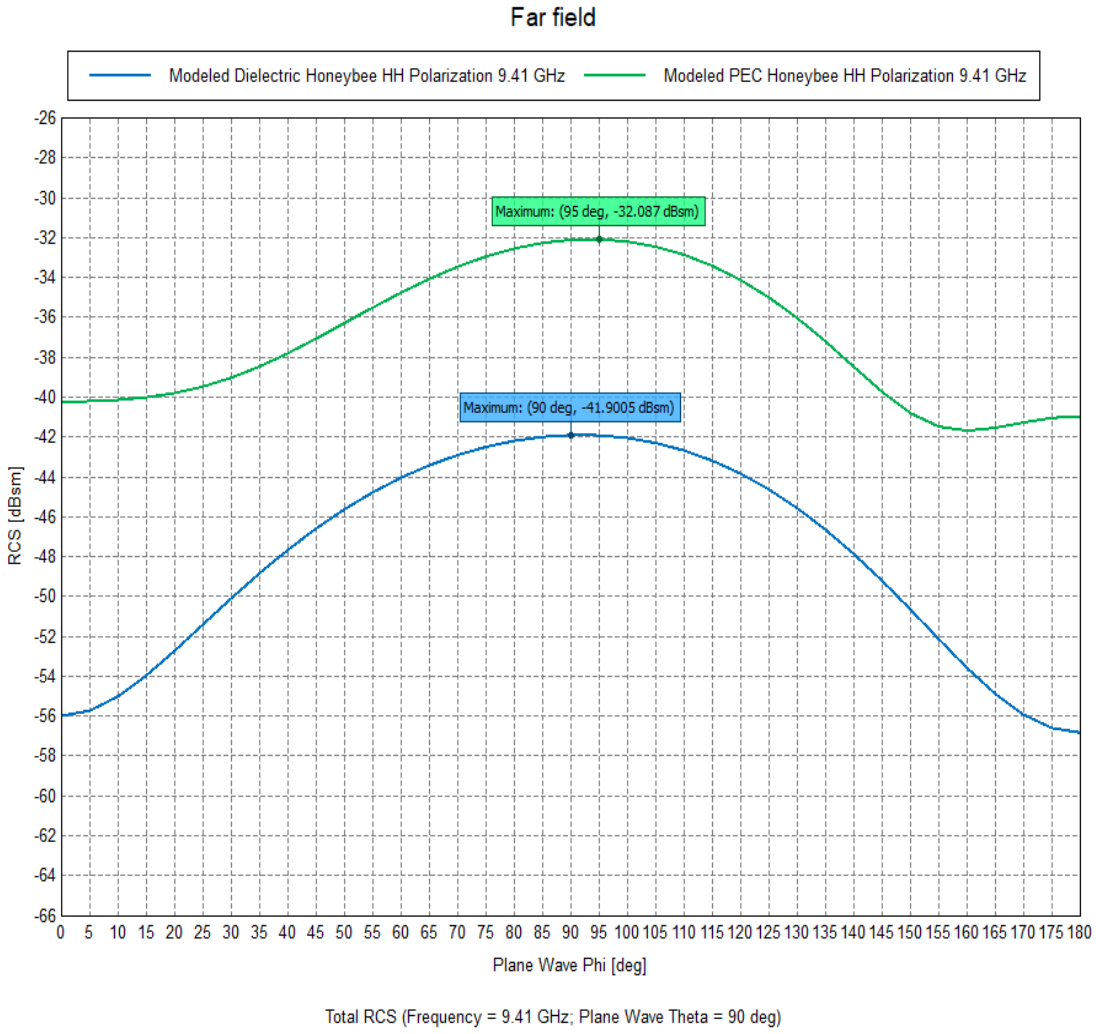

Figure 3.16: Comparison of Dielectric and PEC Honeybee modeled backscattering cross section for horizontal polarization at 9.41 GHz.

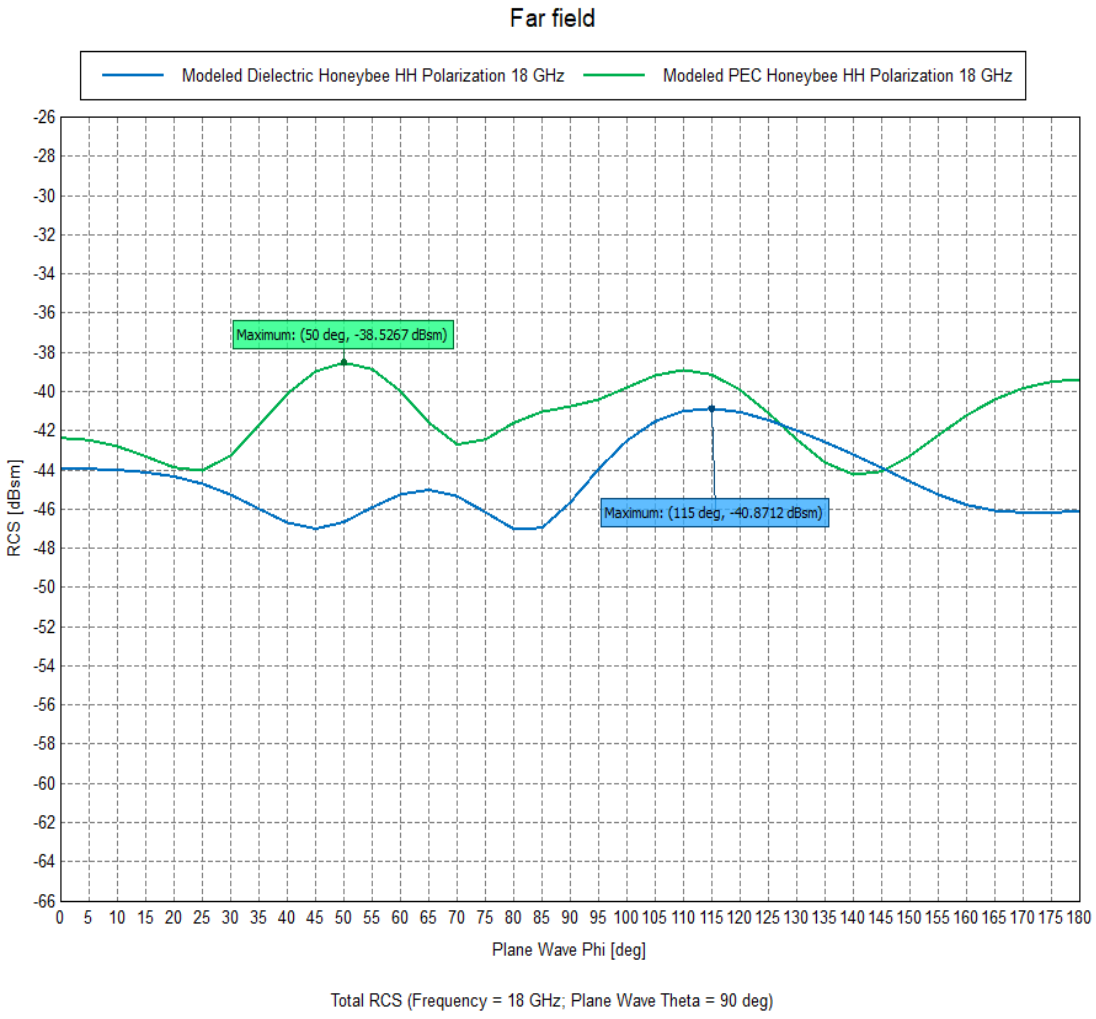

Figure 3.17: Comparison of Dielectric and PEC Honeybee modeled backscattering cross section for horizontal polarization at 18 GHz.

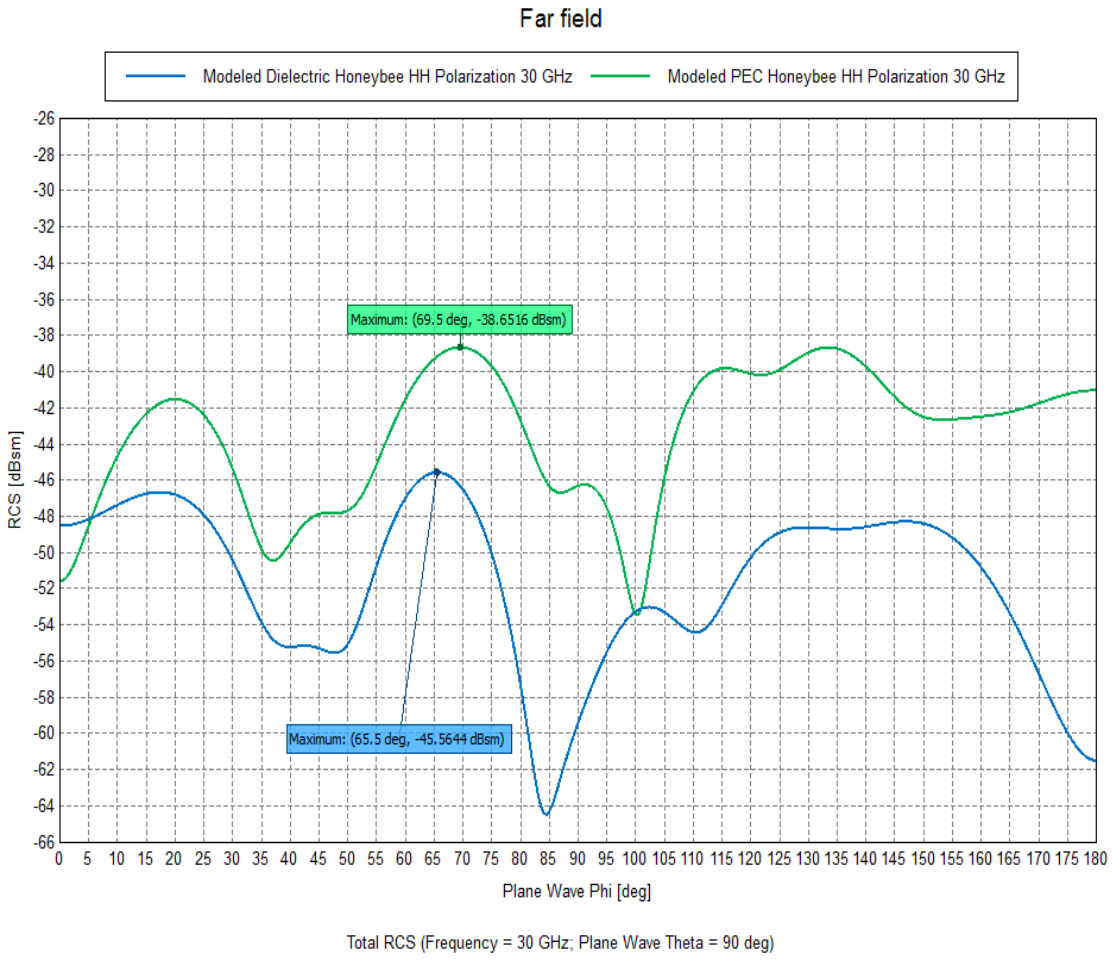

Figure 3.18: Comparison of Dielectric and PEC Honeybee modeled backscattering cross section for horizontal polarization at 30 GHz.

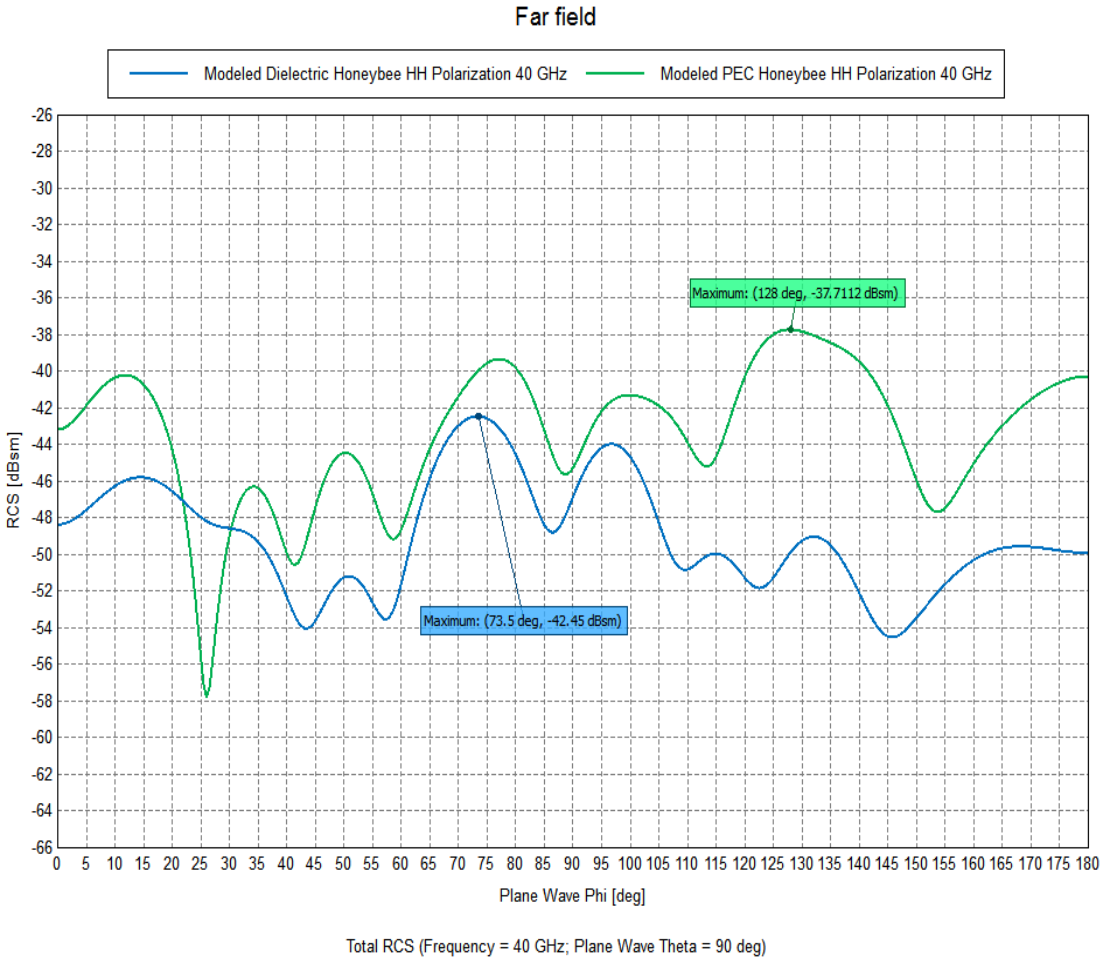

Figure 3.19: Comparison of Dielectric and PEC Honeybee modeled backscattering cross section for horizontal polarization at 40 GHz.

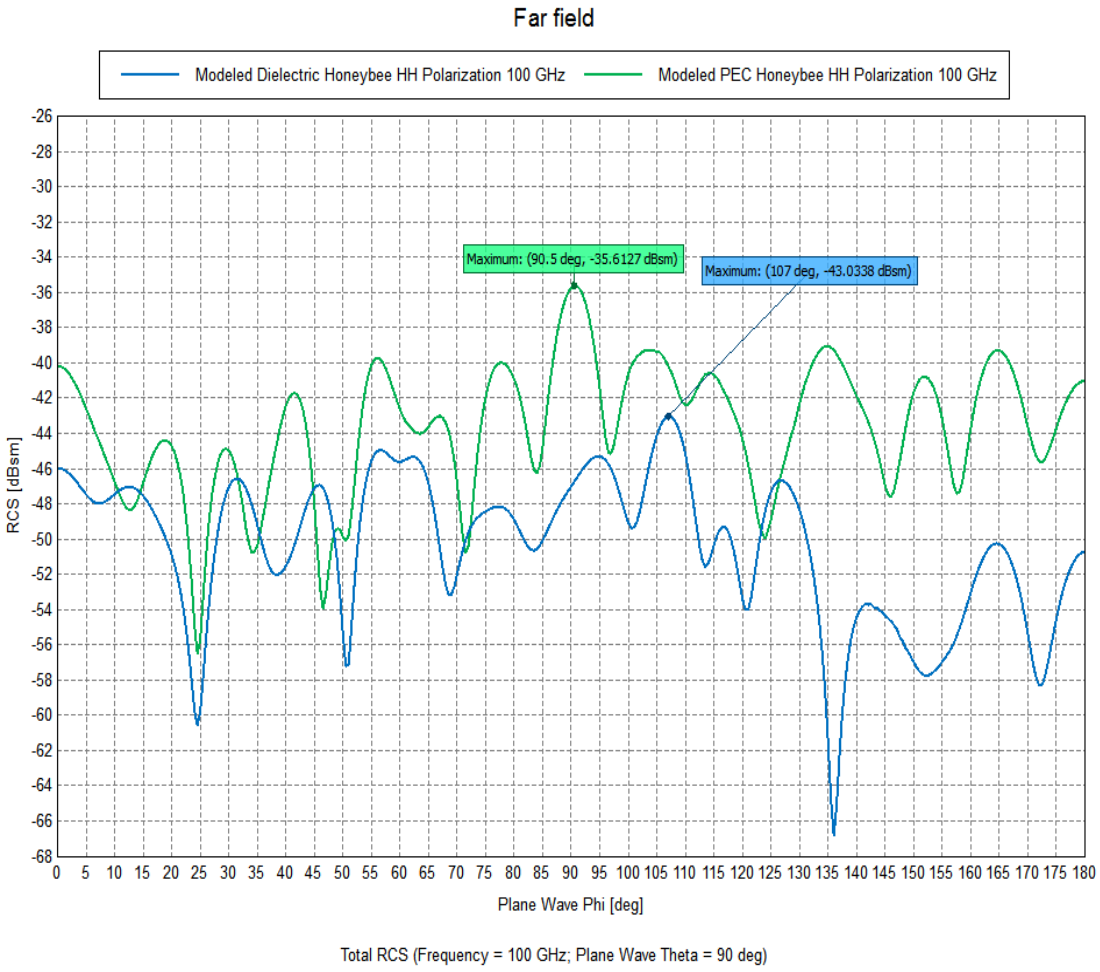

Figure 3.20: Comparison of Dielectric and PEC Honeybee modeled backscattering cross section for horizontal polarization at 100 GHz.

3.5 References

[1] Lack, David, and G. C. Varley. "Detection of birds by radar." *Nature* 156.3963 (1945): 446.

[2] Crawford, A. B. "Radar reflections in the lower atmosphere." *Proceedings of the Institute of Radio Engineers* 37.4 (1949): 404-405

[3] Edwards, J., and E. W. Houghton. "Radar echoing area polar diagrams of birds." *Nature* 184.4692 (1959): 1059.

[4] Glover, Kenneth M., et al. "Radar characteristics of known insects in free flight." (1967).

[5] Vaughn, Charles R. "Birds and insects as radar targets: a review." *Proceedings of the IEEE* 73.2 (1985): 205-227.

[6] Bruderer, Bruno. "The study of bird migration by radar part 2: Major achievements." *Naturwissenschaften* 84.2 (1997): 45-54.

[7] Horn, Jason W., and Thomas H. Kunz. "Analyzing NEXRAD doppler radar images to assess nightly dispersal patterns and population trends in Brazilian free-tailed bats (Tadarida brasiliensis)." *Integrative and Comparative Biology* 48.1 (2008): 24-39.

[8] Chapman, Jason W., V. Alistair Drake, and Don R. Reynolds. "Recent insights from radar studies of insect flight." *Annual review of entomology* 56 (2011): 337-356.

[9] Chilson, Phillip B., et al. "Partly cloudy with a chance of migration: weather, radars, and aeroecology." *Bulletin of the American Meteorological Society* 93.5 (2012): 669-686.

[10] Drake, V. A. "Estimation of unbiased insect densities and density profiles with vertically pointing entomological radars." *International journal of remote sensing* 35.13 (2014): 4630-4654.

[11] Drake, V. A. "Target density estimation in radar biology." *Journal of Theoretical Biology* 90.4 (1981): 545-571.

[12] Skolnik, Merrill Ivan. "Radar handbook." (1970).

[13] Knott, Eugene F. *Radar cross section measurements*. Springer Science & Business Media, 2012.

[14] Hobbs, S. E., and Anthony C. Aldhous. "Insect ventral radar cross-section polarisation dependence measurements for radar entomology." *IEE Proceedings-Radar, Sonar and Navigation* 153.6 (2006): 502-508.

[15] Hajovsky, R., A. Deam, and A. LaGrone. "Radar reflections from insects in the lower atmosphere." *IEEE Transactions on Antennas and Propagation* 14.2 (1966): 224-227.

[16] Bruderer, Bruno. *Zur Registrierung und Interpretation von Echosignaturen an einem 3-cm-Zielverfolgungsradar*. 1969.

[17] Riley, Joseph R. "Radar cross section of insects." *Proceedings of the IEEE* 73.2 (1985): 228-232.

[18] Wolf, W. W., et al. "Insect radar cross-sections for aerial density measurements and target classification." *Transactions of the ASAE* 36.3 (1993): 949-954.

[19] Riley, J. R. "Angular and temporal variations in the radar cross-sections of insects." *Proceedings of the Institution of Electrical Engineers*. Vol. 120. No. 10. IET, 1973.

[20] Mm, G. "A Contribution in the Optics of Turbid Media, Especially Colloidal Metallic Suspensions." *Ann. Phys* 25 (1908): 377-445.

[21] Schaeffer, G. W. "Bird recognition by radar: A study in quantitative radar ornithology." *The problems of Birds as Pests*(1968): 53-56.

[22] Melnikov, Valery M., Michael J. Istok, and John K. Westbrook. "Asymmetric radar echo patterns from insects." *Journal of Atmospheric and Oceanic Technology* 32.4 (2015): 659-674.

[23] Mirkovic, Djordje, et al. "Electromagnetic model reliably predicts radar scattering characteristics of airborne organisms." *Scientific reports* 6 (2016): 35637.

[24] Harrington, Roger F. "The method of moments in electromagnetics." *Journal of Electromagnetic waves and Applications* 1.3 (1987): 181-200.

[25] Balanis, Constantine A. *Advanced engineering electromagnetics*. John Wiley & Sons, 1999

[26] Ton, Cuong. *Radar cross section (RCS) simulation for wind turbines*. NAVAL POSTGRADUATE SCHOOL MONTEREY CA, 2013.

[27] Kunz, Karl S., and Raymond J. Luebbers. *The finite difference time domain method for electromagnetics*. CRC press, 1993.

[28] Sevgi, L., and S. Paker. "FDTD based RCS calculations and antenna simulations." *AEU. Archiv für Elektronik und Übertragungstechnik* 52.2 (1998): 65-75.

[29] Jin, Jian-Ming. *The finite element method in electromagnetics*. John Wiley & Sons, 2015.

[30] Volakis, John L., Arindam Chatterjee, and Leo C. Kempel. *Finite element method electromagnetics: antennas, microwave circuits, and scattering applications*. Vol. 6. John Wiley & Sons, 1998.

[31] Aldhous, Anthony C. "An investigation of the polarisation dependence of insect radar cross sections at constant aspect." (1989).

[32] FEKO web page [online]. Available: https://altairhyperworks.com/product/FEKO

[33] Stratton, Julius Adams. "Electromagnetic theory. International series in pure and applied physics." (1941).

[34] Kerr, Donald E. "Propagation of Short Radio Waves (Volume 13 in the Massachusetts Institute of Technology Radiation Laboratory series)." (1965).

[35] Blake, Lamont V. "Radar range-performance analysis." *Norwood, MA, Artech House, Inc., 1986, 467 p.* (1986).

[36] https://www.solidworks.com/

[37] Kuang, Wensheng, and S. O. Nelson. "Low-frequency dielectric properties of biological tissues: a review with some new insights." *Transactions of the ASAE-American Society of Agricultural Engineers* 41.1 (1998): 173-184.

[38] Gabriel, Sami, R. W. Lau, and Camelia Gabriel. "The dielectric properties of biological tissues: II. Measurements in the frequency range 10 Hz to 20 GHz." *Physics in medicine & biology* 41.11 (1996): 2251.

Chapter 4

Radar Cross Section Measurement of Honeybee Apis Mellifera

4.1 Introduction

The purpose of this chapter is to validate the backscattering cross section results of the Honeybee model obtained through the FEKO method of moments. Several challenges complicated the backscattering cross section measurements of the Honeybee. Mainly, Honeybee size and dielectric composition produced weak echo signals that were masked by the surrounding clutter and interference. In addition, the delicacy and fragility of the Honeybee body caused a challenge in handling and maintaining a consistent position when performing the measurements. The following sections describe the method of measurement and apparatus used in determining the backscattering RCS characteristics of the Honeybee.

4.2 Samples Collection Procedure

The Honeybee worker (i.e., Apis Mellifera) samples were collected in accordance with relevant guidelines of the Department of Entomology at The Ohio State University. They were collected from Rothernbuhler Honeybee Research Laboratory during the Winter 2018 season. The winter Honeybees inside the colony live longer than summer Honeybees. They are not very active and stay inside the beehive in winter, which made collecting the Honeybees easier. In essence, they are in a state of low metabolism, to prepare for the population growth needed the following spring. The extreme freezing temperature during winter months was a problem, since the beehive had to be opened. As Honeybees are cold-blooded, the hive must maintain a warm temperature to keep the colony alive and unharmed. Therefore, to avoid this issue, the beehive lid was quickly raised

and Honeybee samples were grabbed without disturbing them too much, placing them in a glass vial. Protective gear including a veil and gloves were used and made the collection of the Honeybee samples safer and easier. Only one sample of the collected Honeybees was selected for RCS measurement. The RCS measurements were performed mostly within 2-3 hours of collection, to match the RCS signatures of the living Honeybee.

4.3 Description of the Compact Range Facility and Measuring Apparatus

The backscattering cross section measurements of the Honeybee were performed in the anechoic chamber at the ElectroScience Laboratory (ESL) at The Ohio State University (OSU). A photograph of the compact range facility is shown in Figure 4.1. It is one of the largest academic chambers of size $60 \times 40 \times 20$ ft and the finest compact range in the world that operates from 400 MHz to 100 GHz band. It has a sensitivity down to -100 dBm. The chamber is covered with high-quality radar-absorbing material, and employs both wedge and pyramidal-shaped absorber on the walls, floor, ceiling, and support structure for the reflector and feed. This system utilizes the 16 ft high by 16 ft wide compact rolled-edge parabolic reflector to generate a far-field plane wave in the confines of anechoic chamber; it allows a much smaller antenna-target distances. The feed antennas are located at the focal point of the reflector and either horizontal or vertical displacement can be used. The reflector is rolled-edge, reducing edge diffraction and shadowing from the feed and feed support. The target support structure is a foam column and is supported with an internal mechanism for azimuth rotation. This set of feed antennas and the velocity of support rotation are controlled by a computer program software.

Figure 4.1: Photograph of compact radar range at ElectroScience Laboratory at The Ohio State University.

A block diagram of the measuring apparatus used in determining the backscattering cross sections of Honeybee is presented in Figure 4.2. The vector network analyzer (VNA) used in this analysis was the Agilent E8362B. This VNA is equipped with a single source and has a frequency range of 10 MHz to 20 GHz. One limitation in using this VNA is that it has a limited power output. Consequently, the backscatter from the target will drop below the noise floor. To overcome this limitation, a source port of the VNA system was connected to the power amplifier AMF-3D-020180-60-20P. The transmitting and receiving ports of the antennas were connected to the source port of the power amplifier and receiver port of the VNA, respectively. The antennas that were used are ultra-broadband frequency performance (2.0-18.0 GHz), Cobham horns (model H-1498). They were set up in a quasi-monostatic configuration, where the transmit and receive antennas are

slightly separated, but still appear to be at the same location as viewed from the target, and RCS measurements are taken through S_{21}. Their placement was such that their combined phase center is at the focus of the reflector. The system is interfaced with computer software, to control the measurement process and to record the digested data.

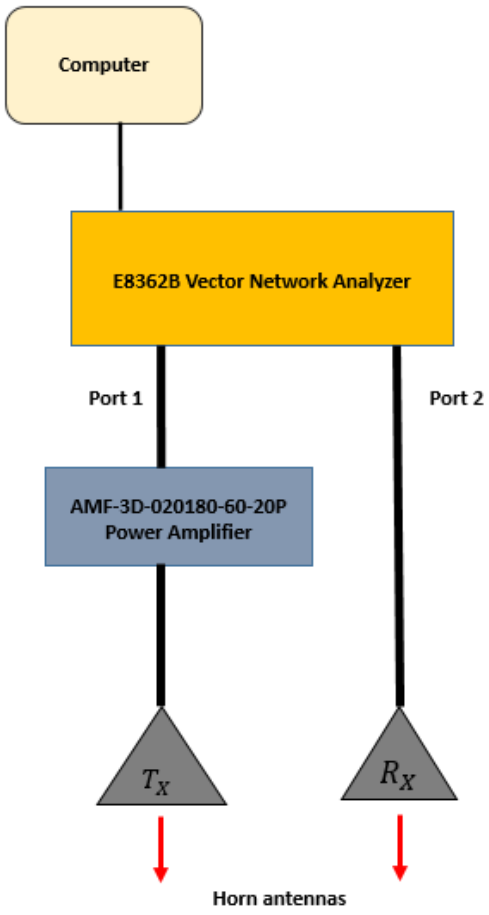

Figure 4.2: Block diagram of the backscattering cross section measurement system at the ESL-OSU anechoic chamber.

4.4 Procedure

There were several challenges encountered prior to RCS measurements. The Honeybee is a very aggressive insect when it feels threatened, and its body structure is extremely delicate and small in size. This made the RCS measurements more complicated and challenging to perform. The most challenging task was stabilizing the Honeybee body in exact and consistent positioning during measurements. This problem was solved to some degree by anaesthetizing the Honeybee. The anesthetic apparatus consisted of a conical tube and dry ice. The Honeybee was placed inside the conical tube and the emission of carbon dioxide from the dry ice was injected for about 1-2 minutes. The carbon dioxide did not kill the Honeybee but did immobilize its body movements enough to the point that it could be easily fixed to a desired position prior to performing the measurement. Additionally, the dielectric composition and the Honeybee model in FEKO software yielded relatively weak backscattering cross sections, which are easily contaminated by surrounding clutter or interactions in the test environment. Such a prediction of weak backscattering signals made using the supporting structure for suspending the Honeybee more difficult. To eliminate this problem, foam supporters chosen to have minimal electromagnetic contribution to recorded measurements were used. Nonetheless, attempts were made at further minimizing effects of foam supporters together with the background through noise cancellation and background signature (clutter) subtraction. The Honeybee's thorax was glued to the center of a styrofoam cup, as shown in Figure 4.3. The styrofoam cup with the glued Honeybee was then mounted on the top of the foam column. The foam column on the positioner provided rotations to a desired increment in azimuth angle.

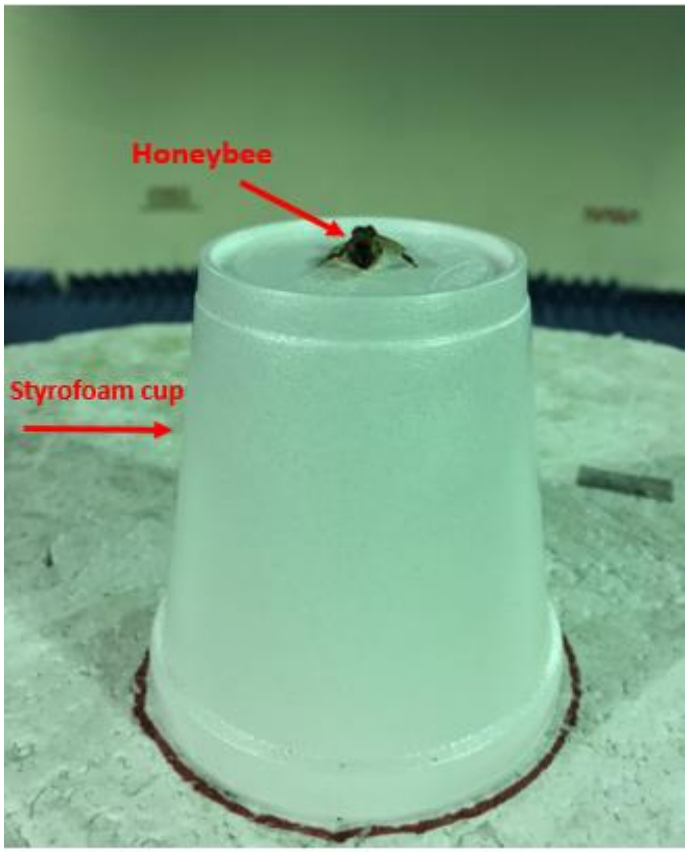

Figure 4.3: Physical setup of Honeybee sample on Styrofoam cup (with contributions of cup calibrated out of measurements).

Even though the foam supports have low reflection, they can still interfere by masking small features of the target. Similarly, the small reflection from the chamber can interfere with the desired target echo signal. To mitigate this interference, the technique is to take two measurements with the VNA, one with the target under investigation (the Honeybee in this case) and one with the absence of the target being investigated, which is considered the background. Then, the background data magnitude and phase is subtracted from the target plus background data, to suppress unwanted reflections from the test environment. To further improve RCS measurement quality, signal post-

processing using time gating was implemented to suppress multipath reflections, especially those interactions between the target and the test environment which are not present in the background data but have distinguishable path length differences. The frequency sweep data is processed with an inverse fast-Fourier transformation algorithm, and then a window is created around the target reflection at specified time points with a specified rejection for outlying signals. The time-gated data is then transformed back into frequency domain with a fast-Fourier transformation.

There are several ways to calibrate RCS measurement; however, they all require measurements of or calculations for objects that have well-understood RCS characteristics, such as spheres, cylinders, or plates composed of conducting material. Spheres are typically used as a standard for experimentally calibrating radar systems, because of its pure radial symmetry and the invariance of its echo with orientation. Here, two conductive spheres with a diameter of 2.75 and 12 in. were calibrated to each other for comparison. For calibration standards verification, the RCS of both spheres were measured and compared to the Mie series theoretical (exact) solution. The two spheres were measured from 2 GHz to 18 GHz. The maximum error was about 2 dB, but it was found to be more accurate for the 12 inch-diameter sphere (see Appendix A). Therefore, the 12 inch-diameter sphere was used to calibrate the system. The calibration spheres were positioned on top of a styrofoam cup, identical to what the Honeybee was placed on.

4.5 Results and Discussion

To validate the calculation of backscattering cross section results of the Honeybee model obtained through the FEKO method of moments, a comparison between the model results and the measurements was made. The backscattering cross section measurements of the Honeybee were carried out for both horizontal and vertical polarizations over the frequency range between 2 and 18 GHz with a frequency step of 6 MHz. The measurements were performed at the incident angle of the plane wave $\theta = 90^{\circ}$ and $0^{\circ} \leq \varphi \leq 360^{\circ}$. The azimuth angle was incremented by 5 degrees. Figures 4.4-4.36 compare the backscattering cross section results between the measured and modeled Honeybees. They are represented in rectangular diagrams, and expressed in dBsm. The Honeybee's head (Head-on) and abdomen (End-on) correspond to azimuth angles of $0^{\circ}/360^{\circ}$ and 180°, respectively.

In general, the minimum measured and modeled backscattering cross sections occur with head-on and end-on positions of the Honeybee, whereas the maximum backscattering cross sections occur between 0° and 180° or 180° and 360° in the azimuth plane, that is, when the Honeybee is broadside-on to the incident wave for horizontal and vertical polarizations. Some disparities did occur in both shape and magnitude of backscattering cross section results between the measured and modeled Honeybee, in both horizontal and vertical polarization cases.

Measured and modeled backscattering cross sections of the Honeybee corresponding to horizontal polarization are shown in Figures 4.4-4.16. The overall backscattering cross section magnitudes between the measured and modeled Honeybee are generally similar. There were slight differences in backscattering cross section magnitudes between the measured and modeled Honeybee at some azimuth angles. This is due to some "clutter" (undesired reflections) that could not be completely removed from the test signal during the calibration process. This clutter could

be associated with some retained residual reflections in the anechoic chamber, or the mutual coupling between two horn antennas.

In most cases, the measured backscattering cross sections shapes are approximately symmetrical; however, the curves are offset in the azimuth angle. These shifts in azimuth angle can be attributed to physical misalignments between the measured and modeled Honeybee. It was difficult to suspend the body of the measured Honeybee in an exact position like the modeled one, since the Honeybee's body is extremely delicate and small in size. The Honeybee had to be suspended by gluing the underneath of the thorax surface to the center of styrofoam cup, which makes this part not visible as in the case of the modeled Honeybee.

Most likely, another possible interpretation of the offset in azimuth angle is to maintain the Honeybee's body position during the measurement. The time requirement of the measurement is about 25-30 minutes; however, the carbon dioxide gas can only keep the glued Honeybee anesthetized and stable at the center of styrofoam cup for the first 3-5 minutes of the measurement. After that, the Honeybee starts to move its body parts, such as head, legs, wings, and abdomen, slowly during the remaining time of the measurement. Such slow body movements could cause variations in the aspect angle, which consequently are observed in both backscattering cross sections shape and magnitude, since the RCS values are strongly dependent on the shape and orientation of the scatterer with respect to the radar position. These effects are more noticeable at higher frequencies, as shown in Figures 4.12-4.16. The shapes and magnitudes of the measured and modeled backscattering cross sections are not quite identical. In addition to the previous effects, it is expected at higher frequencies that the foam column has higher RCS, and consequently it affects the accuracy of backscattering cross section measurements of the Honeybee.

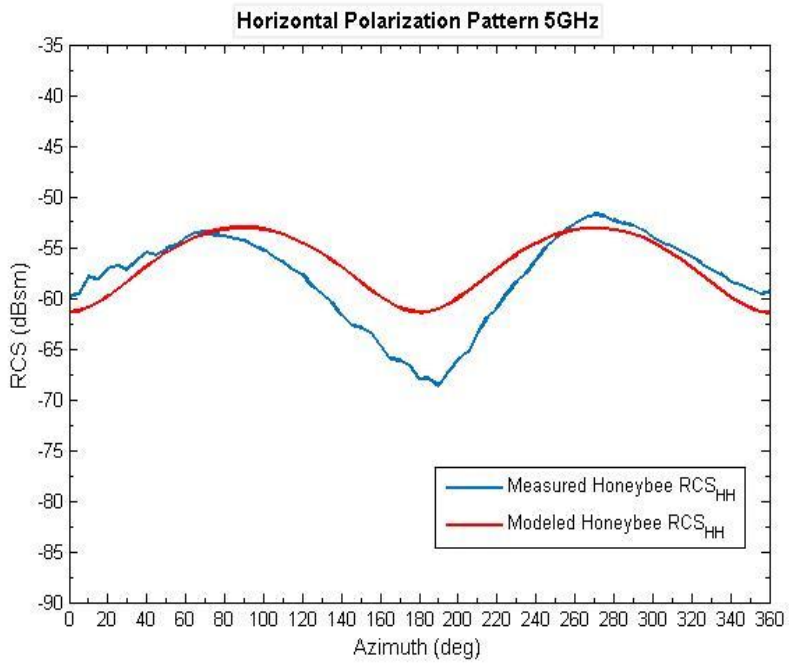

Figure 4.4: Comparison of measured and modeled backscattering cross section of a Honeybee worker (i.e., Apis Mellifera) for horizontal polarization at 5 GHz.

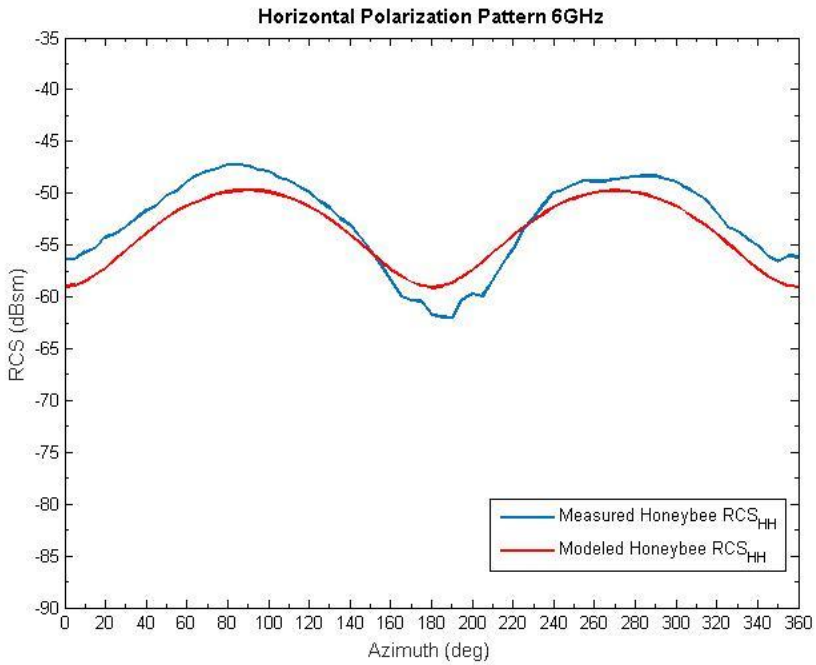

Figure 4.5: Comparison of measured and modeled backscattering cross section of a Honeybee worker (i.e., Apis Mellifera) for horizontal polarization at 6 GHz.

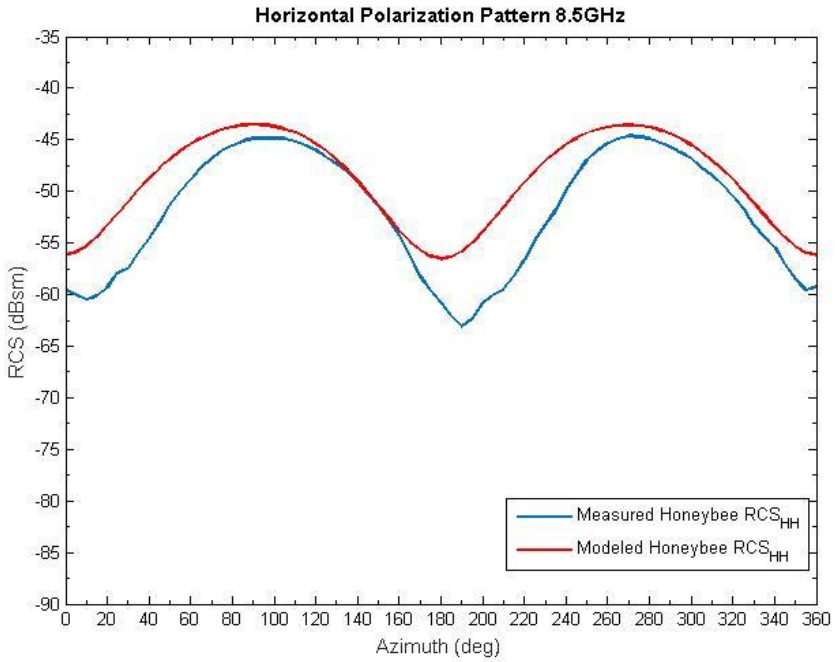

Figure 4.6: Comparison of measured and modeled backscattering cross section of a Honeybee worker (i.e., Apis Mellifera) for horizontal polarization at 8.5 GHz.

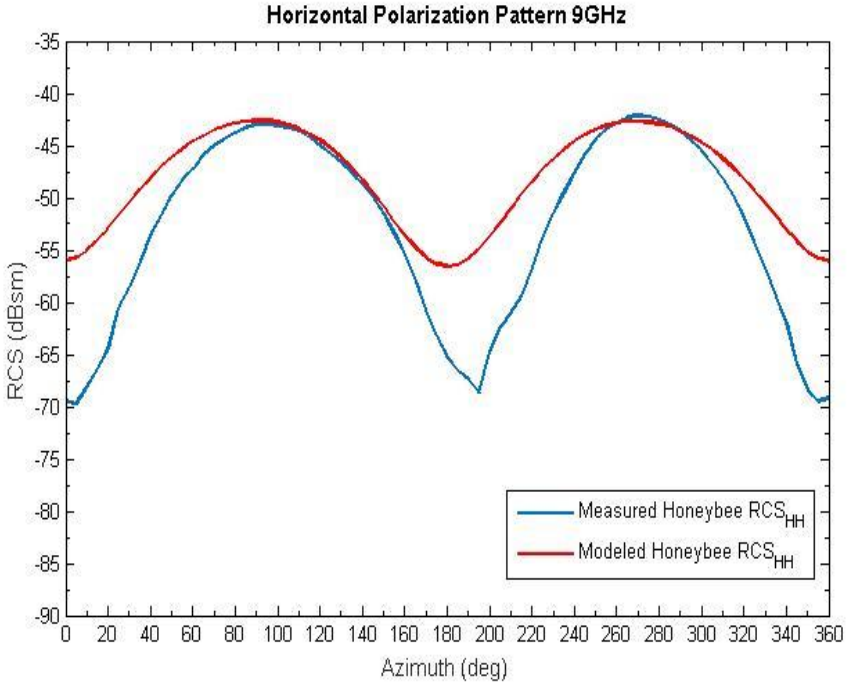

Figure 4.7: Comparison of measured and modeled backscattering cross section of a Honeybee worker (i.e., Apis Mellifera) for horizontal polarization at 9 GHz.

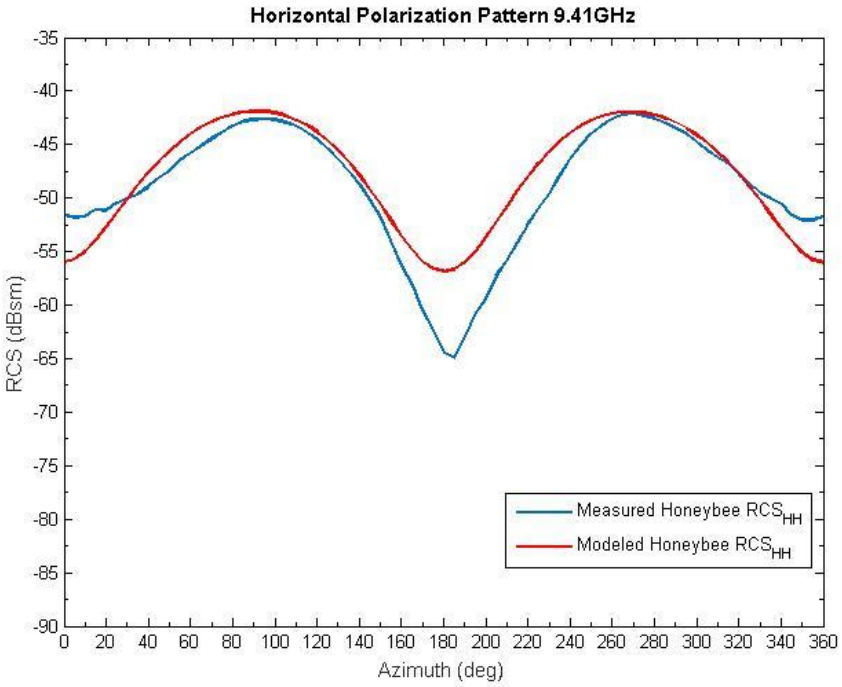

Figure 4.8: Comparison of measured and modeled backscattering cross section of a Honeybee worker (i.e., Apis Mellifera) for horizontal polarization at 9.41 GHz.

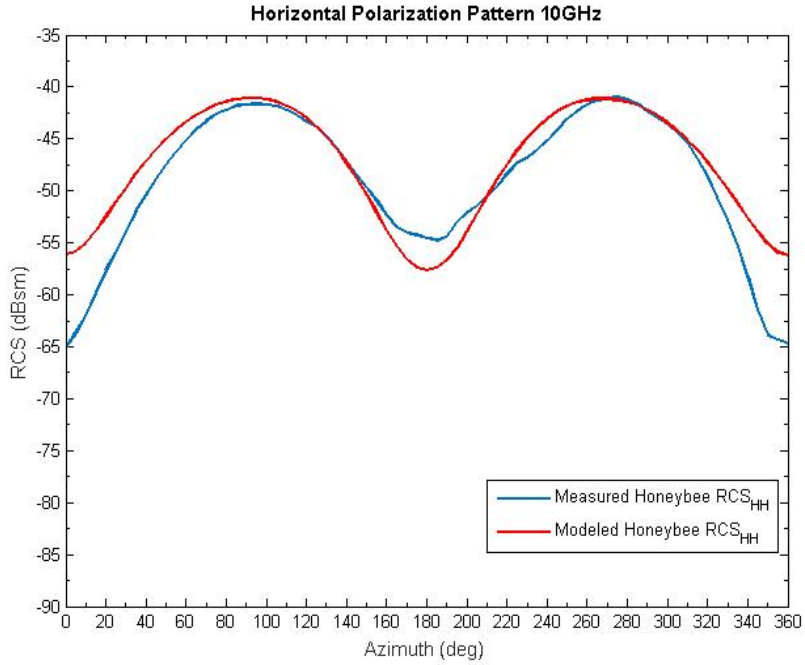

Figure 4.9: Comparison of measured and modeled backscattering cross section of a Honeybee worker (i.e., Apis Mellifera) for horizontal polarization at 10 GHz.

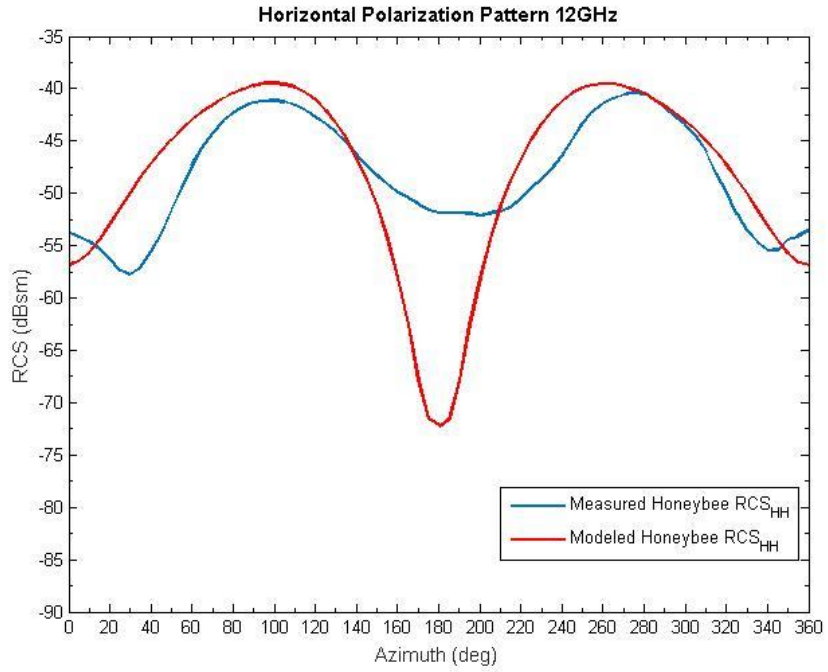

Figure 4.10: parison of measured and modeled backscattering cross section of a Honeybee worker (i.e., Apis Mellifera) for horizontal polarization at 12 GHz.

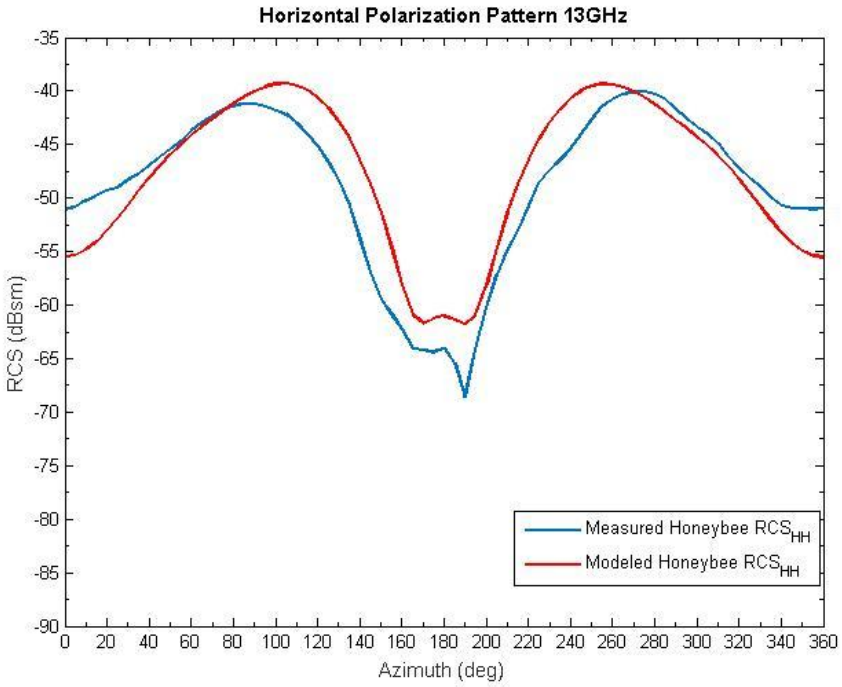

Figure 4.11: Comparison of measured and modeled backscattering cross section of a Honeybee worker (i.e., Apis Mellifera) for horizontal polarization at 13 GHz.

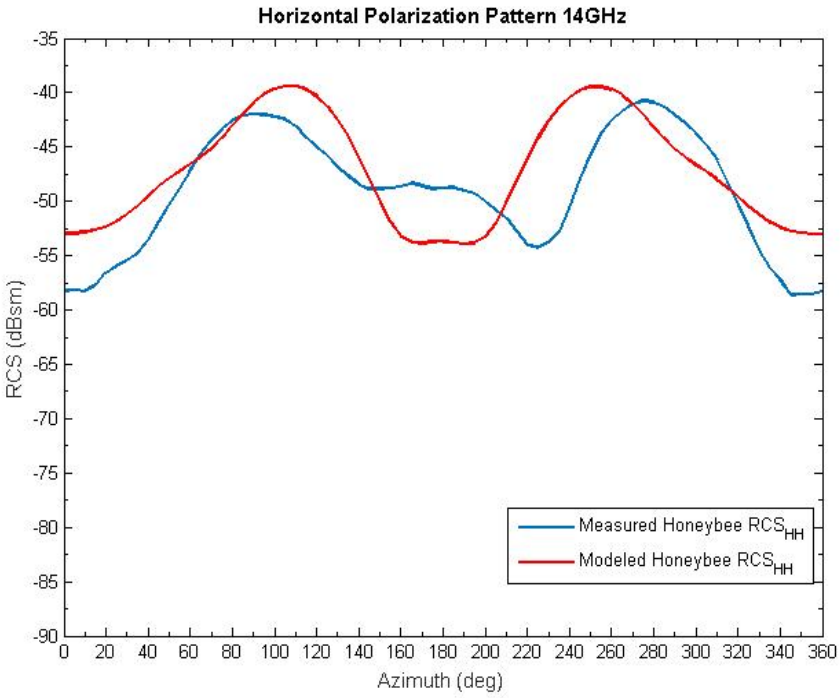

Figure 4.12: Comparison of measured and modeled backscattering cross section of a Honeybee worker (i.e., Apis Mellifera) for horizontal polarization at 14 GHz.

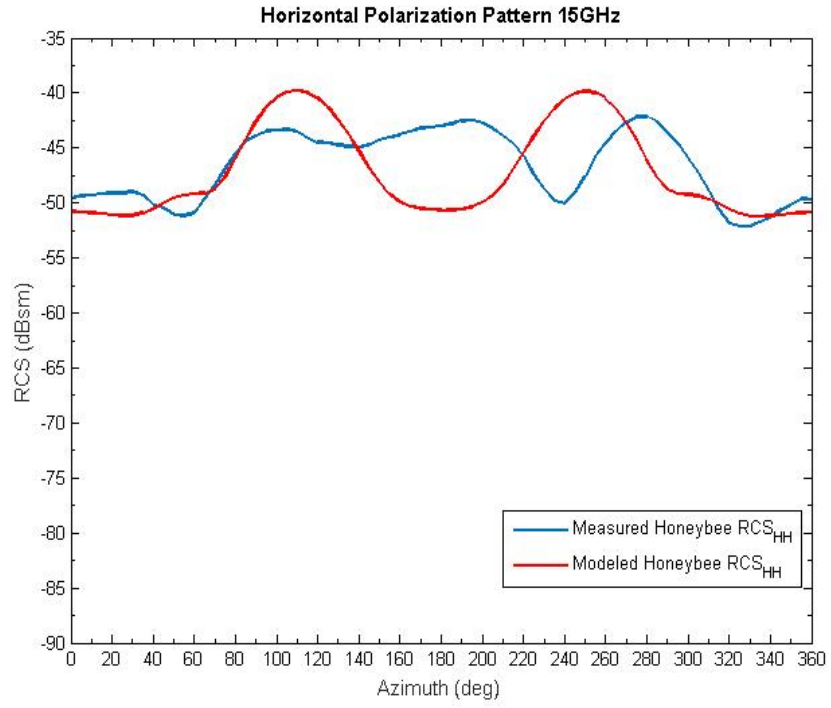

Figure 4.13: Comparison of measured and modeled backscattering cross section of a Honeybee worker (i.e., Apis Mellifera) for horizontal polarization at 15 GHz.

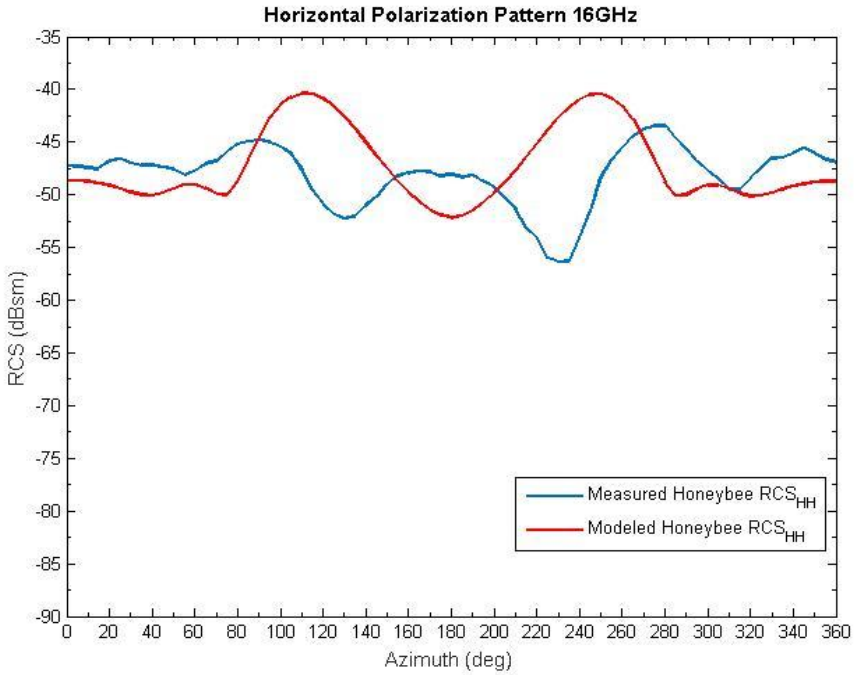

Figure 4.14: Comparison of measured and modeled backscattering cross section of a Honeybee worker (i.e., Apis Mellifera) for horizontal polarization at 16 GHz.

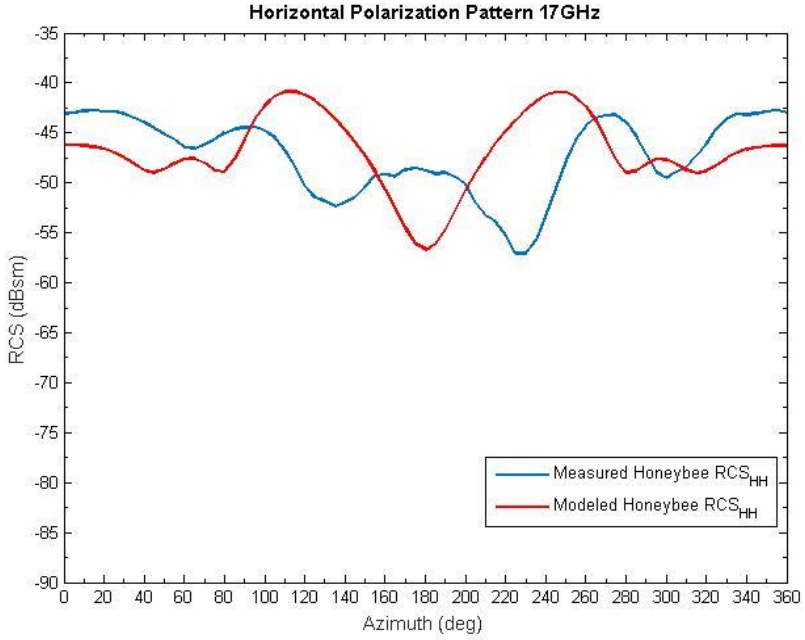

Figure 4.15: Comparison of measured and modeled backscattering cross section of a Honeybee worker (i.e., Apis Mellifera) for horizontal polarization at 17 GHz.

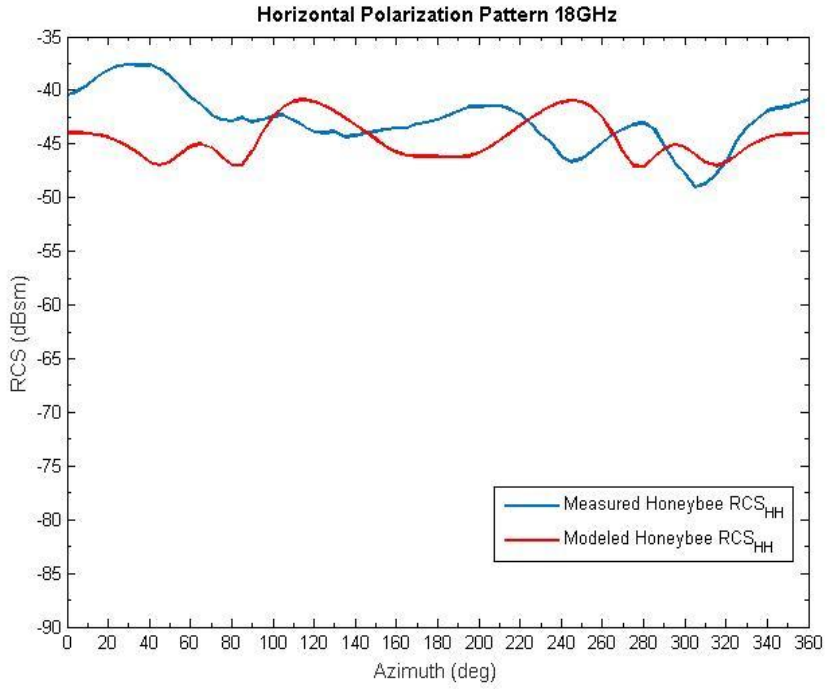

Figure 4.16: Comparison of measured and modeled backscattering cross section of a Honeybee worker (i.e., Apis Mellifera) for horizontal polarization at 18 GHz.

In contrast to the horizontal polarization, the shape and magnitude of backscattering cross section results between the measured and modeled Honeybee did not agree quite as well in the case of vertical polarization, as shown in Figures 4.17-4.28. The measured backscattering cross section shapes in most cases are not symmetrical like the corresponding horizontal ones. Such asymmetrical shapes can be due to other interactions that are not qualitatively subtracted well between the Honeybee and the test environment. For vertical polarization, the electromagnetic waves are expected to be more interactive with the whole length of the foam column, floor and ceiling of the anechoic chamber, while the interactions for horizontal polarization are mainly with the anechoic chamber side-walls, and partially with the foam column. The side-walls of the anechoic chamber are symmetrical, since they are only covered with identical pyramidal-shaped absorber materials, resulting in approximately symmetrical backscattering cross section shapes for horizontal polarization case. However, the ceiling and floor of the anechoic chamber are not symmetrical, since the ceiling is covered with 12" absorbing material, whereas the floor is covered with 18" absorber. This may explain the asymmetrical backscattering cross section shapes in the vertical polarization case.

The disparity in backscattering cross section magnitudes between the measured and modeled Honeybee for vertical polarization can be attributed to unwanted reflections associated with the foam column and styrofoam cup including the background. Prior to the subtraction process, the backscattering cross section of column, styrofoam cup, and background for vertical polarization is found to be relatively higher than that expected with the modeled Honeybee – more than for horizontal polarization (see Appendix section B.1). Moreover, it is imperative to note that the Honeybee is only realistically visible for frequencies at or higher than 5 GHz when measuring the horizontal RCS, while the vertical is only visible at 7 GHz or higher. When tested below those frequencies, background noise level is very high, which was too obstructive and interfered with the Honeybee RCS results (see Appendix section B.2).

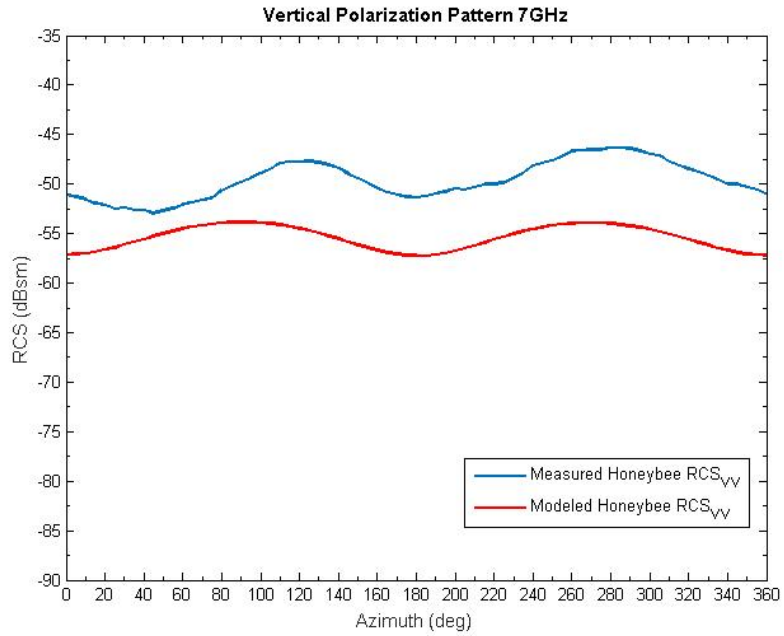

Figure 4.17: Comparison of measured and modeled backscattering cross section of a Honeybee worker (i.e., Apis Mellifera) for vertical polarization at 7 GHz.

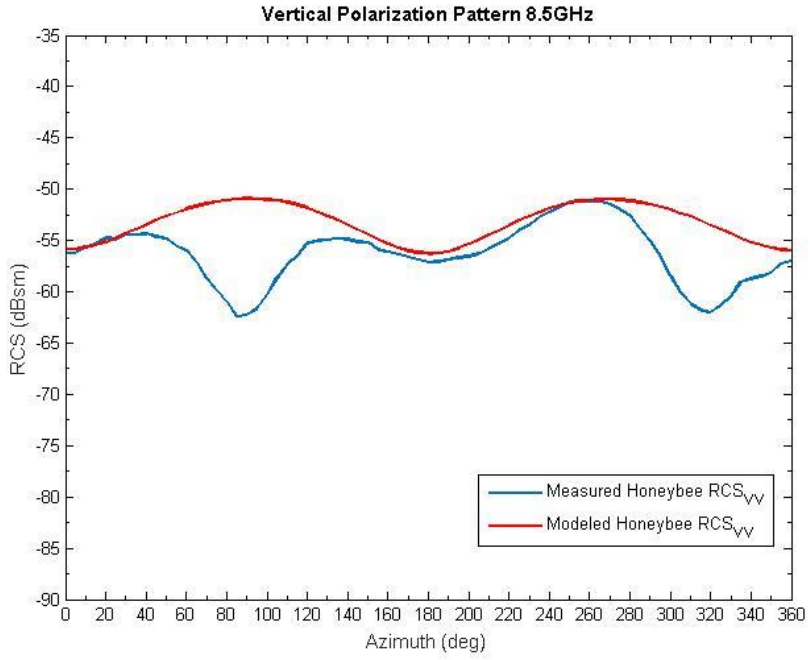

Figure 4.18: Comparison of measured and modeled backscattering cross section of a Honeybee worker (i.e., Apis Mellifera) for vertical polarization at 8.5 GHz.

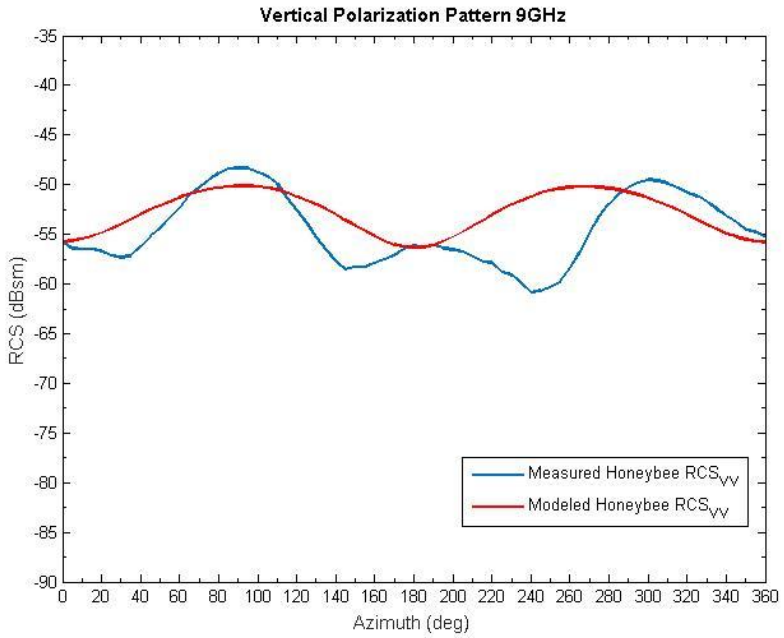

Figure 4.19: Comparison of measured and modeled backscattering cross section of a Honeybee worker (i.e., Apis Mellifera) for vertical polarization at 9 GHz.

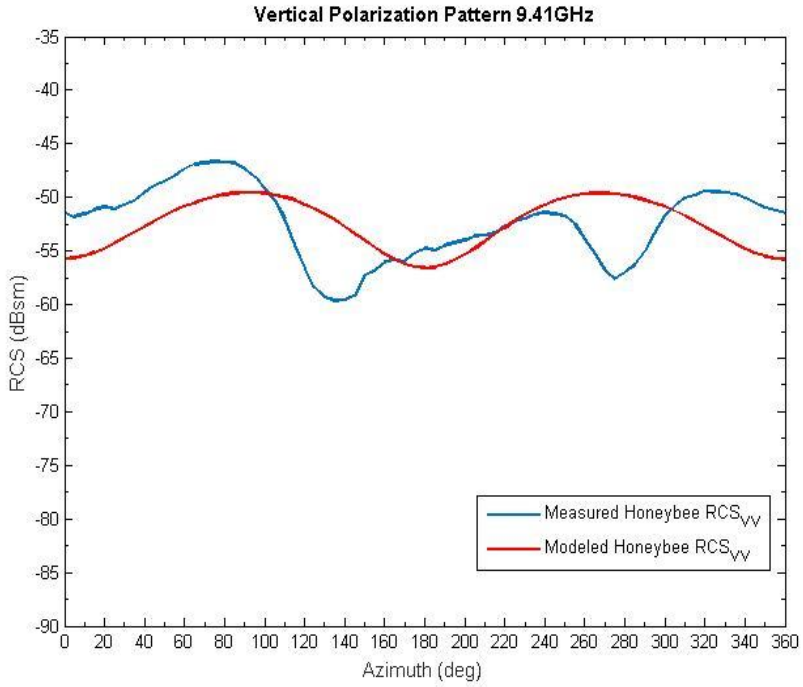

Figure 4.20: Comparison of measured and modeled backscattering cross section of a Honeybee worker (i.e., Apis Mellifera) for vertical polarization at 9.41 GHz.

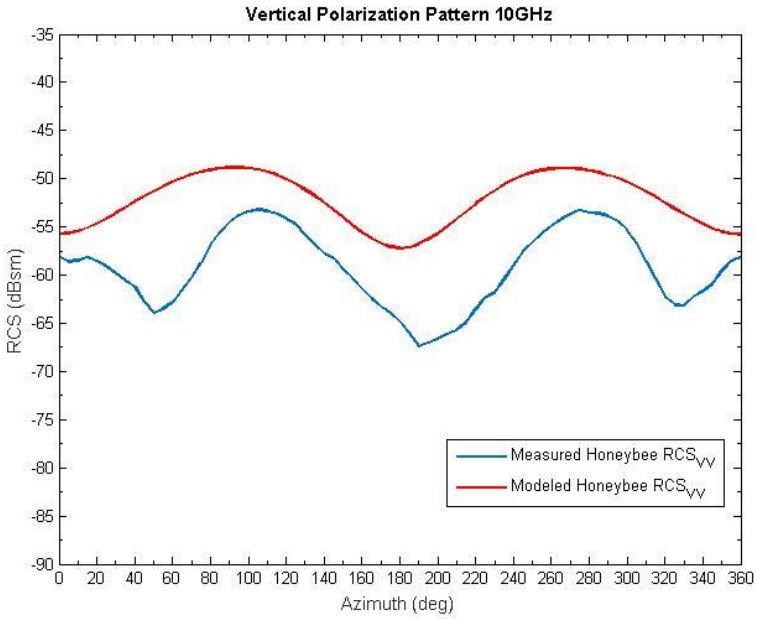

Figure 4.21: Comparison of measured and modeled backscattering cross section of a Honeybee worker (i.e., Apis Mellifera) for vertical polarization at 10 GHz.

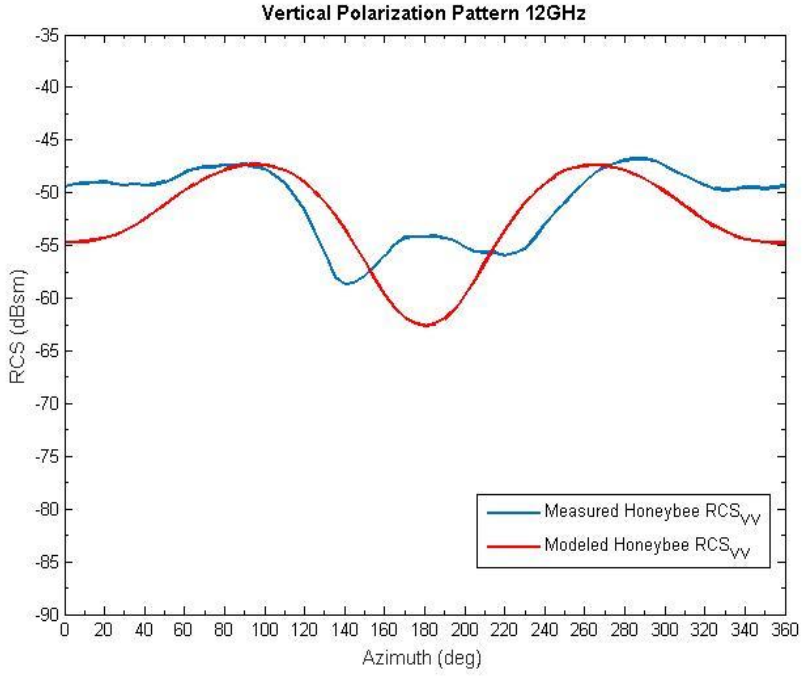

Figure 4.22: Comparison of measured and modeled backscattering cross section of a Honeybee worker (i.e., Apis Mellifera) for vertical polarization at 12 GHz.

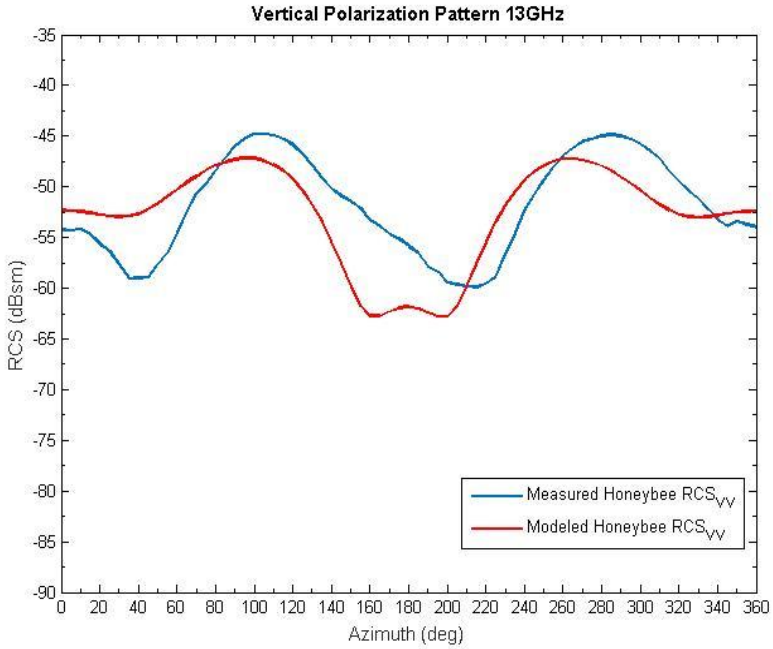

Figure 4.23: Comparison of measured and modeled backscattering cross section of a Honeybee worker (i.e., Apis Mellifera) for vertical polarization at 13 GHz.

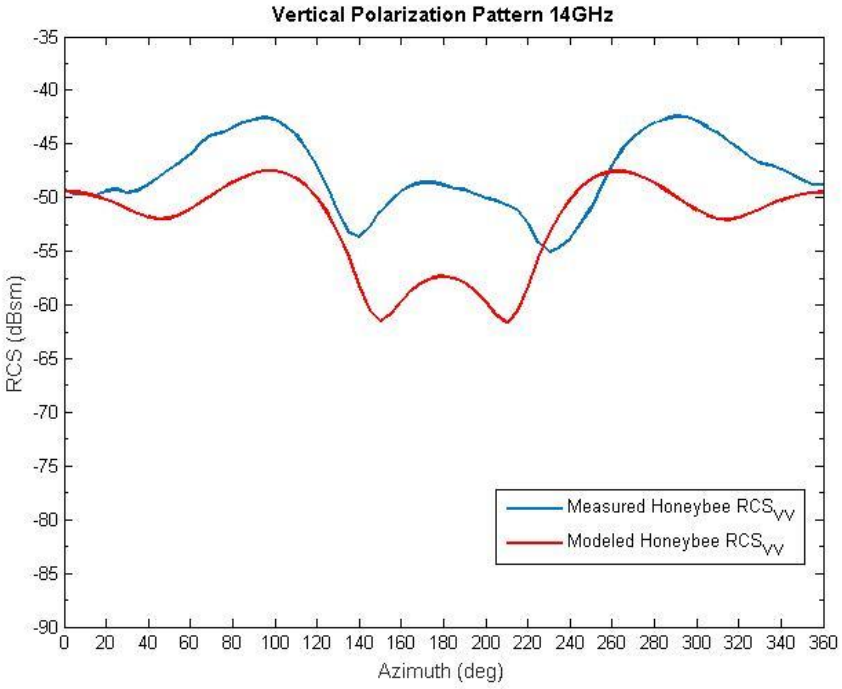

Figure 4.24: Comparison of measured and modeled backscattering cross section of a Honeybee worker (i.e., Apis Mellifera) for vertical polarization at 14 GHz.

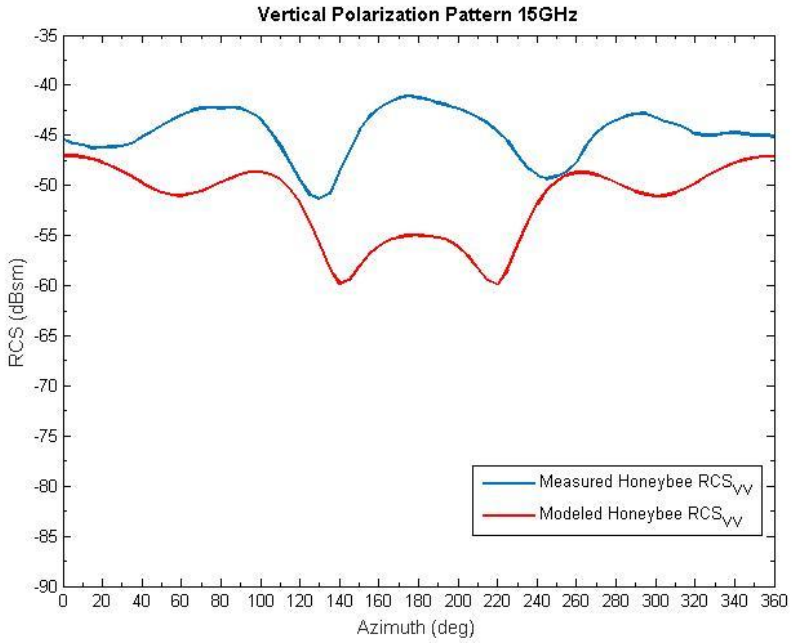

Figure 4.25: Comparison of measured and modeled backscattering cross section of a Honeybee worker (i.e., Apis Mellifera) for vertical polarization at 15 GHz.

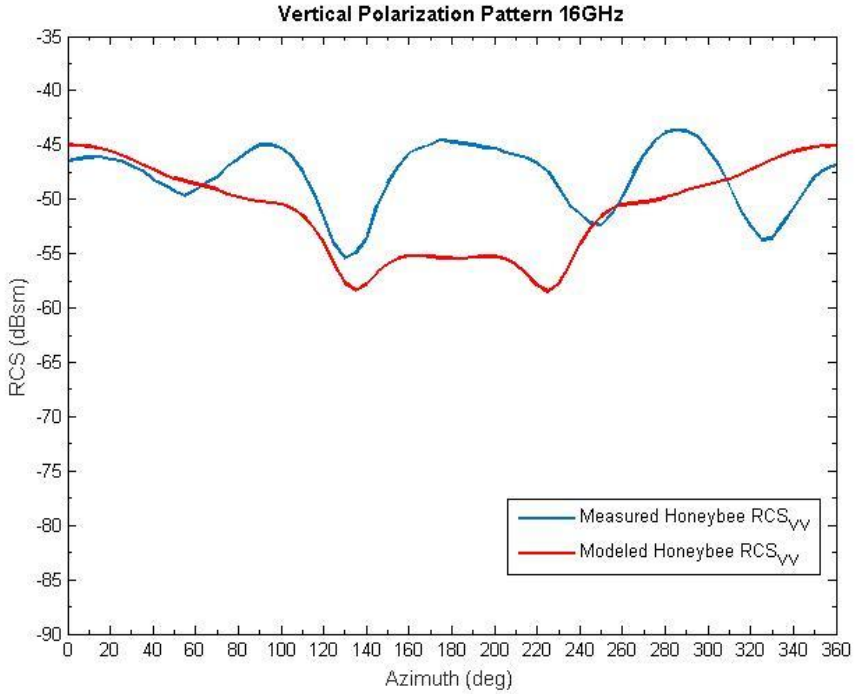

Figure 4.26: Comparison of measured and modeled backscattering cross section of a Honeybee worker (i.e., Apis Mellifera) for vertical polarization at 16 GHz.

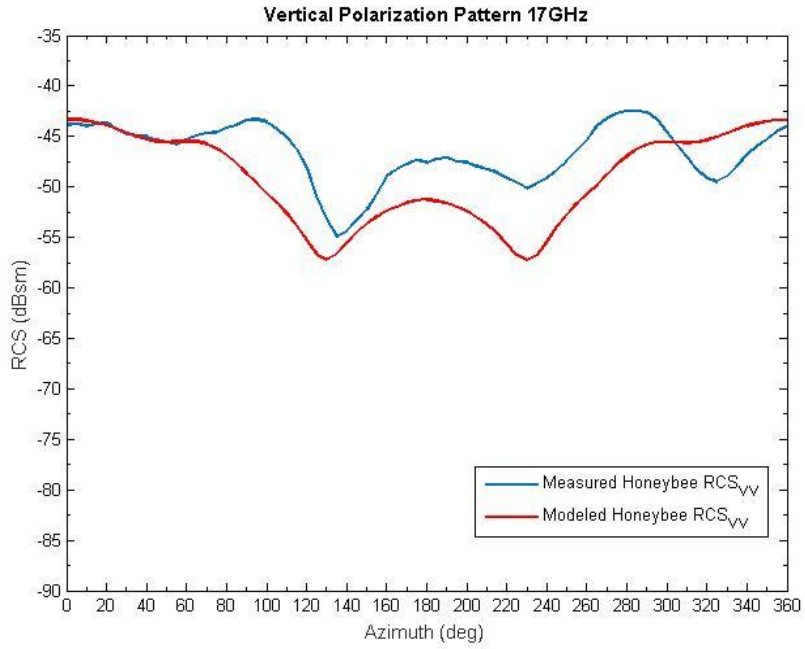

Figure 4.27: Comparison of measured and modeled backscattering cross section of a Honeybee worker (i.e., Apis Mellifera) for vertical polarization at 17 GHz.

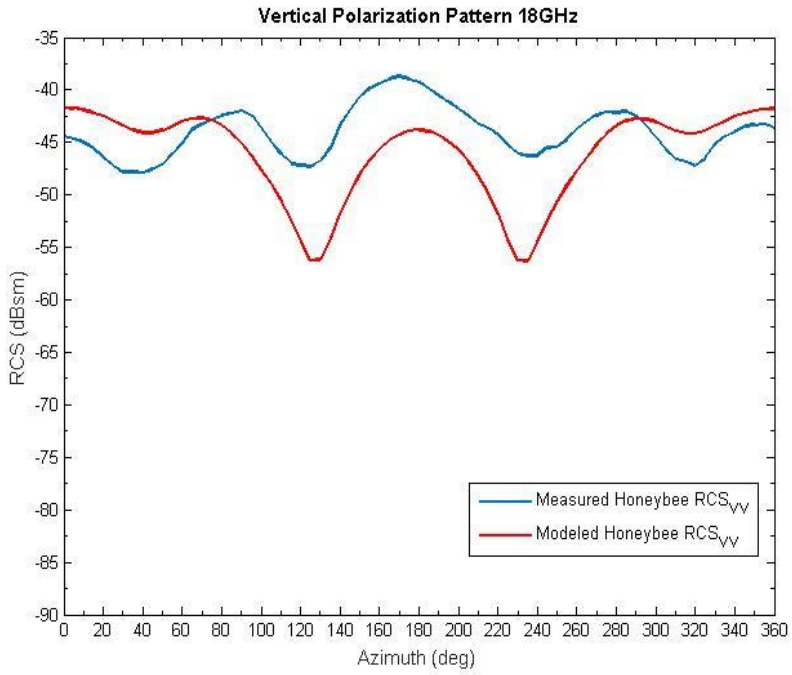

Figure 4.28: Comparison of measured and modeled backscattering cross section of a Honeybee worker (i.e., Apis Mellifera) for vertical polarization at 18 GHz.

To further verify the dielectric composition measurements of the Honeybee and investigate its effect on the backscattering cross section value, another measurement was performed after 24 hours on the same sample of the Honeybee. At that time, the Honeybee was relatively dry and dead, resulting in a lower permittivity and weaker backscattering cross sections than predicted by the Honeybee model, as presented in Figures 4.29-4.36. It is worth noting that the fluctuation observed in earlier results is no longer apparent. This further drives the point that slight movements of the Honeybee do indeed affect final results of the measurements.

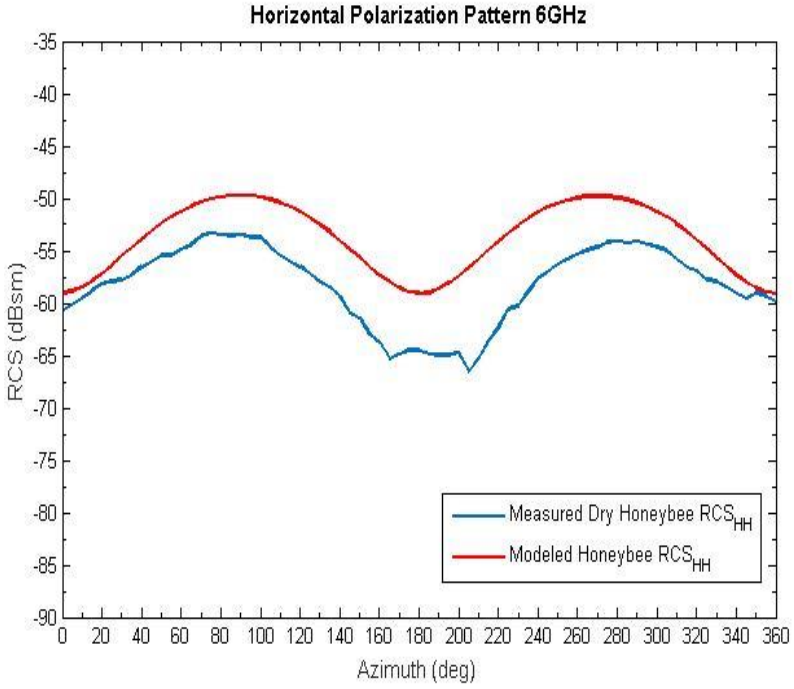

Figure 4.29: Comparison of measured and modeled backscattering cross section of a dry Honeybee worker (i.e., Apis Mellifera) for horizontal polarization at 6 GHz.

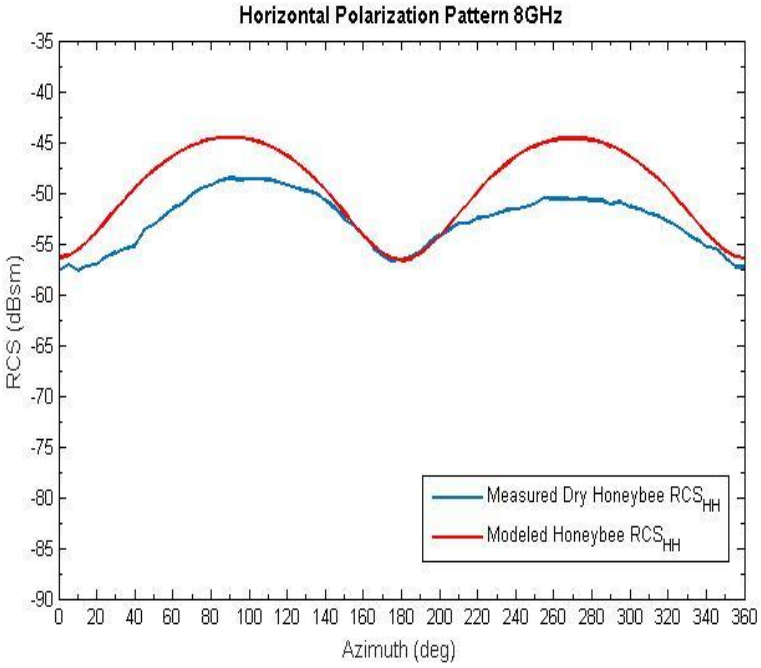

Figure 4.30: Comparison of measured and modeled backscattering cross section of a dry Honeybee worker (i.e., Apis Mellifera) for horizontal polarization at 8 GHz.

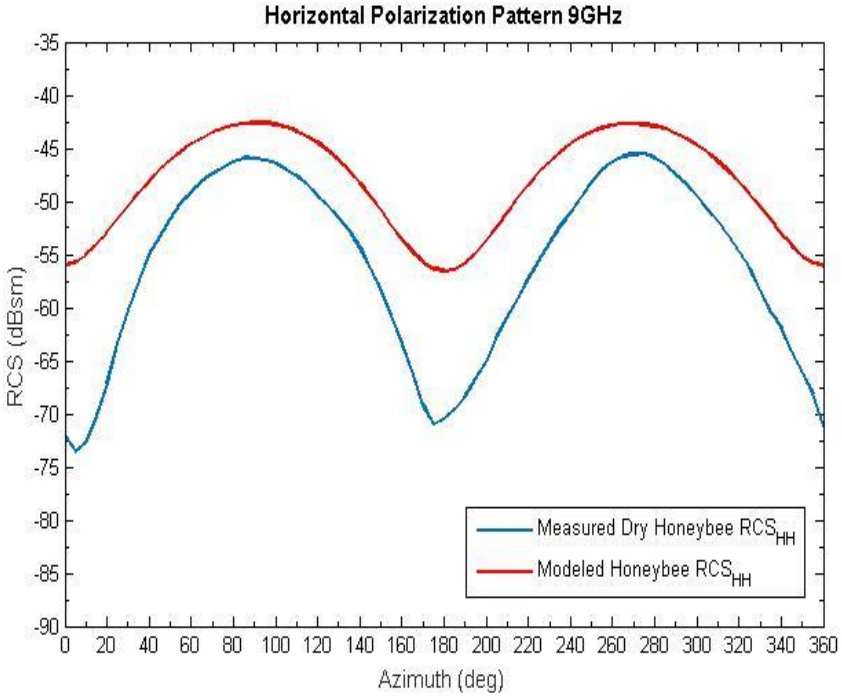

Figure 4.31: Comparison of measured and modeled backscattering cross section of a dry Honeybee worker (i.e., Apis Mellifera) for horizontal polarization at 9 GHz.

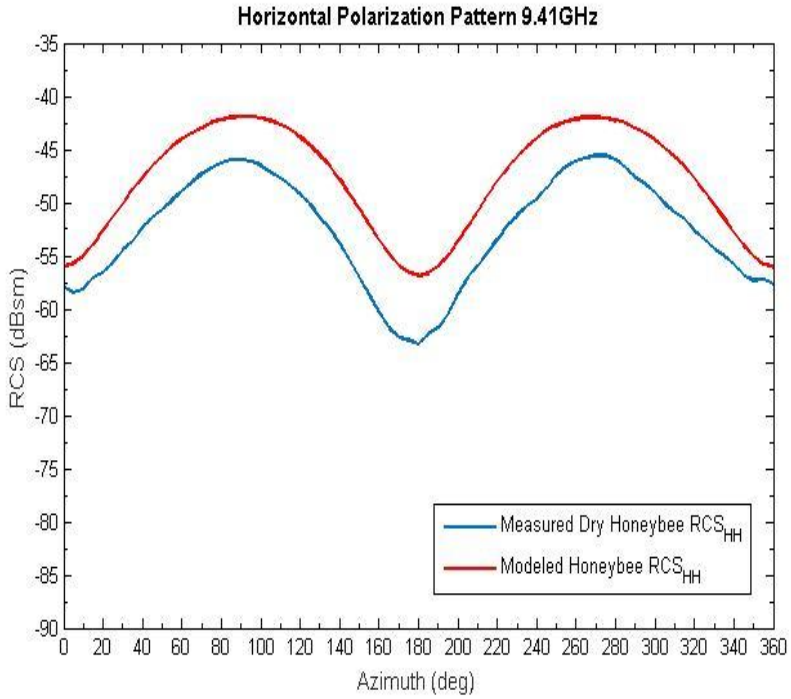

Figure 4.32: Comparison of measured and modeled backscattering cross section of a dry Honeybee worker (i.e., Apis Mellifera) for horizontal polarization at 9.41 GHz.

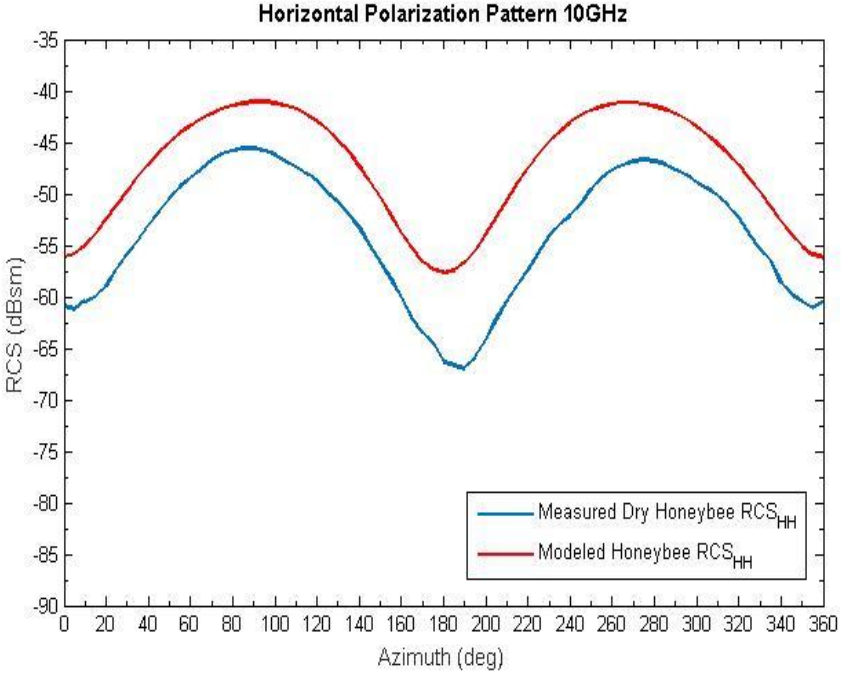

Figure 4.33: Comparison of measured and modeled backscattering cross section of a dry Honeybee worker (i.e., Apis Mellifera) for horizontal polarization at 10 GHz.

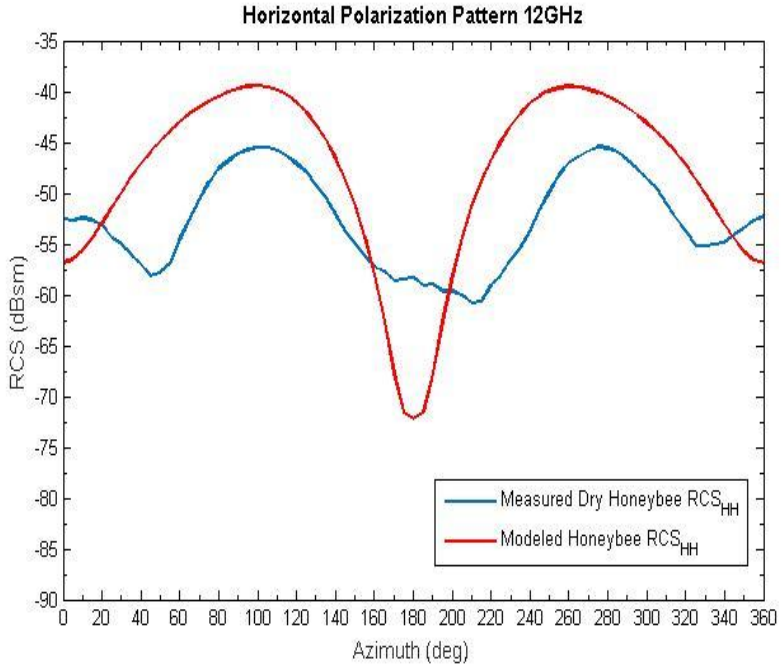

Figure 4.34: Comparison of measured and modeled backscattering cross section of a dry Honeybee worker (i.e., Apis Mellifera) for horizontal polarization at 12 GHz.

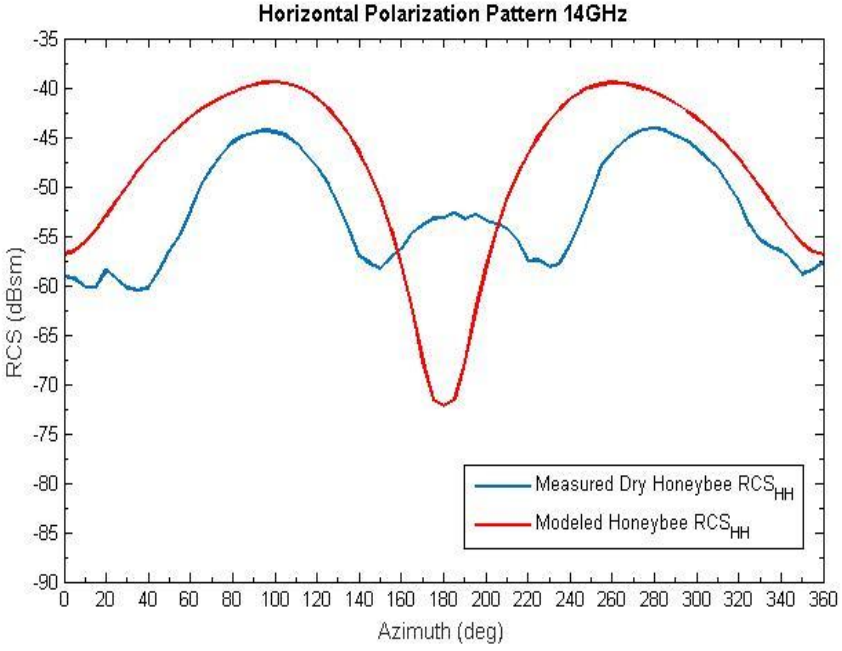

Figure 4.35: Comparison of measured and modeled backscattering cross section of a dry Honeybee worker (i.e., Apis Mellifera) for horizontal polarization at 14 GHz.

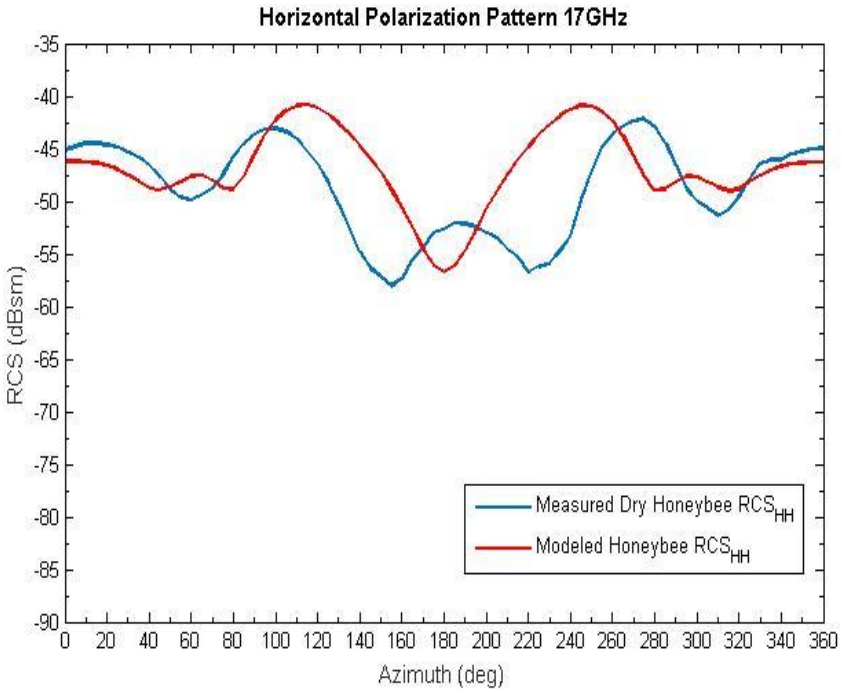

Figure 4.36: Comparison of measured and modeled backscattering cross section of a dry Honeybee worker (i.e., Apis Mellifera) for horizontal polarization at 17 GHz.

The following Figures 4.37-4.40 show the variations of the backscattering cross section of the measured Honeybee with frequency aspect. The backscattering cross section of horizontal polarization is relatively higher than the backscattering cross section of vertical polarization. This can be due primarily to geometrical factors, in which major interaction of the incident wave will show features on the order of a wavelength or larger. Here, it is noted that the Honeybee's length is larger than its diameter. Experimental assessment of this undertaken herein suggested that on average a Honeybee's diameter will be 3-5 mm, while its length on average will be 10-13 mm. Therefore, for a horizontally polarized incident wave, the bee's length will pose as a larger scatterer compared to its diameter. This in turn justifies some of the experimentally noted behavior in which, consistently though with some infrequent exception, the amplitude of the backscattering cross section is larger in the case of horizontal polarization than its vertical polarization counterpart.

Keeping in mind the fact that the backscattering cross section is generally higher when the Honeybee is broadside-on to the incident wave for horizontal and vertical polarizations, analysis of the angular dependence of the RCS level suggests that it is about same for head-on and end-on of the Honeybee. At higher frequencies (10-18 GHz), as shown in Figures 4.39-4.40, the RCS curves of the Honeybee broadside-on are relatively smooth, whereas the RCS curves of the Honeybee head-on and end-on exhibit large variations as frequency increases, with deep nulls at a frequency range between 13 GHz and 14 GHz, in particular for End-on incidence, as depicted in Figures 4.39-4.40. A physical understanding of this observable behavior can be that the bulk of a Honeybee's internal moisture is within its abdomen. Moisture, predominantly comprised of water, will undergo resonance at a frequency range approximately between 11 and 13 GHz, with a marked increase in the imaginary part of relative permittivity as noted in [1], which in turn can directly justify the deep resonance noted in the aforementioned Figures.

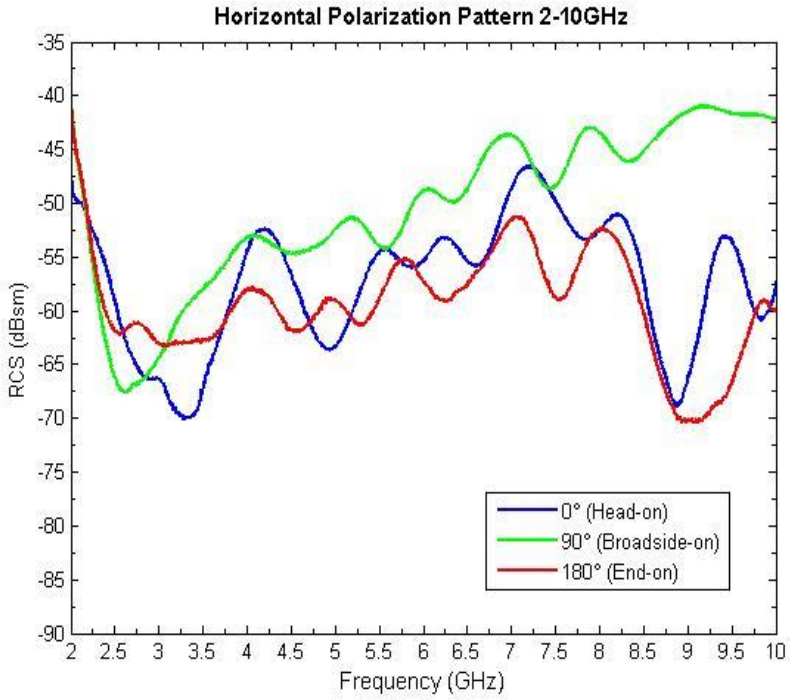

Figure 4.37: Frequency response of backscattering cross section of Honeybee worker (i.e., Apis Mellifera) across S, C-bands completely and X-band partially at H-pol.

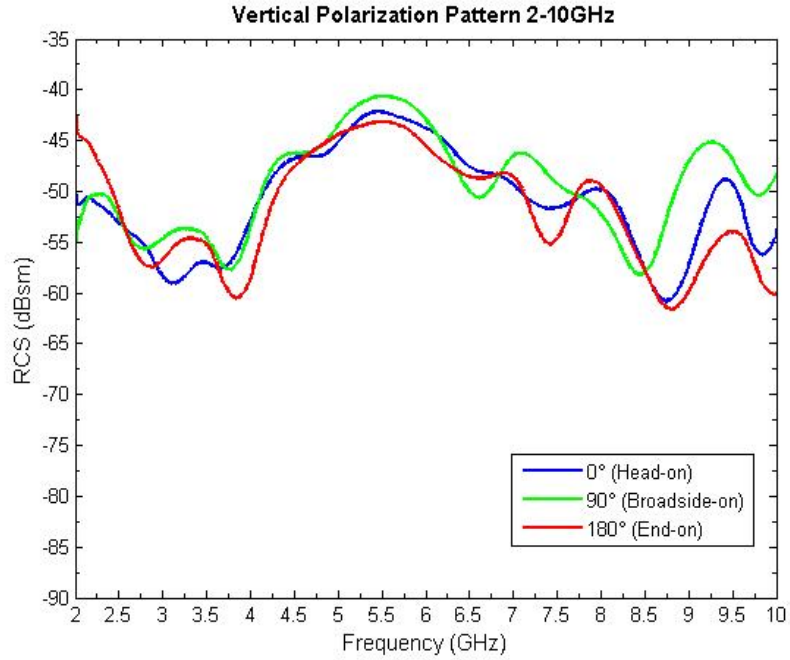

Figure 4.38: Frequency response of backscattering cross section of Honeybee worker (i.e., Apis Mellifera) across S, C-bands completely and X-band partially at V-pol.

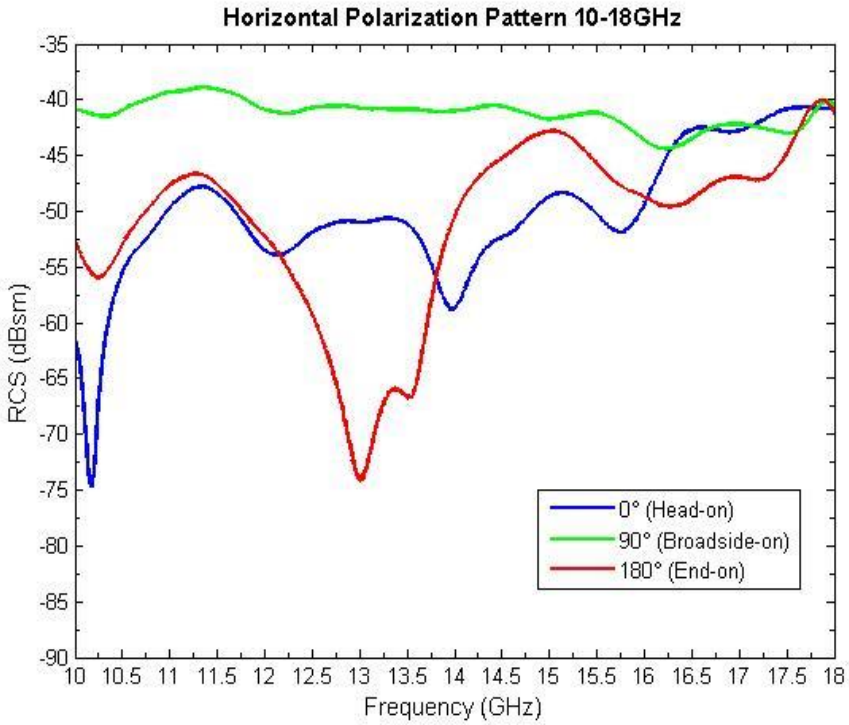

Figure 4.39: Frequency response of backscattering cross section of Honeybee worker (i.e., Apis Mellifera) across X-band partially and Ku-band completely at H-pol.

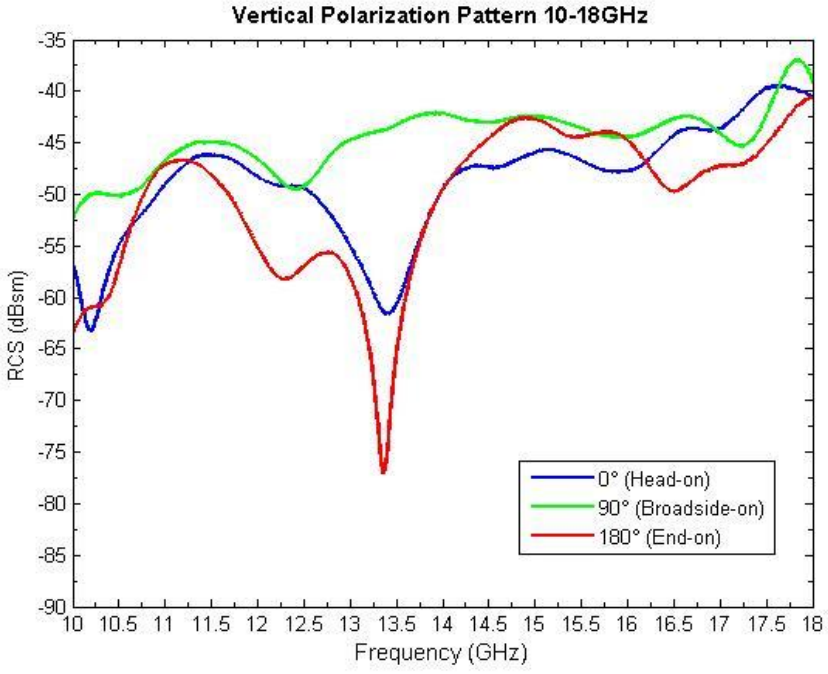

Figure 4.40: Frequency response of backscattering cross section of Honeybee worker (i.e., Apis Mellifera) across X-band partially and Ku-band completely at V-pol.

4.6 References

[1] Levis, Curt, Joel T. Johnson, and Fernando L. Teixeira. *Radiowave propagation: physics and applications*. John Wiley & Sons, 2010.

Chapter 5

Conclusion and Future Work

In this thesis, we used FEKO, a CEM tool, to obtain realistic scattered electric fields of an organismal model for a Honeybee worker (i.e., Apis Mellifera), in order to accurately predict the radar characteristics of biological scatterers at multiple frequencies, polarizations, and observing angles. The numerical simulation technique known as method of moments (MoM) was used. The simulated backscattering cross sections of the Honeybee agree with the laboratory measurements.

Chapter 1 gave a comprehensive review of earlier observations undertaken on flying insects using various techniques. From this review, it's clear that direct insect observation provides limited insight at best into insect behavior, for various reasons. These include the fact that when using strictly traditional tracking techniques such as mark-recapture, and complementary methods such as genetic analysis, as well as pollen mapping, efficacy soon becomes limited by practical considerations, namely, the large geographical area which may be spanned by bees individually and as a group. This is further compounded by the case-by-case treatments which techniques such as genetic analysis require. While other techniques such as transponder-fitting offer significantly more promise, they are limited by their potentially corrupting effect on actual bee behavior.

The proposed tracking-scheme based on RCS measurement is, similarly, not without limitations, but offers significantly more practical promise. In this method, only a select set of frequencies are allowed, a limited set of azimuth and elevation angles are permissible which limit their generality in entomological radar applications, and most of the measurements are done experimentally in laboratories, which are prone to human error. This highlights the inadequacy of existing knowledge in establishing relevant radar classification schemes. For this reason, the work

that is presented aimed to overcome much of these limitations, by adopting schemes based on computational electromagnetic tools with complementary lines of analysis, aiming at enabling prediction of the radar scattering characteristics of aerial insects, with empirical findings supporting much of the claims made.

In order to produce realistic scattered fields from biological scatterers such as insects, prior knowledge of their dielectric properties is required. Throughout Chapter 2, the dielectric properties data of Honeybee tissue have been represented. The dielectric measurements of three sets of Honeybee samples were performed using a rectangular waveguide at a frequency range from 8.2 GHz to 12.4 GHz at room temperature. From empirical analysis, it was found that dielectric properties in the frequency range between 10-12 GHz of the Honeybee tissue is comparable with that of dry human tissue. The ability of waveguide characterization techniques are known to be limited when analyzing nonhomogeneous dielectric media such as biological tissue. To address this shortcoming, dielectric mixture relationships outlined by Landau & Lifshitz and Looyenga were used, which in turn allowed for the elimination of air gap effects between samples and waveguide throughout the dielectric measurements. In this way, the dielectric constant for Honeybee body tissue was found to be from 10.69 to 10.59 as the frequency increased from 8.2 to 12.4 GHz, respectively. In contrast, the loss tangent was found to increase from 0.26 to 0.41 for the same frequency range. Using these measurements, the RCS was simulated and predicted using computational electromagnetic techniques furnished by the commercial software package FEKO antenna modeling software.

Building upon the lines of analysis outlined in Chapter 2, in the subsequent chapter it was shown that numerical simulation techniques, such as the method of moments implemented in the FEKO software package, can produce realistic scattered electric fields of an organismal model, a Honeybee worker (i.e. Apis Mellifera) in this case. The backscattering cross sections were calculated for both the horizontal and vertical polarizations at multiple frequencies and diverse

observable angles. This numerical technique was shown to be of particular use in generating a considerable amount of data for radio scattering through a broad set of azimuth or elevation angles, by eliminating the practical difficulties that are typically associated with laboratory measurements. Although the simulated scattering properties of the Honeybee obtained through the FEKO method of moments largely agrees with past controlled measurements when the Honeybee is broadside-on to the incident wave polarized horizontally at 9.41 GHz, more direct laboratory measurements for quantifying radio wave scattering at different frequencies, polarizations, and viewing angles were shown to be needed, in assessing the validity of this numerical electromagnetic technique.

For this reason, further validation efforts are undertaken in Chapter 4, in which model results and experimental measurements are compared. The backscattering cross section measurements of the Honeybee were carried out for both horizontal and vertical polarizations over the frequency range between 2 and 18 GHz with a frequency step of 6 MHz. The measurements were performed at the incident angle of the plane wave $\theta = 90^{\circ}$ and $0^{\circ} \leq \varphi \leq 360^{\circ}$. The azimuth angle was incremented by 5 degrees. Results reveal a high degree of agreement in backscattering cross sections between the measured and modeled Honeybees, thereby validating dielectric measurements of the Honeybee tissue at X-band using a rectangular waveguide technique, along with backscattering cross section results from both simulation and measurement.

5.1 Limitations

While the high degree of agreement in results is promising, several limitations associated with RCS measurements accounting for some of the observed disagreements is acknowledged.

The RCS of the Honeybee is close to the sensitivity limit of the compact range; in spite of time gating and background subtraction techniques undertaken to minimize any contaminating effects this may have had practically, this still had some bearing on measured results, in particular when incident wave polarization was vertical, for reasons previously discussed. The measurements will therefore be limited by background RCS level, with a combination of stray reflections from the range walls, styrofoam column, cup to hold the bee, and reflections between the network analyzer, amplifier, and feed affecting obtained measurements. One potential way to overcome some of these limitations in future studies is by performing outdoor sky-looking measurements. The construction of a special position apparatus would serve a complementary purpose. Additionally, more accurate measurements could be achieved with a lower RCS positioning system, improved gating techniques (possibly real-time gating with pulsed incident wave emission as opposed to continuous), or improving impedance mismatch near the network analyzer, where we see large reflections in time.

In short, such numerical electromagnetic techniques could be applied for airborne insects and have a significant impact on the field of radar entomology; for instance, the quantifying scattering wave properties of these insects can be used with other parameters (time of flight, altitude, etc.) for developing a classification system to discriminate between species of flying insects.

5.2 Ideas for Future Work

5.2.1 Circularly Polarized Antenna for Harmonic Transponder

As discussed in Chapter 1, most of the wire transponders adopted so far for tracking bees have attachment problems, as they need to be kept stiff and vertical to minimize the polarization loss factor. To eliminate these problems, we propose designing and developing an antenna that can be fitted freely on the bee abdomen or thorax. This antenna can be circularly polarized, giving alignment freedom and extracting maximum power from all angles.

Currently, with the Honeybee model done in FEKO with well-known dielectric composition, it is possible to utilize FEKO to configure different antenna models that could be fitted onto the Honeybee. These models will help us to study and investigate the body effect of the Honeybee in radiation characteristics under different antenna configurations. As was demonstrated in Chapter 2, the properties of the dielectric have been already measured, and the next step is to design a robust circularly polarized antenna that would fit the bee and not affect its natural behavior. A crucial step is to fit the modeled antenna on top of the modeled Honeybee and observe the result. With the advancement in additive manufacturing techniques, the designed antenna could theoretically be printed out and fitted onto an actual Honeybee for further testing.

5.2.2 Individual Transponder Identification

Due to the limitations of existing harmonic tracking systems, it is difficult to track multiple bees at the same time. One solution to this problem is to have an array of harmonic radar, to generate multiple signals which can differentiate tagged individuals. This could easily be achieved if the associated harmonic transponders have a narrow band width, to reject frequencies other than the

fundamental frequency. However, having an array of harmonic radar introduces a complexity in the design and is expensive to apply. One promising and possible way to overcome this limitation is to apply the Orthogonal Frequency Division Multiplexing (OFDM) technique to harmonic radar technology. OFDM has been successfully used for HF radio applications, and it has been chosen as the standard for digital audio broadcasting and high-speed wireless networks. The basic idea of this technique is using a large number of parallel narrow-band subcarriers, instead of a single wide-band carrier, to transport information simultaneously. The advantages of this method are that it is robust against narrow-band interference and efficient with multi-path fading.

5.2.3 Improving the Conversion Efficiency of Frequency Doubler

Further investigations are needed to improve conversion efficiency of the Schottky diode. Since bees are active and work in the daytime, we can consider integrating the diode with organic photovoltaics cells, to be used both as a frequency doubler under outdoor illumination and to provide an external bias. This would eliminate the need for biasing components and significantly reduce design complexity, size and weight. More importantly, this would guarantee the diode harmonic generation process is active under low input RF signal power at long range.

Appendix A

Calibration Standards Verification

A.1 Calculated RCS of Spheres Used and Calibrated Sphere Data

Two conductive spheres with diameters of 2.75 and 12 in. respectively were calibrated to each other for comparison. The calibration measurements swept from 2 GHz - 18GHz for comparison. Figures A.1-A.4 show the comparison between the measured and the calculated RCS of both spheres using a Mie Series solution equation for backscattering from a PEC sphere. The results show about 2 dB maximum error but are found to be more accurate for the 12-inch-diameter sphere.

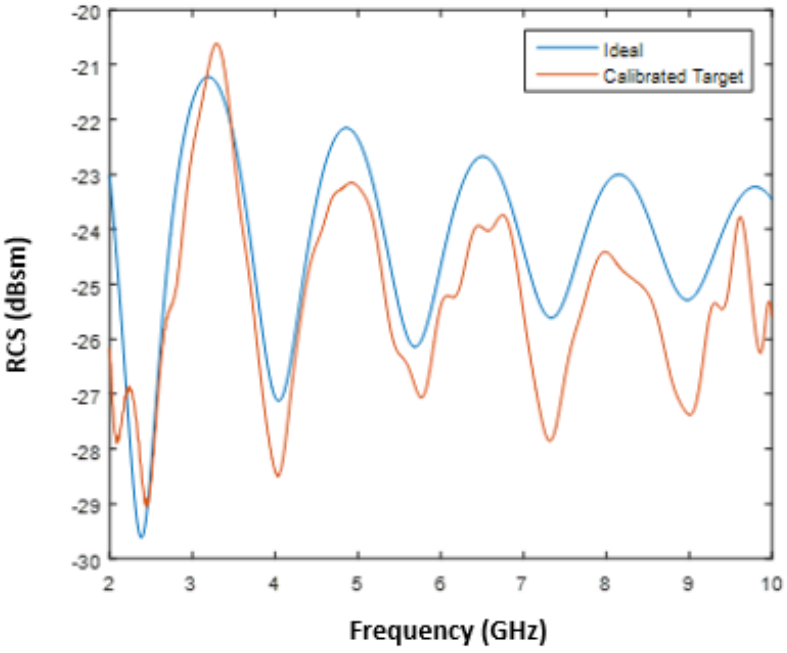

Figure A.1: 2.75" sphere 12" ref. 2-10GHz.

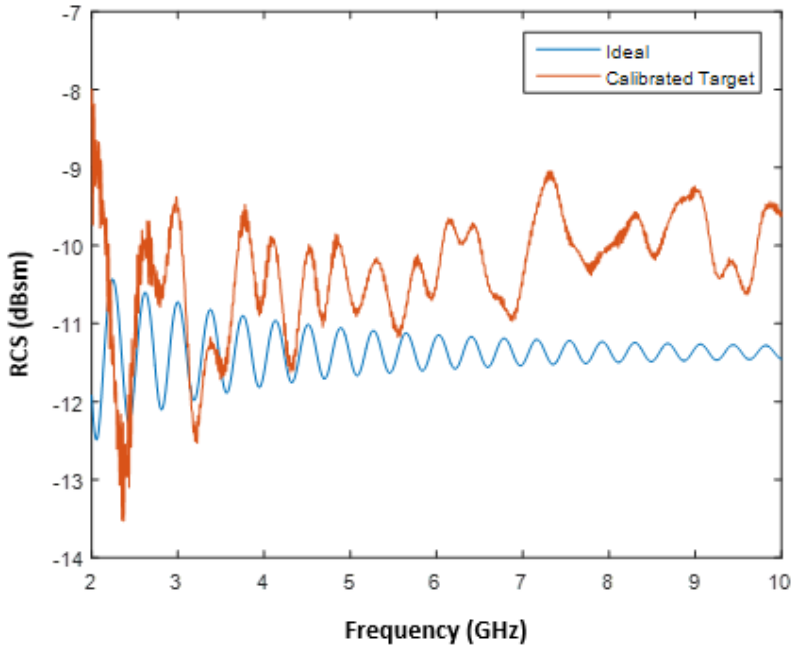

Figure A.2: 12" sphere 2.75" ref 2-10 GHz.

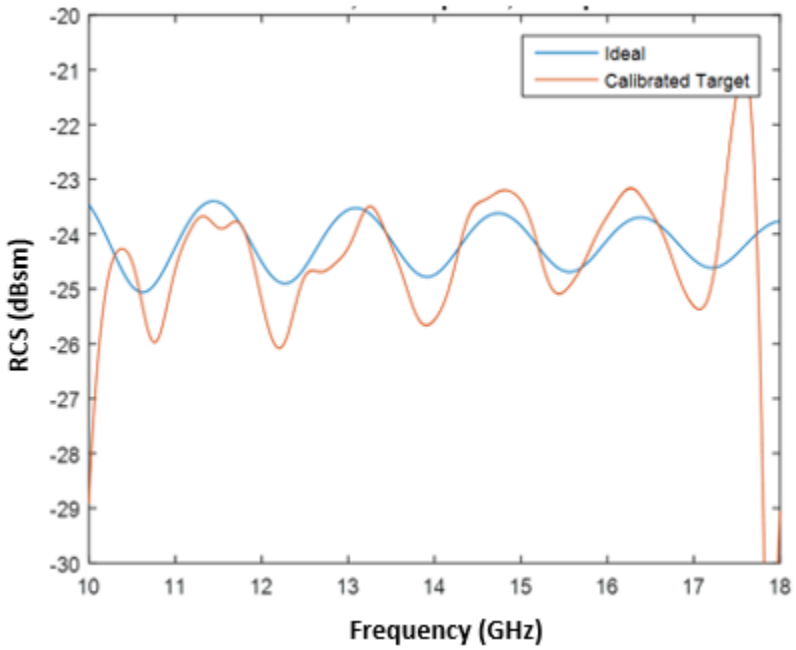

Figure A.3: 2.75" sphere 12" ref. 10-18GHz.

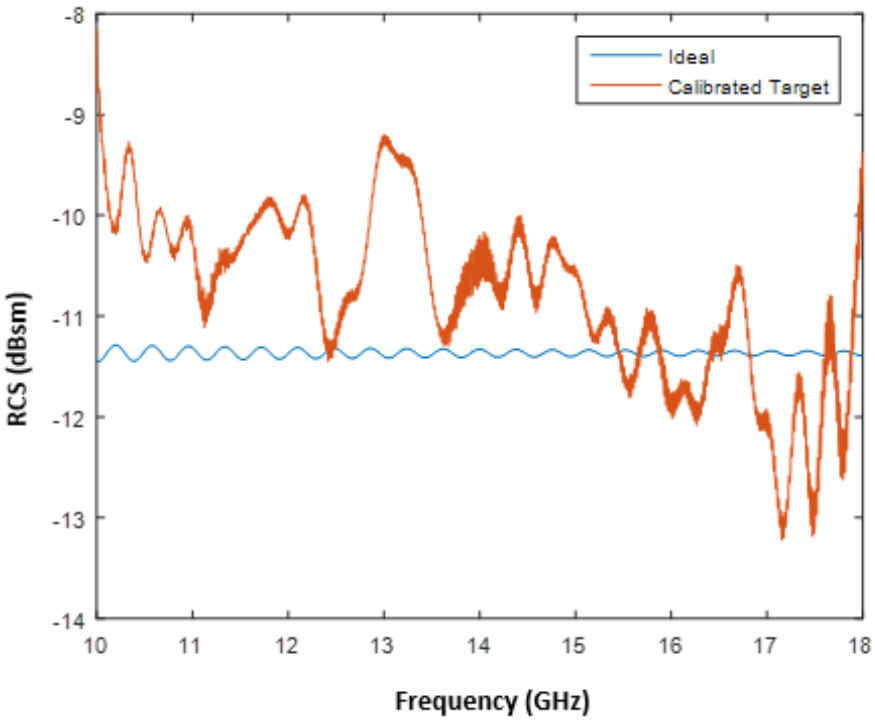

Figure A.4: 12" sphere 2.75" ref 10-18 GHz.

Appendix B

Background RCS Measurement

B.1 Total Background RCS Vs Modeled Honeybee RCS

In this appendix, the following Figures B.1-B.12 compare the total RCS level between the background, including both column and styrofoam cup, and modeled Honeybee at multiple frequencies and viewing angles for horizontal and vertical polarizations. In general, the total background RCS for vertical polarization is found to be relatively higher than the backscattered RCS of the modeled Honeybee.

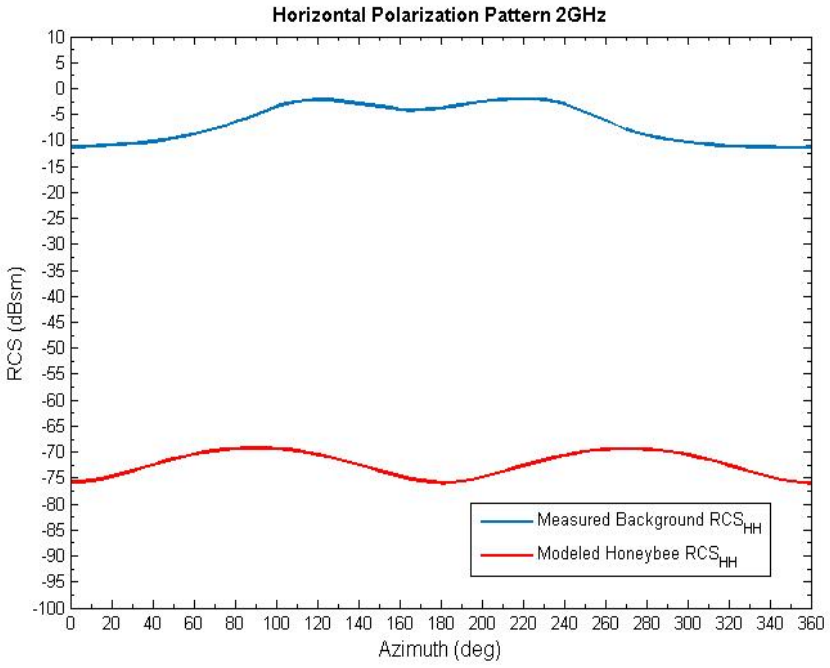

Figure B.1: 2 GHz Background Horizontal Polarization.

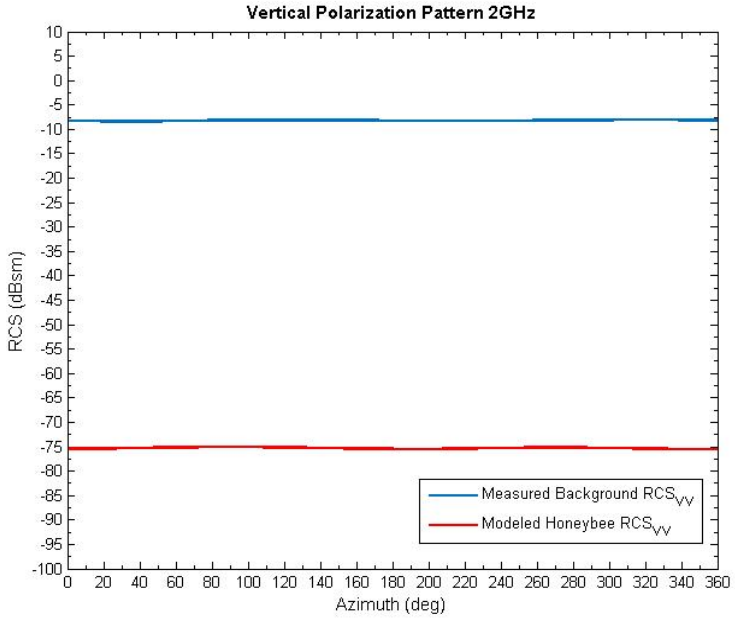

Figure B.2: 2 GHz Background Vertical Polarization.

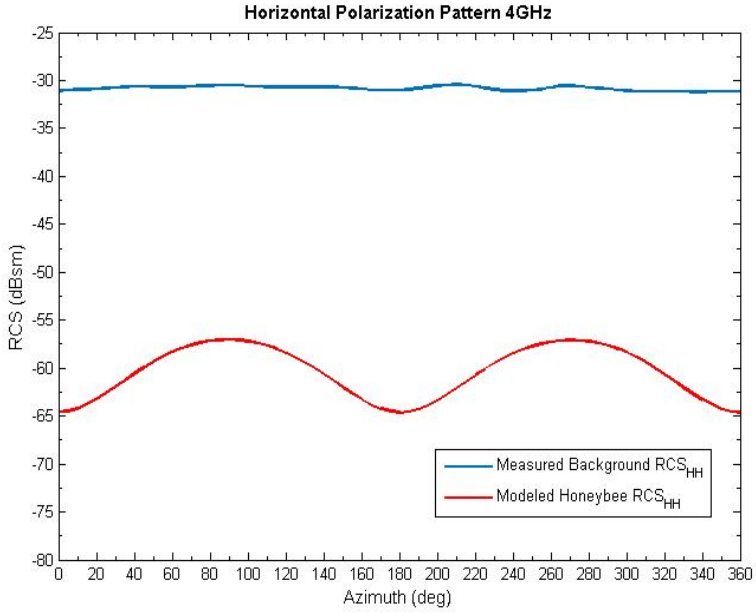

Figure B.3: 4 GHz Background Horizontal Polarization.

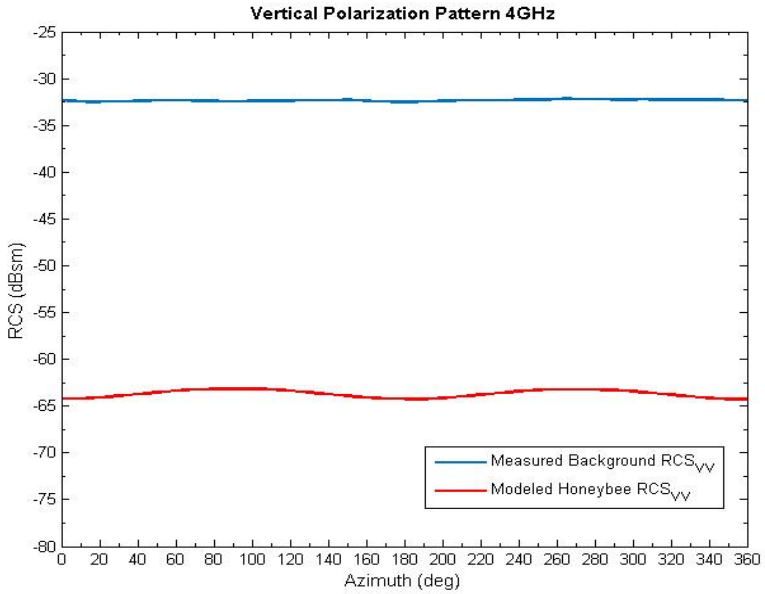

Figure B.4: 4 GHz Background Vertical Polarization.

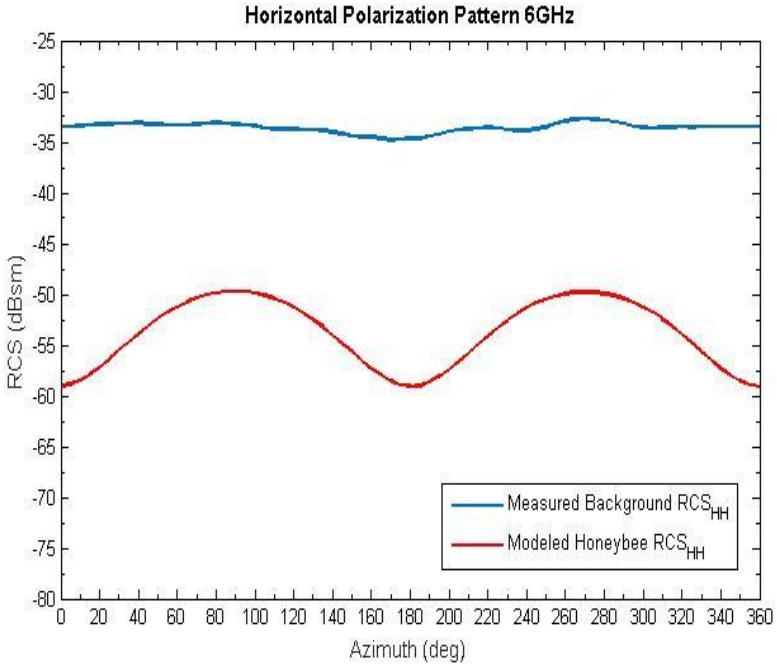

Figure B.5: 6 GHz Background Horizontal Polarization.

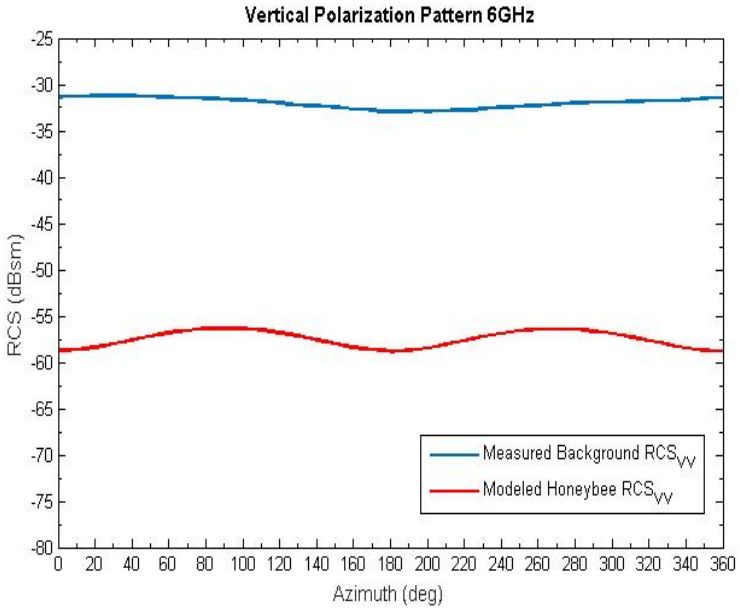

Figure B.6: 6 GHz Background Vertical Polarization.

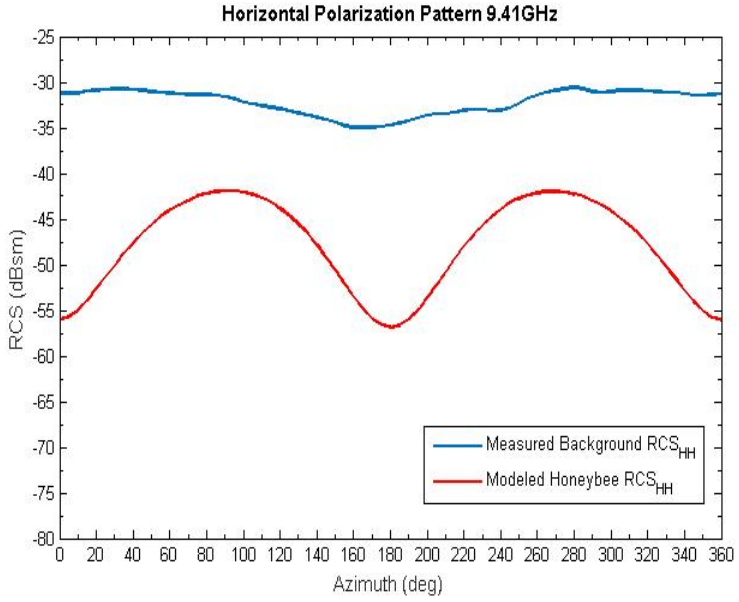

Figure B.7: 9.41 GHz Background Horizontal Polarization.

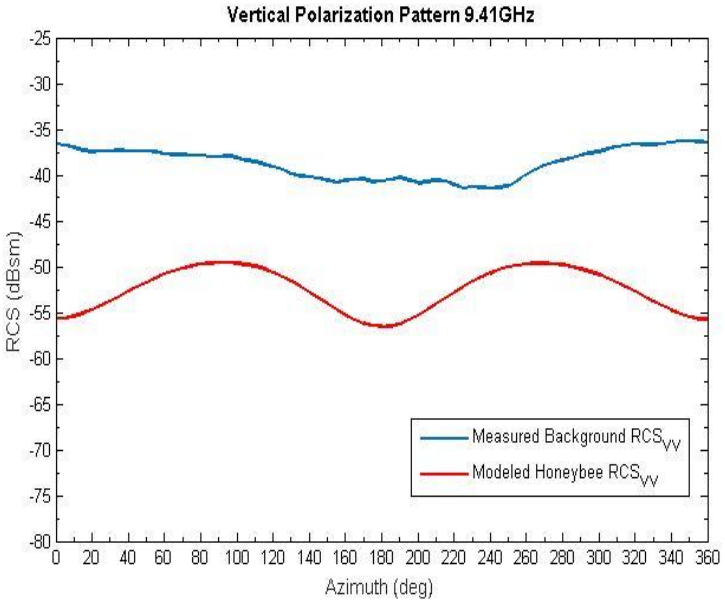

Figure B.8: 9.41 GHz Background Vertical Polarization.

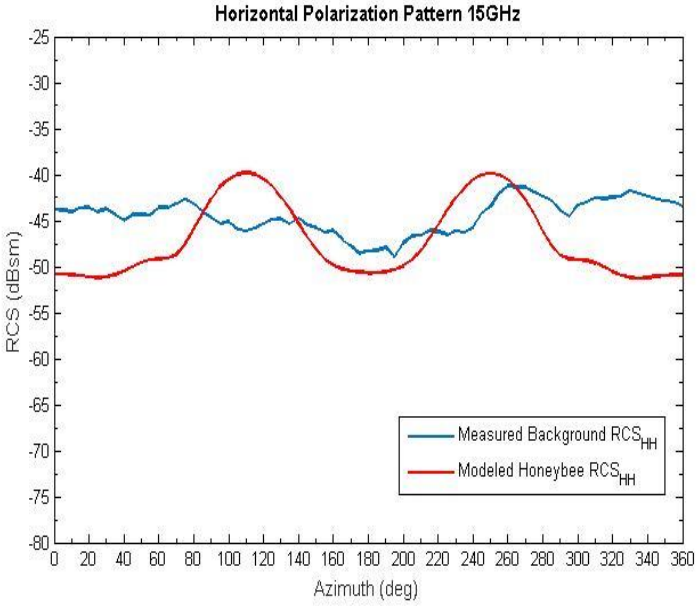

Figure B.9: 15 GHz Background Horizontal Polarization.

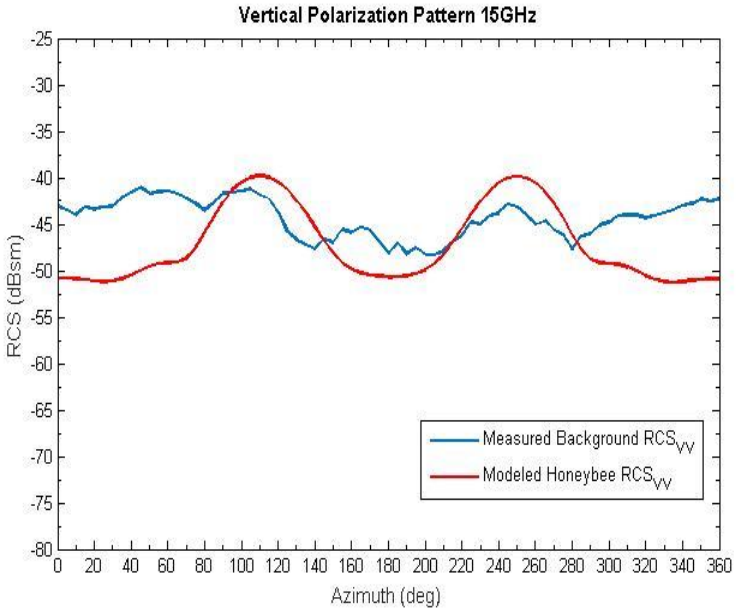

Figure B.10: 15 GHz Background Vertical Polarization.

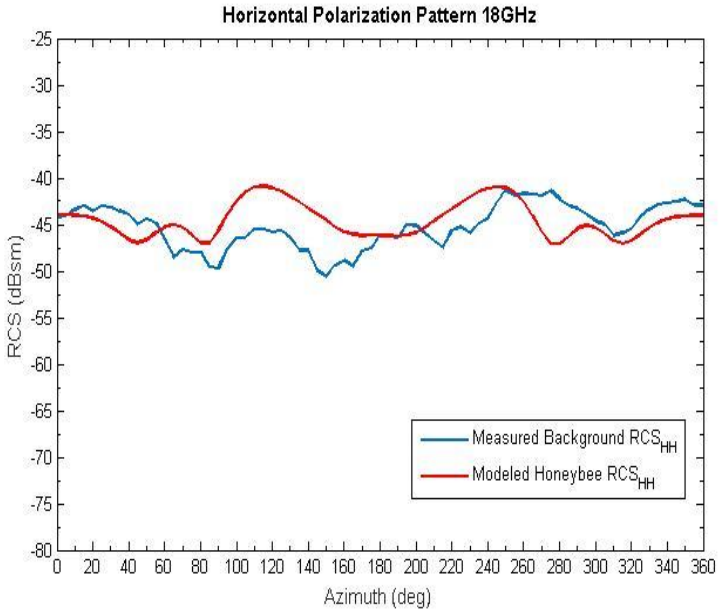

Figure B.11: 18 GHz Background Horizontal Polarization.

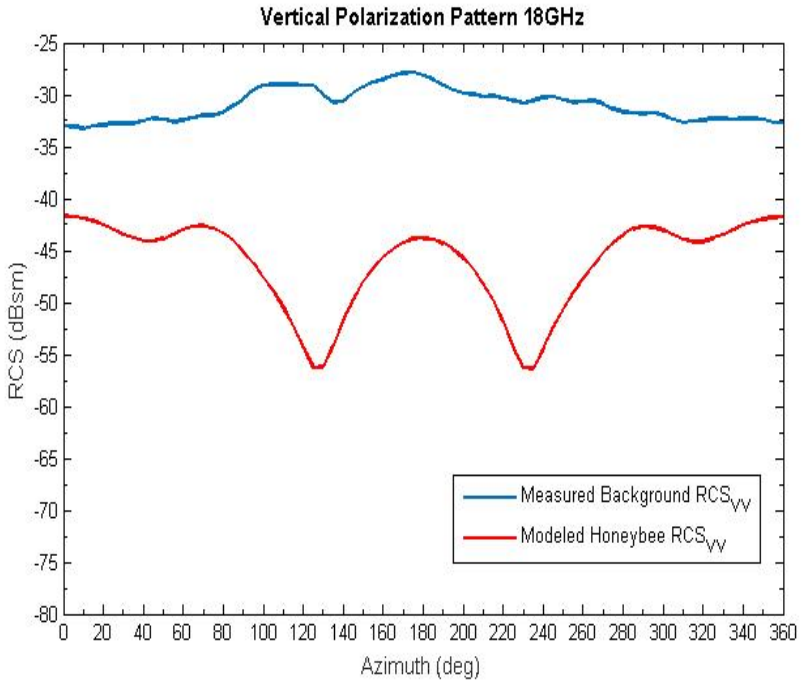

Figure B.12: 18 GHz Background Vertical Polarization.

B.2 Minimum Detectable Signal

Figures B.13 and B.14 show the results of the background RCS itself (noise floor) after subtracting the column and the styrofoam cup. Experimentally, one can see that RCS levels for both the background (noise) and the honeybee (target) are comparable. As a result, the backscattering cross section of the measured Honeybee is only visible for frequencies at or higher than 5 GHz when measuring the horizontal polarization RCS, while the vertical is only visible at 7 GHz or higher, where the background noise floor level was not obstructive and did not interfere with the Honeybee RCS results.

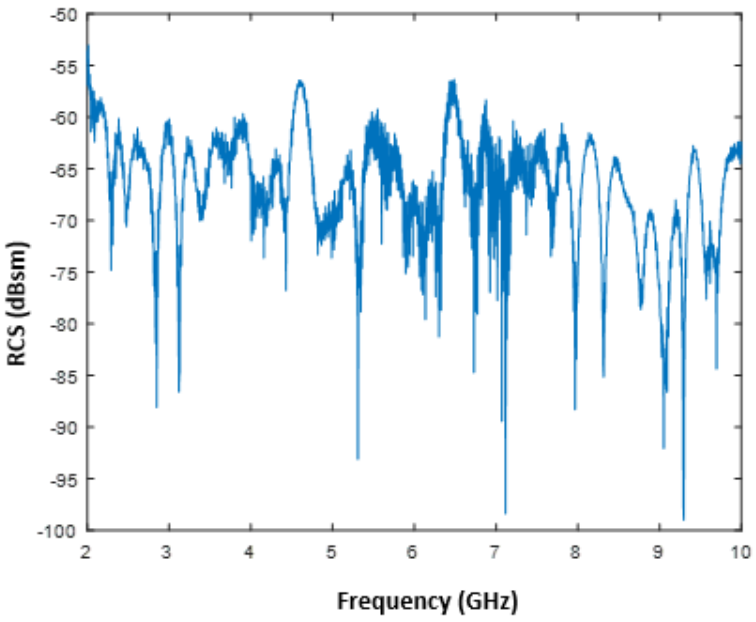

Figure B.13: Background Subtracted Frequency Response 2-10 GHz.

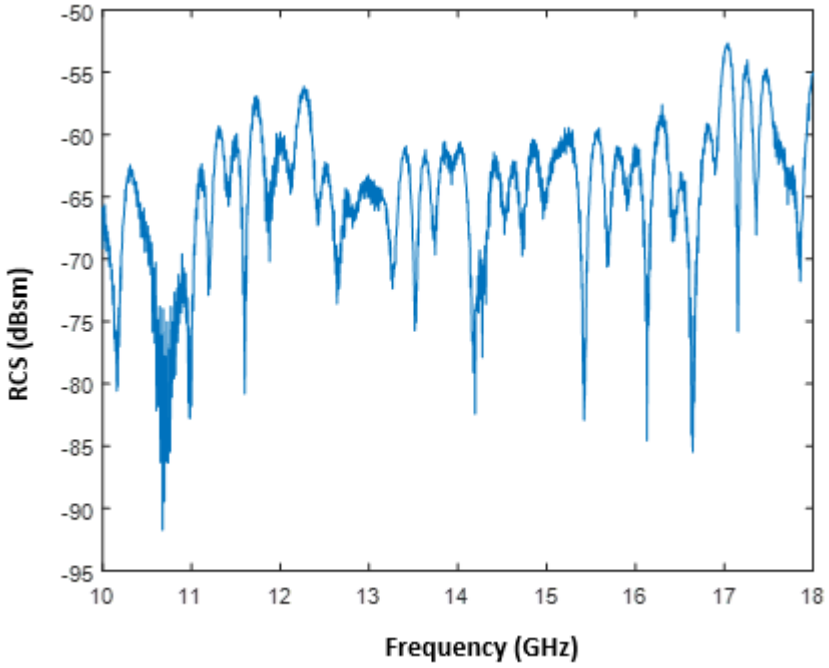

Figure B.14: Background Subtracted Frequency Response 10-18 GHz.

B.3 Background Time Domain

The time-gate was centered on the main peak of the 12” sphere, to suppress the multipath reflections and clutter to the peak to enter the gate. The 12” sphere was gated at 102 ns and 104 ns, as shown in Figure B.15.

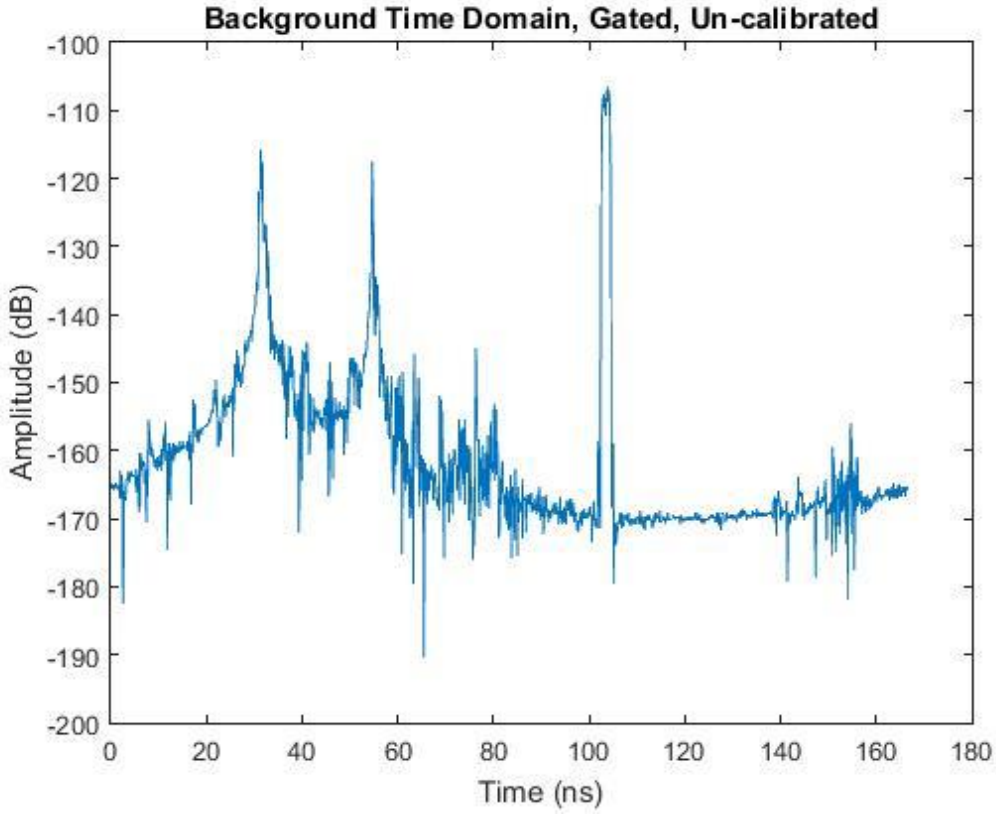

Figure B.15: Illustration of time domain analysis, gating and suppression gating of corrupting background contribution to measurement RCS.

VITA

Omar Alzaabi

Omar Alzaabi was born in Dubai, United Arab Emirates (UAE). After completing high school in his hometown, he became sponsored by the UAE's Ministry of Higher Education to complete a Bachelor of Science in Electrical Engineering at The Penn State University, University Park, where he completed his BSc in Spring 2012. In Fall 2012, Omar joined the Abu Dhabi National Oil Company (ADNOC). Shortly after, he resumed his studies at Penn State University at the Department of Electrical Engineering working towards a Master of Science degree. During the Summer of 2014, Omar earned his M.S. degree in Electrical Engineering, and has been with the same department since then, working towards his Ph.D.

Conference Presentations and Publications:

- **Omar Alzaabi,** Julio Urbina, James K. Breakall, and Michael Lanagan, "Dielectric Properties of Honey Bee Body Tissue for Insect Tracking Applications," *USNC-URSI National Radio Science Meeting*, Jan 2018, Boulder, CO.

- **Omar Alzaabi,** Diego Peñaloza, Julio Urbina, James K. Breakall, and Michael Lanagan, "Airborne Insects Radar Scattering Characteristics Utilizing Electromagnetic Modeling," *USNC-URSI National Radio Science Meeting*, Jan 2019, Boulder, CO.

- **Omar Alzaabi,** Diego Peñaloza, Mohammad M. Al-Khaldi, Julio Urbina, James K. Breakall, Michael Lanagan, Harland M. Patch and Christina M. Grozinger "A Numerical Modelling Approach towards Radar Cross Section Characterization of Airborne Insects," *APS-URSI IEEE International Symposium on Antennas and Propagation and USNC-URSI Radio Science Meeting*, July 2019, Atlanta, Georgia.

- **Omar Alzaabi,** Diego Peñaloza, Mohammad M. Al-Khaldi, Julio Urbina, James K. Breakall, Michael Lanagan, Harland M. Patch and Christina M. Grozinger " Numerical Modelling and Prediction of Airborne Organismal Radar Scattering Properties for Entomological Applications," *IEEE Transactions on Antennas and Propagation (2019)* (*Under Review)*